Correlation of Structure and Energy at $Ni–Al_2O_3$ Interfaces

Hila Meltzman

Correlation of Structure and Energy at $Ni–Al_2O_3$ Interfaces

Hila Meltzman

The research thesis was done under the supervision of

prof. W.D Kaplan in the department of materials engineering.

The Generous Financial Help Of BSF, RBNI, Ilan Ramon Fund & Min. Science is Gratefully Acknowledged.

List of publications:

Published manuscripts:

The equilibrium crystal shape of nickel

An experimental method for calibration of the plasmon mean free path

Published collaboration (based on the methodology presented in this research):

Orientation relationships of copper crystals on c-plane sapphire
(in press)
In this collaboration, H. Meltzman prepared all of the TEM specimens and conducted all of the TEM experimental work.

Equilibrium Segregation of Ti to Au-Sapphire Interfaces

This collaboration was coordinated by H. Meltzman, who prepared the TEM samples, conducted all of the TEM experimental work and performed a large part of data processing and analysis

Manuscripts under preparation:

1) **Hf-Doped Ni-Al_2O_3 Interfaces at Equilibrium.**

Structure and Energy of Equilibrated Ni-Al_2O_3 Interfaces.

Table of Contents

List of Figures

List of Tables

Abstract

The structure and properties of metal-ceramic interfaces have been the focus of many studies since the 1960's, mostly due to the potential for numerous technological applications such as metal-ceramic bonding, brazing, microelectronic packaging, thin film technology, high temperature metal-oxidation processes, photovoltaic cells, protective coatings for metals, bioactive implant coatings, and high temperature aircraft components. The complexity of solid-solid interfaces arises not only from the difference in long rang atomistic order on both sides of the interface, but also from the wide variety of defects that can form, and the unique structural and compositional characteristics of each interface, depending on the relative orientation of the two crystals, the compositions, the temperature and sometimes even the manufacturing process of the interface [1]. The correlation between structural and thermodynamic interfacial properties is extremely important for the basic understanding of interface stability, however, to date, understanding of this correlation is far from being complete, mainly due to experimental limitations which include specimen equilibration and transmission electron microscopy specimen preparation.

Ni-Al_2O_3 interfaces can be found in many of the applications mentioned above, but are mostly known for their use in commercial turbine blades of jet engines. Given the importance of the Ni-Al_2O_3 system, and the questions raised by numerous atomistic simulations of this system, the goal of the present work is to overcome most of these experimental limitations and to determine the structure and energy of Ni equilibrated in contact with (0001) sapphire. The effect of Hf segregation on the structure and energy of the interface will also be investigated. Such segregation is predicted to stabilize the interface.

Samples are based on thin Ni films which were dewetted in the solid-state to reach equilibrium, under careful control of impurity levels and $P(O_2)$ (i.e. partial pressure of oxygen). These specimens are used for both interface structure analysis and interface energy measurement using the Winterbottom method. Characterization of the interface

atomistic structure is mostly done by advanced techniques for quantification of transmission electron microscopy data.

The free surface of Ni was characterized in terms of energy anisotropy and composition. The effect of Fe segregation and $P(O_2)$ level was also investigated. For the first time the nickel crystal shape was determined and correlated to the chemical composition of the surface. The crystal shape was found to be almost completely facetted with both dense and high index planes, unlike other FCC metal. At $P(O_2)<1*10^{-20}$ atm, {135} and {138} facets were stabilized. Fe contamination decreased the anisotropy dramatically, de-stabilizing high-index planes.

The solid-solid interface energy was measured and aberration corrected high-resolution transmission electron microscopy was used to identify the atomistic structure of the same interfaces. It was found that the interface between Ni and (0001) sapphire undergoes reconstruction, resulting in a $2.5\sqrt{3} \times 2.5\sqrt{3}\,R30$ interfacial unit cell and the creation of shorter and stronger Ni-O bonds (lower bond energy). The energy of this specific interfacial state was determined to be 2.16 J/m^2. It is believed that the reconstructed interface accommodates the very different structures of the two bulk phases at the interface, and this is predicted to be a viable mechanism to reach a low energy interface between very dissimilar materials. To the best of the authors' knowledge, this is the first report of reconstruction at metal-ceramic interfaces.

In contrast to the existing literature, Hf was not found to segregate to Ni-alumina interfaces. Furthermore, due to the limited solubility of Hf in Ni which is different from that reported in available phase diagrams, under the current $P(O_2)$ level the Hf oxidized and formed small HfO_2 particles from which the Ni films dewetted. This is explained by the measured difference in interface energy between Ni-alumina (2.16 ± 0.2 J/m^2) versus Ni-HfO_2 (2.7 ± 0.4 J/m^2). As a result, in the experimental configuration used here, the Hf will prefer to form as HfO_2 particles on the free surface of the Al_2O_3. This Ni-Hf separation process occurs via anisotropic dewetting of the Ni film (fastest along the sapphire $\langle 1\bar{1}00 \rangle$ directions) simultaneously with HfO_2 precipitation at the Ni-Al_2O_3-ambient triple line.

List of Symbols and Abbreviations

γ	Surface energy
S_{hkl}	Surface entropy
T	Absolute temperature
Γ^{i}_{hkl}	Surface excess of solute species i
μ_i	Chemical potential of solute species i
FCC	Face centered cubic
c_i	Impurity concentration
R	Universal gas constant
$\partial\gamma/\partial\theta$	Surface/interface torque, angular variance of γ
τ	Equilibration time
D_s	Surface diffusivity
ν	Surface density of atoms
Ω	Atomic volume
γ_{MC}	Metal-ceramic interface energy
W_{ad}	Thermodynamic work of adhesion
γ_M	Metal surface energy
γ_C	Ceramic surface energy
Γ_f	Fracture energy
W_p	Plastic energy
T_m	Melting temperature
θ	Contact angle
ϕ	Dihedral angle
γ_{SL}	Solid-liquid interface energy
γ_{LV}	Liquid-vapor interface energy (liquid surface energy)
γ_{GB}	Grain boundary energy
γ_{SP}	Solid-particle interface energy
γ_{PV}	particle-vapor interface energy (particle surface energy)
γ_{int}	Interfacial energy
ECS	Equilibrium crystal shape
DFT	Density functional theory

HRSEM	High resolution scanning electron microscopy
EBSD	Electron backscattered diffraction
FEG-SEM	Field emission gun - scanning electron microscopy
CCD	Charged couple device
XRD	X-ray diffraction
TEM	Transmission electron microscopy
HRTEM	High resolution transmission electron microscopy
SAD	Selected area diffraction
FIB	Focused ion beam
HAADF	High angle annular dark field
STEM	Scanning transmission electron microscopy
APT	Atom probe tomography

1. Literature Survey

This chapter reviews the scientific background which forms the basis from which the goals and strategy of the research were derived. The chapter is divided into four sections. The first section is dedicated to surface energy of solids and equilibrium crystal shapes. The second section deals with general aspects regarding interface thermodynamics, with emphasis on interface energy measurement. The third section describes the structure of solid-solid interfaces. Finally, in the fourth section previous work from the literature is reviewed regarding Ni-Al_2O_3 interfaces.

1.1 Surface Energy of Solids

In general, an atom positioned at a surface has a higher energy than an atom in the bulk, due to unsaturated ('dangling') bonds. In order to reduce the total energy of the system, a minimization of the total surface energy is required. In the case of liquids or amorphous phases the surface energy is independent of the orientation, i.e. it is isotropic. For these materials, the equilibrium shape of a closed body, in the absence of external forces, will be that of a sphere which has a minimum surface area per volume ratio.

However, for anisotropic solids the surface energy may differ with crystallographic orientation, and the minimum energy configuration will no longer be a sphere. The change in surface energy with crystallographic orientation may be due to the number of unsaturated bonds per atom, inter-planar spacing, charge balance at the surface, and the ability of the surface planes to reduce the surface energy by rearranging the atomic structure of the surface plane (relaxation and/or reconstruction).

The solid surface energy *anisotropy* is not independent of temperature. As the temperature increases, enhanced energetic fluctuations result in increasing fluctuations at the surface plane which prevent a facet from remaining flat. As a result, the surface energy of the cusp (a local minimum in the surface energy polar plot) increases and the anisotropy decreases and approaches that of a liquid [2]. At a relatively high homologues temperature, the surface no longer behaves as a solid surface, although the bulk is still in

a solid state. The temperature at which the surface energy becomes isotropic is known as the *roughening transition,* above which the γ-plot (the surface energy polar plot) of the solid will resemble that of a liquid. For FCC metals, the anisotropy usually decreases with increasing temperature

Changes in the chemical composition of the surface also influence the surface energy. Variations in the surface composition may occur as a result of adsorption from the surrounding medium or due to segregation of impurities/dopants from the bulk to the surface. In both cases, a reduction in the surface energy takes place, which is the driving force for segregation. In the case of anisotropic surface energy, this change in composition and energy is not uniform in all orientations, causing a change in the surface energy anisotropy.

While it is normally accepted that segregation occurs to high energy surfaces in order to lower their surface energy, thus reducing the surface anisotropy (for example Au heated in carbon [3] and Cr in sapphire [4]), exceptions have been found where segregation to low energy surfaces is preferred which results in deeper cusps and higher anisotropy (for example Pb doped with Ni and Bi [5] and Cu doped with Bi [6]).

Another means of lowering the surface energy of a solid surface is by rearrangement of the surface atoms. This can be done by surface relaxation, which is a small change in the inter-planar spacing perpendicular to the surface (about 10% of the d-spacing) and in some cases may lower the surface energy of certain orientations by a factor of two [7]. Another way of reducing the surface energy is by surface reconstruction, which involves small displacements of some surface atoms in a way which alters the two dimensional surface symmetry [8,9]. Unlike relaxation, the phenomenon of reconstruction involves a change in the periodicity of the surface structure. Both processes may occur with clean surfaces in ultrahigh vacuum, but adsorption of species onto the surface may enhance, alter, or even reverse these processes.

Although many experimental methods enable the measurement of the surface energy of liquids, the surface energy of solids and its anisotropy is much more difficult to access. In order to obtain information on the actual values of the surface energy, and not only on the

anisotropy and the orientations at the cusps, an absolute value of the surface energy of at least one orientation must be known [10, 11, 12].

1.1.1 Equilibrium Crystal Shape of Solids: Wulff Construction

An understanding of surface energy anisotropy is important for many technological applications as well as for fundamental scientific reasons, including facet formation, crystal nucleation and growth, catalytic processes, thin films, surface step energy, and surface thermodynamics.

The use of γ-plots to predict the equilibrium shape of solid particles was developed by Wulff [13]. The construction of the equilibrium crystal shape (ECS), also known as the *Wulff shape,* involves drawing planes perpendicular to the normal unit vectors at each point on the γ-plot. The inner envelope of the tangents corresponds to the equilibrium crystal shape with the lowest surface energy for a fixed volume. The construction is illustrated in Figure 1 for different degrees of anisotropy.

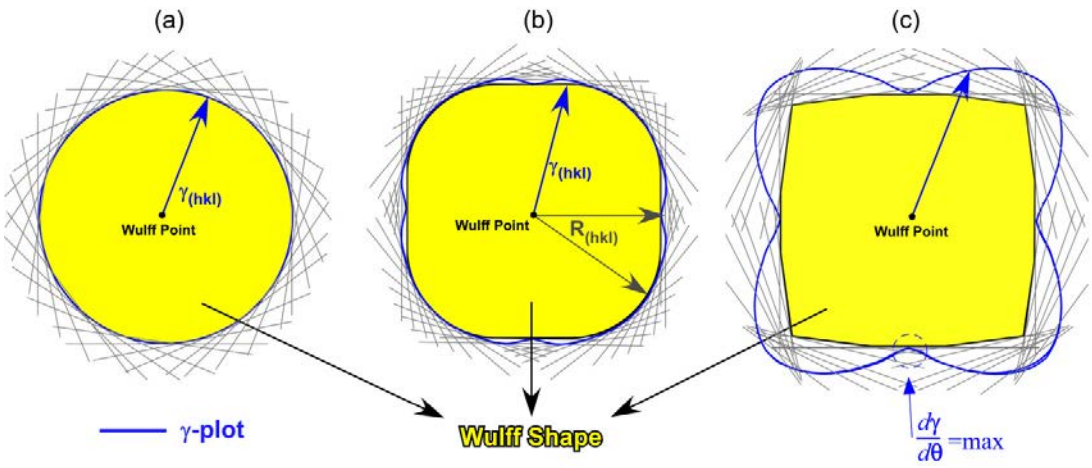

Figure 1: Wulff construction for (a) isotropic surface energy, (b) anisotropic surface energy, and (c) highly anisotropic surface energy.

The normal vectors from the center of the Wulff shape (also known as the *Wulff point*) to the surface plane can be used to calculate the relative surface energies, according to:

$$\frac{\gamma_1}{R_1}=\frac{\gamma_2}{R_2}=\ldots=\frac{\gamma_i}{R_i}=constant, \qquad \Rightarrow \frac{\gamma_i}{\gamma_j}=\frac{R_i}{R_j} \tag{1}$$

In order to obtain information on the actual values of the surface energy, and not only on the anisotropy and the orientations at the cusps, an absolute value of the surface energy of at least one orientation must be known [14, 15, 16].

The slope of the γ-plot $\left(\partial\gamma/\partial\theta\right)$ is known as the surface (or interfacial) *torque*. This parameter reflects the stability of a surface plane with respect to the surrounding orientations. In Figure 1 (a), the torque has a constant value of zero ($\gamma\left(\theta\right)$=constant). The maximum torque value is achieved at the orientation of maximum surface energy anisotropy, i.e. in the vicinity of a cusp (see Figure 1 (c)). Large torque values indicate the instability of the vicinal surfaces around the cusp. The issue of interfacial torque and its influence on the equilibrium configuration will be discussed below.

The intersection between a flat facet and a curved surface may be a sharp transition or a continuous one which contains all orientations vicinal to the facet. A discontinuous transition may be associated with deeper cusps in the γ-plot, resulting from reconstruction of low-index facets [17]. It is also possible that a smoothly curved edge will become sharp at elevated temperatures. Such a smooth-to-sharp transition has been reported for Pb between 300°C and 307ºC [18] and is associated with melting of the surfaces which occurs in all orientations except {111} and {100} (for which the roughening transition is the same as the melting temperature of the bulk). Since pure Pb does not wet the Pb{111} facet perfectly, a contact angle appears at the facet edge causing it to be sharp [8].

Since shape evolution involves diffusion processes, only relatively small crystals at high homologues temperatures will be able to reach the equilibrium form within a reasonable time-frame (limited to that of experiments). The equilibration time (τ), for a spherical particle with radius r is given by [19]:

$$\tau=\frac{r^4 kT}{24\gamma D_s \nu \Omega^2} \tag{2}$$

Where k is Boltzmann's constant, T is the absolute temperature, γ is the surface energy, D_s is the surface diffusivity, ν is the number of atoms per unit surface area and Ω is the atomic volume. The temperature dependence is manifested not only by T, but also as an exponential dependence on D_s.

Although the Wulff shape describes the lowest energy configuration of the system at equilibrium, kinetic constraints may inhibit equilibration. The key factors influencing the rate of shape evolution are the size and the temperature (manifested in equation (2) through r and D_s, respectively). However, these parameters impose practical limitations, which do not prevent the formation of an equilibrium shape, but require very long equilibration durations.

Mullins *et al.* [20] and Rohrer *et al.* [21] have shown that in order for a facet to grow or shrink, mass transport normal to the facet is required. Unless step propagating defects (such as dislocations with a screw component) intercept the surface, a nucleation barrier exists which cannot be overcome by thermal activation. As a result, the facet is prevented from reaching its full equilibrium size. This barrier is proportional to the facet size and relates to the nucleation of a step on a flat facet, from which addition or removal of atomic layers occurs. This limits the facet size to about 50%-75% of its equilibrium size. Being dependent on the facet size, this nucleation barrier becomes significant for facets which are larger than a few nanometers. On the other hand, taking into account the density of dislocations as the size of the particle increases, the probability for a dislocation to emerge from the facet surface also increases, enabling the facet to reach its equilibrium size. This results in a size dependent Wulff shape, which does not always reflect the surface anisotropy and the relative surface energies [6, 22, 23].

Equilibrated metal particles were previously used to study the surface energy anisotropy of several FCC metals such as Cu [24,25], Pb [26,27] and Au [25,26,28,29,]. In most cases, at temperatures close to the melting point, the equilibrium (Wulff) shape of the pure metals was found to be composed of the close-packed planes {111} and {100}, connected by extended rough surfaces. An exception was Cu which also exhibits (smaller) {110} and {311} facets.

Discrepancies between experimentally determined ECSs of pure metals may be related to the adsorption/segregation of extra components to the surface, originating as either a solute in the metal, adsorbed from the gas phase, or obtained from the substrate on which the crystals were equilibrated. Adsorption of one or several foreign species may take place at the metal surface and can have a significant influence on the anisotropy (and consequently on the ECS) [30-33]. The relation between adsorption and the change in surface free energy, γ is described by the Gibbs adsorption isotherm:

$$d\gamma = - \Sigma (\Gamma_i \, d\mu_i) \qquad (3)$$

where Γ_i and μ_i are the chemical surface excess and the chemical potential of component *i*, respectively. It is important to emphasize that it is not the concentration but rather the chemical potential of the solute which is correlated to surface adsorption, driven by a decrease in surface energy. This is a key-point in the case of oxygen adsorption at the surface of metals, which may take place at very low oxygen partial pressures, as directly measured for liquid metals [34], or at very low solute concentrations [35,36].

While adsorption can significantly change the ECS (i.e. the surface anisotropy), very few experiments have been conducted on this topic [33]. One of the reasons is that a very low concentration of alloy components can have a strong effect and it is often difficult to control the composition of dilute alloys [31]. As such, careful control of the experimental conditions together with chemical analysis of the surface(s) is essential for characterization of the ECS.

1.2 Interface Thermodynamics

High temperature wetting experiments are often used to extract interfacial thermodynamic data for solid-liquid systems, such as the thermodynamic work of adhesion and interfacial energies. In its simplest form, the relative surface energies of the solid-liquid system are represented by the contact angle (θ), which is often used as a comparative measure of wetting for processes in which a liquid phase is involved such as soldering, brazing, and liquid phase sintering [37] (see Figure 2).

The most common method to measure wetting is the sessile drop experiment, which is based on a liquid drop equilibrated in contact with a solid substrate. When thermodynamic equilibrium is achieved, and provided that the interface remains flat and co-planar with the substrate [38] (see Figure 2a), the contact angle (θ) can be used via Young's equation as a measure of the substrate-vapor (γ_{SV}), liquid-vapor (γ_{LV}), and substrate-liquid (γ_{SL}) interfacial energies [39]:

$$\gamma_{SV} = \gamma_{SL} + \gamma_{LV} \cos\theta \tag{4}$$

If the surface energy of the liquid is known or measured, the thermodynamic work of adhesion, W_{ad}, can be determined via the Young-Dupré equation:

$$W_{ad} = \gamma_{LV}(1 + \cos\theta) \tag{5}$$

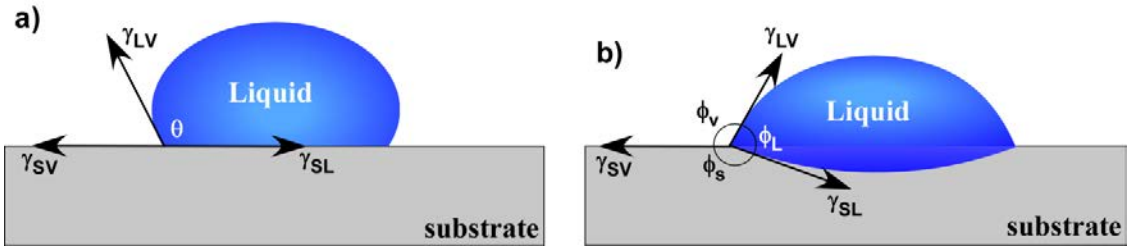

Figure 2: Schematic drawing of a liquid sessile drop on a solid substrate. (a) The solid-liquid interface is co-planar with the substrate surface and a characteristic contact angle is formed at the interface. (b) The interface morphology has changed due to capillary forces (analogous to grain boundary grooving), resulting in a dihedral angle at the triple junction.

According to equations (4) and (5), good adhesion (low γ_{SL}) is associated with relatively high surface energies (γ_{SV}, γ_{LV}). In addition to the assumption that no mass transfer occurs (flat area of contact), Young's equation is based on an energy balance only at the plane of the substrate, and ignores the $\gamma_{LV}\sin\theta$ component [40, 41]. Another parameter which is overlooked in the original form of Young's equation is the line tension (γ_{SLV}) of the triple line, which increases the measured value of γ_{SV} for a relatively small drop radius [42].

If the time and temperature of the experiment allows for mass transport (via diffusion) to take place, the area of contact (i.e. the solid liquid interface) will not remain flat and coplanar with the solid substrate (as shown in Figure 2(b)), resulting in the formation of a dihedral angle at the triple junction. These diffusion processes may include partial dissolution of the solid substrate followed by diffusion through the liquid phase, evaporation from the liquid phase and subsequent condensation, or diffusion along the interface, followed by precipitation [43]. The sine rule may be used to describe the equilibrated surface / interface energy balance via the dihedral angles [40]:

$$\frac{\gamma_{SL}}{\sin\phi_V} = \frac{\gamma_{SV}}{\sin\phi_L} = \frac{\gamma_{LV}}{\sin\phi_S} \tag{6}$$

According to equation (6), once the dihedral angles are known, only one of the surface/interfacial energies is required to determine the other two energies [40, 41, 43, 44, 45]. Contact angle analysis is much more straightforward than dihedral angle measurements, since the latter requires cross-sectioning of the interface. Obviously, contact angle analysis will be misleading if a dihedral angle is formed, which cannot be seen in conventional imaging (i.e. topographic analysis by SEM), and will surely change the apparent contact angle.

It should be noted that torque terms are neglected in the energy balance in both equations (4) and (6). While this is correct for γ_{LV}, the torque terms of the other two surface/interface energies are not necessarily zero.

1.2.1 Wetting in Practice: Sessile Drop versus Dewetting

The vast majority of wetting studies are based on sessile drop experiments, mostly due to the simplicity of the method and the straightforward relation between the drop shape and the capillarity phenomena that takes place in the system [46]. The equilibrium state of a single liquid drop on a solid substrate can be reached via two processes: the first is the sessile drop experiment which involves heating a solid particle above the melting temperature, and the second is dewetting of a thin film, which is essentially a disruption of the film under the action of its surface energy.

Typically, in sessile drop experiments, a single relatively large drop is produced. The size of the drop is limited to ~100mg in order to avoid significant deformation of the spherical shape by gravity [46]. The major advantage of this method is the ability to monitor the system *in-situ*, and acquire information regarding dynamic processes and kinetics. The main disadvantages are the lack of statistics and the requirement of a high degree of purity throughout the entire contact area [41,47] and the fact that sessile drop experiments are limited only to solid-liquid interfaces.

In dewetting experiments, agglomeration of a thin film occurs, since a contact angle of some finite value exists for the system [48]. Rupture of the film results in a very large number of isolated particles, which can be investigated separately to achieve very good statistics. The size of the droplets/particles (up to several microns in diameter) limits *in-situ* investigations, but enables shorter equilibration times and equilibration of solid particles. Obviously, the rate of rupture and equilibration in solid-state dewetting will be significantly slower than for liquid-state dewetting. It should be noted that the resulting equilibrium state of a droplet (or a solid particle) is independent of the experimental method.

1.2.2 Stable and Meta-Stable Interfaces

One of the most studied types of metal-ceramic interfaces is that between FCC metals and α-Al_2O_3 (sapphire). These interfaces are usually produced either by diffusion bonding of a pre-determined orientation, or by thin film deposition such as molecular beam epitaxy (MBE) [49,50,51]. It should be noted that these preparation techniques do not necessarily produce equilibrated interfaces. The as-bonded or as-deposited interface states often reflect a metastable interface structure and orientation, rather than a thermodynamically equilibrated state. Whether the examined interface is equilibrated or not, and whether it reflects the minimum energy configuration of the interface is rarely addressed, although this is a significant driving force for microstructural evolution of interfaces. The Nb-Al_2O_3 interface provides a good example of the influence of interface fabrication on the resulting interface orientation. Mader and Rühle [52] reported an orientation relationship of $(110)[001]_{Nb}\|(0001)[2\bar{1}\bar{1}0]_{Al_2O_3}$ for a solid-state diffusion

bonded interface, while a $(111)[110]_{Nb}\|(0001)[2\bar{1}\bar{1}0]_{Al_2O_3}$ orientation relationship was reported for the same system produced by molecular beam epitaxy (MBE) [53]. The relative stability of the different interfaces was not determined.

1.2.3 Solid–Solid Interface Energy

The measurement of solid-solid interface energies is equally important as the measurement of solid-liquid interface energies, although more difficult to access. Thermodynamic parameters of solid-solid interfaces are essential for the quantification of bond strength, fracture energy and reliability and for a better understanding of preferred orientations and crystal growth. The analysis of solid surfaces and interfaces requires a different approach than that of liquids, since solid surface and interface energies can be anisotropic and have a facetted rather than a round equilibrium shape, making the interpretation of wetting experiments more complex. There has been a long tradition of extracting thermodynamic data from contact angles of molten metals on ceramic substrates, and then attempting to relate these thermodynamic properties to the adhesion of the solid interfaces formed from the same materials. This approach has been a failure mainly due to the orientation dependence of interfacial segregation and energy. According to Howe [54], the difference in surface energy of *rough* surfaces above and below the melting point is about 20%. This discontinuity in surface energy variance with temperature illustrates the problematic correlation of solid-solid and solid liquid interfaces.

Preferred orientation and orientation relationships result from energy minimization usually associated with matching of planes or dictated by symmetry. Most often close packed planes and directions are aligned across the interface. In order to quantify the effect of surface chemistry and crystallography on the interface energy and adhesion, a rigorous methodology is required. The most frequently used methods are discussed in the next sections.

1.2.3.1 Dihedral Angle Measurement

The energy balance at a triple line between two (or three) *solid* phases was first presented by Herring [55]. This approach is based on geometrical analysis of the equilibrium configuration around a triple line, resulting from an energy balance of the three surface/interface energies, according to:

$$\sum_i \gamma_i \hat{t}_i + \frac{\partial \gamma_i}{\partial \beta_i} \hat{n}_i = 0 \qquad (7)$$

Where γ_i is the free energy per unit area of the ith interface, $\hat{t}_i$ is the unit tangent of the ith interface at the point of intersection with the triple line l, $\hat{n}_i$ is the unit vector normal to the triple line and to the interface tangent (such that $\hat{n}_i = \hat{l} \times \hat{t}_i$) and β_i is the angle of rotation about l for the ith boundary [56]. Figure 3(a) illustrates such an energy balance perpendicular to the line l for the case of a grain boundary groove.

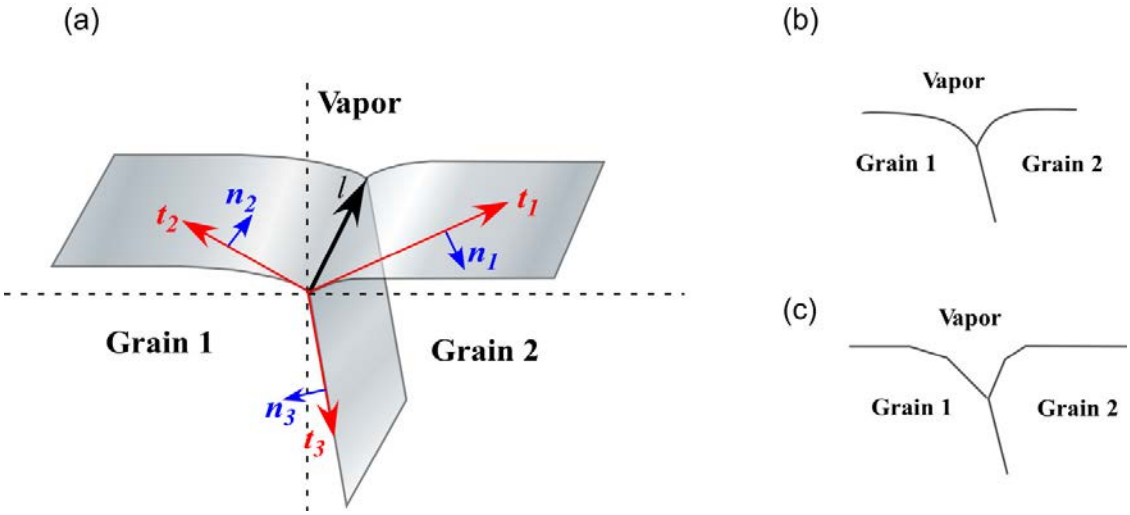

Figure 3: (a) Schematic perspective drawing of a triple junction (after Saylor and Rohrer [56]). (b) Grains with isotropic surface energies result in a rough triple junction. (c) Cusps in the γ-plot result in a faceted triple junction.

The derivative terms $\frac{\partial \gamma_i}{\partial \beta_i}$ in equation (7) is the interfacial torque, which reflects the dependence of interface energy with orientation about the triple line *l*. A cusp in the (interfacial) γ-plot will induce a faceted morphology of the interface adjacent to the triple line (see Figure 3 (c)). In the isotropic case, $\frac{\partial \gamma_i}{\partial \beta_i} = 0$ and so only the first term in equation (7) remains, and Herring's equation reduces to the analysis of dihedral angles in solid-liquid interfaces, as seen in equation (6) [57]. The major drawbacks of this method are the fact that only relative surface energies are normally obtained, and the rather complex calculations required to estimate the value of torque [58] often leads to abandoning these terms.

1.2.3.2 Winterbottom Analysis

Another theory which can be used for the measurement of solid-solid interfacial energy was developed by Winterbottom [59]. This approach is based on geometrical analysis of the Wulff shape of a single crystal equilibrated on a solid substrate of a dissimilar material. The analysis is based on surface and interfacial energy considerations of an equilibrated particle on a foreign substrate, under conditions of constant temperature, volume and chemical potential.

In his analysis, Winterbottom reduced the problem of determining the equilibrium shape of a particle equilibrated on a substrate to a much simpler problem of determining the equilibrium shape of an ***equivalent*** particle with a surface energy γ*. The interfacial energy can thus be determined by measuring two characteristic lengths in the Wulff shape: the distance from the center of the Wulff plot (i.e. the Wulff point) to the interface with the substrate (R_1), and the distance from the Wulff point to the uppermost facet of the particle (R_2), as shown schematically in Figure 4.

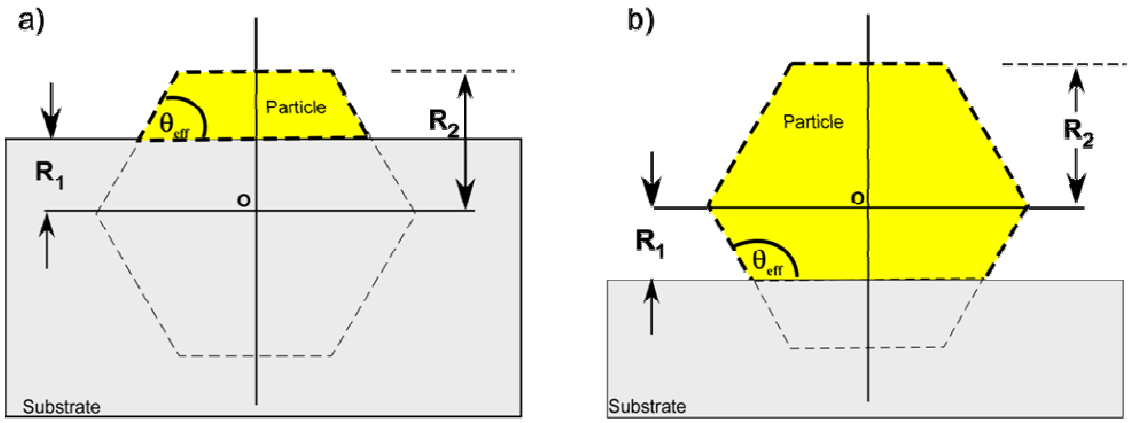

Figure 4: Schematic drawing of the Winterbottom analysis for particles equilibrated on a substrate, having different effective contact angles; (a) θ < 90° and (b) θ > 90°. The dashed polyhedron indicates the resulting equilibrium Wulff shape and its center O (the Wulff point). R_1 and R_2 are the distances from the Wulff point to the interface with the substrate and to the uppermost particle facet, respectively.

For an effective contact angle larger than 90°, measured values of R_1 and R_2 can be used to determine the interfacial energy according to:

$$\frac{R_1}{R_2} = \frac{\gamma_{sp} - \gamma_{sv}}{\gamma_{pv}} \tag{8}$$

where γ_{SP} is the substrate-particle interfacial energy, γ_{SV} is the surface energy of the substrate, and γ_{PV} is the surface energy of the uppermost particle facet [59,60]. A more detailed description of this calculation is given in Appendix I. According to Cahn, interfacial torque terms are included in the measured energy value, provided the interface is flat and coplanar with the substrate [61]. Although Winterbottom's analysis provides a relatively simple methodology for the measurement of γ_{SP}, experimental limitations have prevented widespread applications. The major limitation arises from the demand that the examined system consist of a ***single-crystal*** particle thermodynamically ***equilibrated*** and having a ***flat*** interface which is co-planar with the substrate surface [61]. The requirement for equilibration (in a reasonable time-frame), in addition to the absence of grain

boundaries, limits the particles size. This poses a challenge regarding the characterization techniques for high accuracy morphological analysis. In order to determine the interface energy, the orientation of both the particle and the substrate must be known.

This method was recently employed by Sadan and Kaplan to Au-Al_2O_3 interfaces [62]. It was found that the energy of Au (111) $[2\bar{2}0]$ ‖ sapphire (0006) $[2\bar{1}\bar{1}0]$ interface at equilibrium is 2.16±0.02 J/m^2.

The use of equation (8) requires knowledge of the absolute values of the relevant surface energies. In the case of a particle on a foreign substrate, segregation may often occur resulting in chemical changes at the surfaces and a decrease in the surface energies. Determination of the surface composition and measurement of the relevant surface energies is a major obstacle. Usually, the effect of segregation is ignored despite the resulting inaccuracy of the results.

1.3 Interface Structure

The complexity of solid-solid interfaces arises not only from the difference in long rang atomistic order on both sides of the interface, but also from the wide variety of defects that can form, and the unique structural and compositional characteristics of each interface, depending on the relative orientation of the two crystals, the compositions, the temperature and sometimes even the manufacturing process of the interface [63]. This degree of complexity often inhibits quantitative treatment of interfacial phenomenon.

Due to the different atomistic arrangement at both sides of the interface, misfit strain inevitably develops. If kinetically possible, the system will work to reduce this strain by either introducing misfit dislocations or steps (to create a semi-coherent interface), or alternately, by the formation of an incoherent interface. While the presence of misfit dislocations is widely reported at metal-ceramic interfaces, only a single report was found regarding incoherent metal-ceramic interfaces [64].

1.3.1 Macroscopic and Microscopic Degrees of Freedom

An interface can be described by the boundary plane and relative rotation of the crystals. Thus a boundary has 5 *macroscopic* degrees of freedom; two are used to define the boundary plane and three additional parameters are needed to define the 3D rotation required to bring one crystal into atomic coincidence with the other.

In addition, the structure of the interface can be described by its microscopic properties that are usually related to the atomistic arrangement at the interface. These include the following parameters:

- Translation state of the two crystals.
- Termination of the boundary plane.
- Relaxation, which is a small change in the inter-planar spacing perpendicular to the interface.
- Reconstruction, which is a change in the periodicity (symmetry) of the interface plans.

1.4 The Ni–Al_2O_3 System

1.4.1 Ni–Al_2O_3 interface

In addition to being a model metal-Al_2O_3 system, Ni-Al_2O_3 interfaces can be found in numerous technological applications, such as composites, microelectronic packaging, catalytic processes and applications demanding high temperature strength and oxidation resistance such as turbine blades [65,66,67].

In contrast to the large technological importance of this system, Ni-Al_2O_3 interfaces were not experimentally studied to the same extent as other metal-alumina interfaces. This is mainly because of the relative high melting temperature of the metal and/or because of the relatively large surface energy of Ni, which requires an extremely pure environment for model studies [68,69]. Resolving the detailed atomistic arrangement at the interface is an extremely important and challenging task which is crucial for the understanding of interface-related phenomena. Unfortunately, the limitations of atomistic analysis

techniques, especially for case of interfaces, are the main reason for the lack of experimental data that can help to better understand the structure and chemistry of interfaces.

Due to the lack of experimental data available, numerous atomistic simulations (mostly DFT) were performed as an attempt to simulate the atomistic and electronic structures at Ni-Al_2O_3 interfaces, as well as other properties such as the work of separation, the work of adhesion and interfacial energy [67,70,71,72,73,74,75]. In order to conduct these simulations within a reasonable time, some information regarding the macroscopic properties of the interface was required ***a priori***. This includes the orientation relationship and the interface planes, and sometimes also microscopic parameters such as interface termination and translation of one crystal with respect to the other. However, as was mentioned above, reliable experimental data on Ni-Al_2O_3 interfaces is not available. As a result, all of the published simulations on Ni-Al_2O_3 interfaces are actually based on parameters of similar interfaces such as diffusion-bonded Nb-Al_2O_3 interfaces or Cr-doped Ni-Al_2O_3 interfaces [75,76]. The fact that these experimental results do not reflect equilibrated Ni-Al_2O_3 interfaces, including both the structure and chemistry, raises doubt on their use as the starting point for DFT simulations. It was almost always assumed that the interface is semi-coherent (with the exception of [73]) and the calculations were performed on a small section of the interface in which the crystals are either stretched or compressed to be coherent.

Zhang et al. calculated the stability of the (111)Ni-(0001)Al_2O_3 interface, with Al dissolved in the Ni, as a function of Al activity and P(O_2), using ***ab-initio*** calculations [77]. The results are presented in Figure 5.

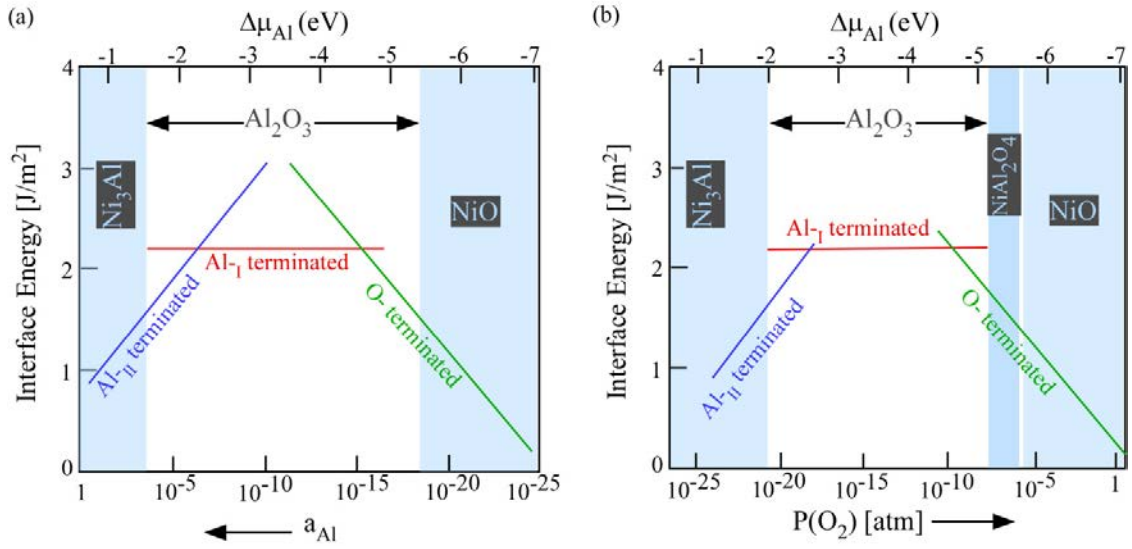

Figure 5: Calculated interfacial energy of (111)Ni(Al) – (0001)Al_2O_3 at 1027°C, with different terminating planes as a function of (a) Al activity, and (b) P(O_2). Redrawn after Zhang, Smith and Evans [77].

According to the simulations, it was found that the most stable interface over a wide range of Al activity and P(O_2) was the one in which the (0001) sapphire was terminated by one Al layer ($Al-_I$). At this interface, the Ni atoms are located directly above and strongly bonded to the oxygen atoms, similar to bonds in NiO (even though the Al plane partially saturated the oxygen dangling bonds). The $Al-_{II}$ termination was stabilized at a high activity of Al and low P(O_2) by the presence of Ni_3Al-like and Al_2O_3-like bonds. At high P(O_2) and a low a_{Al}, the O-terminated interface is stabilized as the Ni atoms are located at the first Al layer sites and the next Ni layer is buckled [78]. These results were compared to experimental results of interfacial strength and were found compatible. However, no experimental evidence of the proposed atomistic structure was found.

Long et al. [73] examined the structure of Ni-Al_2O_3 interfaces that are not constrained by commensuration, using an energy minimization technique, and were able to predict the existence of a reconstructed Ni layer at the interface that absorbs the misfit strain energy. Unlike DFT, this method is not limited by size. This alternative interface structure provides an alternative mechanism for strain energy reduction and the formation of shorter and stronger Ni-O bonds.

Trumble *et al.* [79] showed that the formation of an *interphase* depends on the oxygen activity, and that above some threshold value nickel aluminate spinel forms. The calculated threshold value as a function of oxygen partial pressure at 1400ºC is shown in Figure 6.

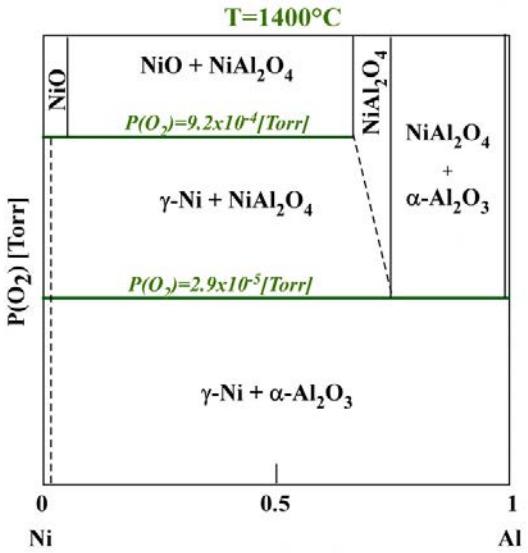

Figure 6: Ni-Al-O phase diagram at 1400ºC (after Trumble and Rühle [79])

Brydson *et al.* [80] experimentally confirmed the calculated threshold value using analytical electron microscopy. The formation of spinel creates two interfaces instead of the original one. The spinel-Al_2O_3 interface is relatively strong (mechanically), but the Ni-spinel interface is weaker than the Ni-Al_2O_3 interface. An interesting question raised by Brydson *et al.* is whether a spinel phase at the nanometric length scale exists at the interface even under the threshold value. The presence of such a phase (or interface) would be expected to affect the interfacial properties, and thus this issue requires further study with more advanced microscopy and spectroscopy techniques.

1.4.1.1 Liquid–Solid Ni–Al_2O_3 Interfaces

The thermodynamic properties of pure Ni-Al_2O_3 interfaces at different compositions of the Ni alloy were mostly investigated through wetting experiments [81-88]. The wettability of a sessile drop on a solid substrate is an important parameter for understanding high temperature processes, in which a liquid metal is involved, such as infiltration, brazing, soldering, liquid-phase sintering, etc. Since a decrease in interfacial energy will result in a smaller contact angle, the correlation of better wetting (i.e. smaller contact angle) with a more energetically stable interface is the most widespread method of assessing thermodynamic properties of an interface.

In previous wetting experiments, it was found that the contact angle between liquid Ni and the basal plane of Al_2O_3 at 1500ºC in UHV is 112±3º. No significant change in the contact angle was reported with the orientation of the sapphire substrate [89]. Levi ***et al.*** examined the structure of the Ni-Al_2O_3 interface at 1500ºC and $P(O_2)$ $<10^{-9}$ Torr, and confirmed that no interfacial phases are present, and that the interface appears to be smooth [47]. However, the systematic presence of Al excess equivalent to 1–3 atomic monolayers was detected at the Ni-sapphire interface, as well as segregation of Al and O from the substrate to the free surface of the Ni [90].

1.4.2 Ni–Al_2O_3 Interfaces in Commercial Turbine–Blades

Ni-Al_2O_3 interfaces are widely used as oxidation barriers for Ni-based super-alloys in turbine blades for jet engines. In order to improve the durability of this interface, a number of reactive additives (such as Cs, Y, La, Zr and Hf) are added to the Ni-based super-alloys (usually less than 1 at.%), which are known to segregate to the Ni-alumina interface (and often oxidize).

Commercial thermal barrier coating (TBC) systems typically consist of three different coating layers that protect the superalloy from the extreme working conditions (see Figure 7). The outer-most layer is a ceramic top coat made of yttria-stabilized zirconia (YSZ) which is a very good heat insulator (but unfortunately also a good oxygen conductor). Below the YSZ layer, a thermally grown oxide (TGO) is formed, which is

essentially a several micron thick oxide scale (primarily α-Al_2O_3) that provides oxidation protection. The underlying bond-coat is composed mainly of Ni but also contains other elements such as Cr, Co, Y and Al from which the protective oxide scale is grown. The poor mechanical adhesion at interface between the Al_2O_3 scale and the Ni-based bond-coat is the main cause for mechanical failure of turbine blades.

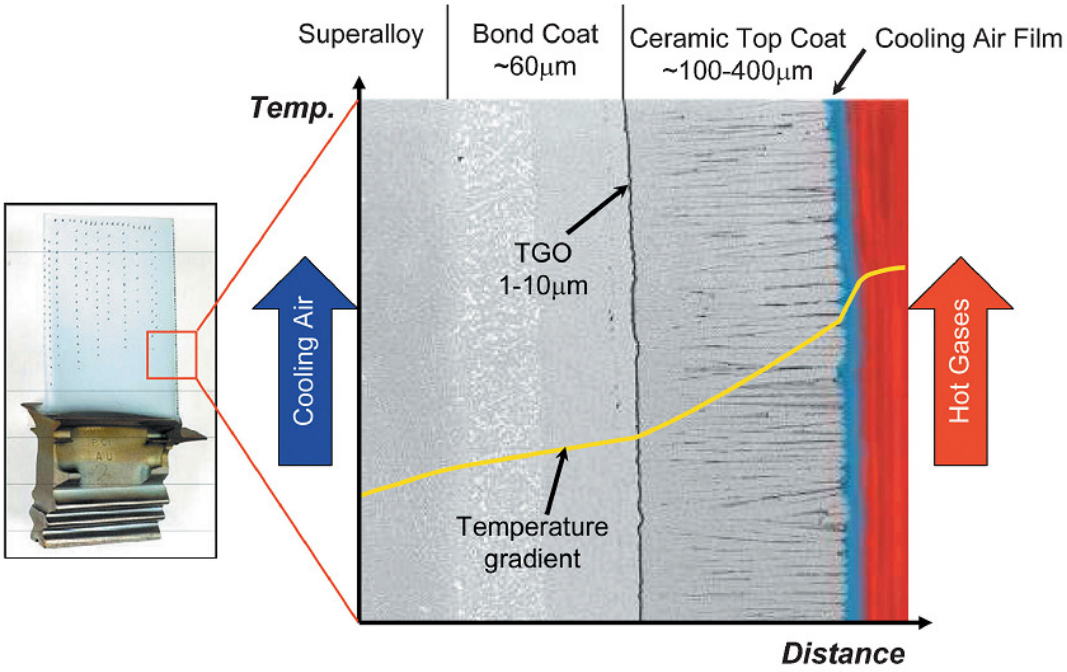

Figure 7: SEM cross-section of the various layers used to protect Ni-based turbine blades: Bond-coat; thermally grown oxide (TGO); and ceramic top coat. The yellow line represents qualitatively the temperature gradient superimposed on the cross-section during operation. Taken from [91].

1.4.3 Hf-Doped Ni-Al_2O_3 Interfaces

While the presence of small amounts of Hf in commercial Ni-Al_2O_3 interfaces is known to improve its mechanical integrity, the mechanism behind this is not clear. Several explanations were proposed, including impurity scavenging (mostly S and C) [92,93,94], reduction of oxide growth rate [95,96,97], improved resistance to cyclic fatigue [98] or direct improvement of interfacial bonding [99,100]. This issue has been studied to a great extent, for a large variety of bond-coat alloys. The dominating mechanism responsible for

adhesion improvement by Hf is greatly affected by the presence of other dopants in the alloy and the resulting microstructure.

Simulations were also made in order to model the influence of Hf on the thermodynamic work of adhesion and the work of separation of the interface. The results are contradicting: Bennett *et al.* [101] modeled the NiAl-Al_2O_3 interface and found that the presence of Hf does not cause a significant change in the W_{ad}, while Jiang and Smith [100] used DFT simulations to clearly show that Hf segregates to the interface (i.e. a thermodynamic driving force exists) and increases the work of separation (W_{sp}) by a factor of 3, directly improving interfacial bonding.

1.4.4 Ni Surface Energy

Careful control of the experimental conditions together with chemical analysis of the surface(s) is essential for characterization of the ECS. This is especially true for Ni, due to its high surface energy which acts as a driving force for surface segregation [31,102], and the relatively high annealing temperature required for equilibration compared to other metals. The difficulty in achieving *pure* and *equilibrated* Ni particles could be the reason why the ECS of Ni was not studied to the same extent as other FCC metals.

Knowledge of the surface composition and energy of solids is important not only to understand surface-related phenomena, but also for interface research, since in order to measure the interface energy, the absolute surface energies in the system must be known (see equations (7),(8)).

Recently, the ECS of dewetted Ni particles was investigated by Hong *et al.* [103]. Surprisingly, they found that at equilibrium, the most stable surface is {210} (which is usually the highest low index surface energy for FCC metals [31]), followed by {110}, {111}, {100} and {320}. In these experiments, the initial Ni film contained a total of 100 ppm of impurities, to which Si resulting from the use of a quartz tube furnace was added. No chemical analysis was performed on the equilibrated particles. In our opinion the ECSs of Ni determined by Hong *et al.* was modified by adsorption.

Mykura used the geometry of twin boundary grooves in Ni annealed for 50-100 hours at 1273 K (0.75 Tm) in vacuum to experimentally determine surface anisotropy and found that the lowest energy surface was for {100}, followed by {111} ($\gamma_{(100)}/\gamma_{(111)} = 0.95 \pm 0.03$) [104]. The maximum anisotropy found at this relatively low equivalent temperature was 8.5 ± 2%. The purity of the Ni sheets was not reported, nor was the vacuum level (partial pressure of oxygen) used for annealing. While the measured anisotropy was consistent with the expected increase of anisotropy with temperature [30], the lack of surface chemical analysis prevents any comparison of Mykura's results with similar experiments. Sundquist used Ni particles equilibrated on BeO for up to 100 hours at 1273 K to investigate the Wulff shape in two different atmospheres: vacuum and dry H_2 [25]. Although no quantitative measurement of the anisotropy was made, {111} and {100} facets were identified in both atmospheres. However, the particles equilibrated in vacuum had almost no rounded surfaces and were almost completely faceted, while the particles equilibrated in H_2 had rounded surfaces with sharp edges connecting the facets. The authors attributed this difference to anisotropic O_2 or H_2 adsorption, respectively (although H_2 does not adsorb on the surface of Ni at this temperature [105]). No surface analysis was done to validate this assumption. In another report, Barsotti ***et al.*** investigated the ECS of a Ni field emission tip at 1300K and were able to measure the anisotropy of low index facets as well as rounded surfaces [106]. Emphasis was made on the measurement of surface impurities and only tips that were found to have clean surfaces were investigated. However, due to the initial geometry of the tips the resulting shape may have not been the ***equilibrium*** shape but rather that correlated with steady state, and thus only the facets at the apex were investigated. Barsotti ***et al.*** determined that the {111} facet has the lowest energy, followed by {001}, and a maximum anisotropy of 3%.

2. Research Goals

The main goal of this research is to address the questions that were raised in the literature survey by characterizing the full atomistic structure of equilibrated Ni-Al_2O_3 interfaces, and in parallel to measure the solid-solid interface energy of the *same* interface. By employing new analytical tools and developing methods to improved specimen preparation, most of the experimental obstacles that existed in the past were overcome. The use of these techniques will help to clarify and quantitatively assess the influence of interface bonding and structure on energy and adhesion. The effect of Hf segregation on the structure and energy of the interface was also studied.

Methodology:

Equilibrated solid-state Ni-Al_2O_3 specimens were prepared by dewetting experiments. TEM specimens were prepared by FIB combined with conventional broad ion-milling. Equilibrium shape analysis that is needed for the energy measurements was determined using TEM. Atomistic analysis of the interface was conducted by HRTEM using exit plane wave function reconstruction.

3. Experimental Methods

This chapter describes the equipment, materials and methodology that were used to conduct, control, investigate and interpret the experiments during this research. The experimental approach is based on of solid-state dewetting experiments conducted under carefully controlled working conditions.

The chapter is divided into four sections. The first section deals with the experimental equipment and solid state dewetting of Ni. In addition, the introduction of Hf to the Ni-Al_2O_3 system is described. In the second section, TEM specimen preparation is described, with emphasis on an experimental technique that was developed to improve the specimen quality. The following section describes the characterization methods that were employed. Finally, in the last section, a unique method to experimentally measure the thickness of TEM specimens is described.

3.1 Dewetting Experiments

The experimental challenge in this research is to create a configuration from which a thermodynamic parameter (interface energy) of an equilibrated system can be extracted, in addition to the atomistic structure and chemistry of the same interface.

Solid-state dewetting was chosen as the basic experimental approach for this study not only because it allows for reasonable equilibration times for solid Ni (no more than a day), but also because it provides a huge number of equilibrated Ni-Al_2O_3 particles which can be examined independently. This is extremely important for TEM specimen preparation which is a destructive technique and often requires several attempts to prepare a specimen appropriate for the more advanced TEM methods. In addition, the large number of particles offers better statistics and allows for producing specimens in several complementary projections perpendicular to the interface.

Special emphasis was made on keeping the system as clean as possible from impurities that may alter the structure and properties of the system.

3.1.1 Ni Thin Film Deposition

(0001) oriented sapphire (α-Al_2O_3) substrates of 99.99% purity were provided by Gavish Industrial Technologies & Materials (Omer, Israel). Substrates were ultrasonically cleaned in acetone and ethanol. Ni films (120-250 nm thick) were deposited on the substrates by magnetron sputtering or by e-beam deposition (99.99% and 99.9995% pure, respectively). The resulting film morphology can be seen in Figure 8. Magnetron sputtering produced columnar structure and a highly irregular surface, with grooves as deep as the film thickness, while e-beam deposition produced a layer with a uniform thickness. The initial morphology of the film was found to have a dramatic influence on the resulting dewetted particles; the columnar structure of the sputtered Ni resulted in polycrystalline Ni particles whereas the e-beam deposited film resulted in single crystalline and uniformly textured Ni particles.

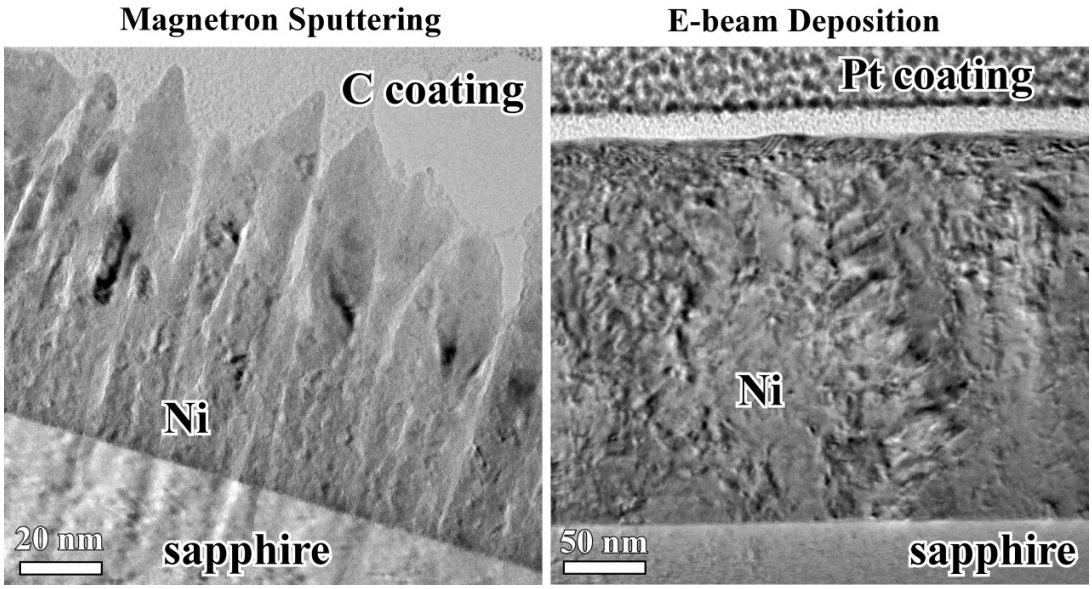

Figure 8: Bright field TEM micrographs of the Ni film deposited by magnetron sputtering or by e-beam deposition.

The specimens were dewetted and further annealed in the *solid* state (between at 1572-1623 K) to form a large number of particles with a diameter ranging from 100 nm to a few microns (see Figure 9), and were cooled at a rate of 15-20 K/min.

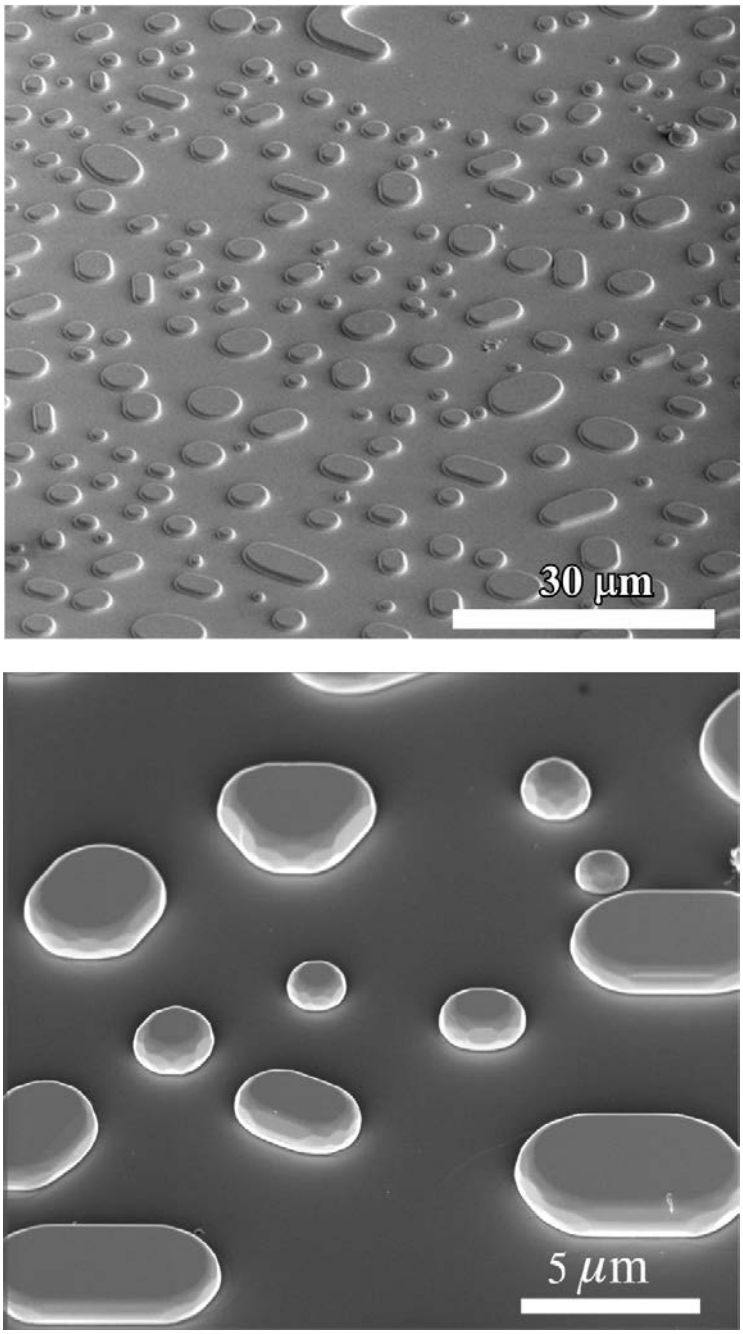

Figure 9: Ni particles after dewetting on (0001) sapphire for 5 hours at 1623 K in Ar+7%H_2. Only the particles smaller than 1 µm are equilibrated (deposited by e-beam deposition).

In order to carefully control the experimental conditions of the dewetting experiments, with focus on the $P(O_2)$, two special furnaces were used.

3.1.1.1 UHV dedicated wetting furnace

A dedicated UHV furnace was used for accurate control of the temperature, total pressure and partial pressure of gasses.

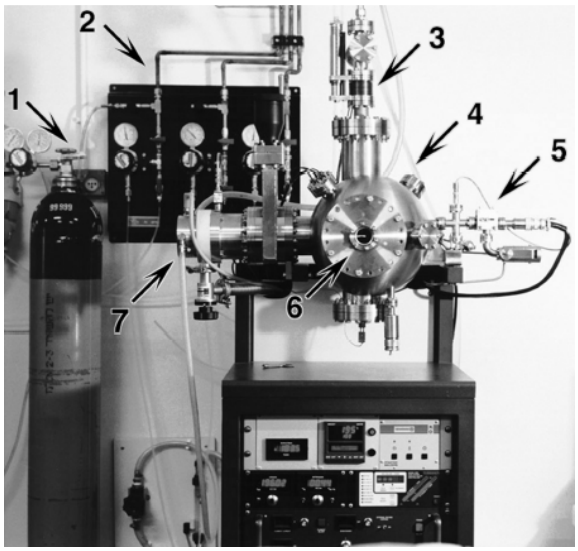

Figure 10: The dedicated UHV wetting furnace. 1) gas supply; 2)gas control panel; 3)heater axis; 4)UHV chamber; 5)ion gun (Ar+, 0-3 kV); 6)quartz window; 7)turbo-molecular pump.

The specimen is located in the central part of the furnace on a tungsten stage, and a tungsten filament is wrapped in a cylindrical shape around it. The filament and specimen area is covered by concentric cylindrical heat shields which limit the loss of heat and prevent overheating within the chamber. The heat shields have a 5mm X 20mm slit to allow *in situ* observation of the specimen.

3.1.1.2 Dedicated dewetting furnace

In order to further decrease the $P(O_2)$, a series of dewetting experiments was carried out in a specially modified furnace. Due to the high sensitivity of the experiments to impurities, special attention was given to the surrounding of the specimen.

The purity of commercial alumina tubes that are used for furnaces is usually no more than 99 % and often SiO_2 and CaO are present as impurities. The presence of these impurities in the hot zone will contaminate the specimen. In order to prevent this, a

unique tube-in-tube configuration was built, in which six 99.99% pure single-crystal *sapphire* tubes were purchased and assembled to allow gas flow into the hot-zone with a slight overpressure (slightly above 1 atm). This system allows for high temperature anneals at atmospheric pressure using Ar+7vol/%H_2 (99.9999% pure, supplied by Gas Technologies LTD, Israel) giving a $P(O_2)<10^{-20}$atm. The $P(O_2)$ was measured at the exit port of the furnace using a zirconia oxygen detector. The $P(O_2)$ at the hot zone was calculated according to the temperature difference between the detector and the hot-zone (see the calculation is given in appendix 9). A schematic representation of the modified furnace is presented in Figure 11. The joints between the sapphire tubes were produced at the Technion from 99.99% pure alumina powder.

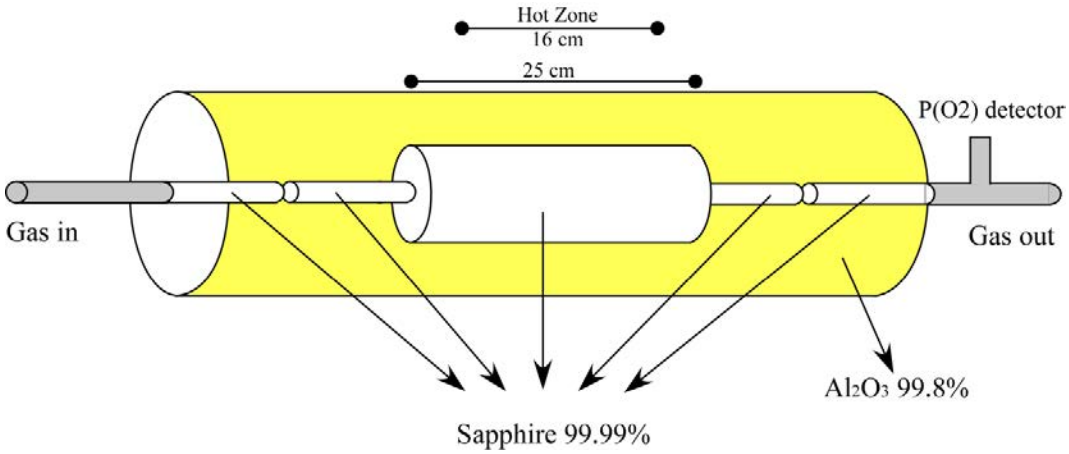

Figure 11: Schematic drawing of the tube-in-tube configuration. The outer tube is made of 99% pure polycrystalline alumina (yellow), and the five inner tubes are made of 99.99% pure sapphire with varying diameters.

3.1.2 Dewetting Pure Ni on Al_2O_3

Three different annealing procedures were performed in order to examine the influence of $P(O_2)$ and the purity of the Ni particles on the equilibrium shape. In all cases, the total pressure was at least one order of magnitude larger than the vapor pressure of Ni (to limit evaporation) and the $P(O_2)$ levels were below the threshold for Ni oxidation or Ni-spinel formation (i.e. $P(O_2)<3*10^{-9}$ atm.) [107]. The experimental conditions in which the three specimens were prepared (marked here after as systems A, B, C) are given in Table 1.

Table 1: Experimental conditions used to equilibrate the Ni particles.

System	Atmosphere (dynamic flow)	Deposition Method (Ni purity)	Measured $P(O_2)$ [atm]	Annealing temperature	Time at temperature	Texture
A	Ar	Sputtering (99.99%)	$1*10^{-9}$	1300°C	30 minutes	{100}
B	Ar + 7vol.% H_2 (+Fe**)	Sputtering (99.99%)	$<10^{-20}$	1350°C	120 minutes	{111}
C	Ar +7vol.% H_2	e-beam deposition (99.9995%)	$<10^{-20}$	1350°C	300 minutes	{111}

***The furnace used in system B was contaminated with Fe.*

3.1.3 Dewetting Hf-doped Ni films on sapphire

E-beam deposition was used to coat the substrate with Ni and Hf layers (99.9995% and 99.99% pure, respectively) at different thicknesses in order to control the relative amount (concentration) of Ni and Hf (giving 0.5at.% and 5at.% Hf). The total thickness of the layers was 120-350 nm. The specimens were dewetted for 3-5 hours at a temperature of 1623K and were then cooled to room temperature at a rate of 15-20 K/min. To maintain the highest purity possible, and to control the oxygen partial pressure during equilibration, dewetting was conducted in the modified dewetting furnace (as described in section 3.1.1.2), under a partial pressure of oxygen of $1.6x10^{-20}$atm (possibly even lower).

3.1.4 Dewetting Ni on HfO_2 and Al_2O_3

In a separate series of experiments, HfO_2 particles (sub-micron in length-scale) were formed on (0001) sapphire substrates by depositing a very thin Hf film (approximately 1 monolayer) and subsequently annealing for 5 hours at 1623K ($P(O_2)=1.6*10^{-20}$atm). As a result, the Hf oxidized and dewetted, uniformly covering the sapphire substrate with

HfO_2 nanoparticles (approximately 10-20% coverage). Following this process, Ni was deposited and then dewetted under the conditions listed in section 3.1.3.

3.1.5 Dewetting Ni on HfO_2

In order to achieve a clean and relatively flat HfO_2 substrate, a thick Hf layer (700nm) was deposited on sapphire and was heat treated under the same conditions listed in section 3.1.3. Due to the large thickness of the layer, the layer was completely oxidized but did not break-up within the time-frame of the experiment (i.e. dewetting did not occur). A Ni film was then deposited on top of the specimen and dewetted (according to the procedure given in section 3.1.3).

3.2 TEM Specimen Preparation

A dual-beam focused ion beam (FIB, Strata 400 s, FEI) equipped with a field emission gun (FEG) electron source (operated at 3-30 kV), a Ga^+ ion beam (2–30 kV), an in-situ nanomanipulator (Omniprobe, AutoProbe 200) and a scanning transmission electron microscopy (STEM) detector was used for preparing TEM specimens from the center of particles with a known morphology and orientation using the in-situ "lift-out" technique [108,109]. The particles were sectioned across the Wulff center and in a direction carefully chosen to intersect specific surface facets. This was important for subsequent *edge-on* imaging of the facets by TEM. The particles were initially covered with a protective layer (Pt or C) deposited using the electron beam in the FIB, in order to prevent surface damage by the ion beam.

Particles for TEM specimen preparation and subsequent analysis were selected according to the following criteria:

1) Particle size: Since the shape evolution involves diffusion processes, only relatively small crystals at high homologous temperatures will be able to reach an equilibrium shape within a reasonable time-frame. The equilibration time, for a particle with radius r is given by equation (**2**).

2) Particle orientation and sectioning direction: The selected Ni particles were positioned in such a way that the sectioning direction was normal to the facet planes (and goes through the Wulff center of each particle). This allowed for ***edge-on*** imaging in the TEM, identification of the facets by electron diffraction, and correct measurement of surface energy anisotropy on a section of the Wulff shape.

3) Particle microstructure: Only single crystal particles, without grain boundaries, were selected and analyzed.

3.2.1 Improving TEM Specimen Quality

Although the use of FIB for TEM specimen preparation provides very accurate site-specific specimen preparation, the resulting specimen quality is quite poor; the thickness of the specimens is rarely below 50nm and the surface is damaged by the Ga beam. This poses a significant limitation on extracting quantitative TEM data. Clearly, the use of conventional specimen preparation which involves broad ion beam polishing is not applicable for this experimental system.

In order to improve the quality of FIB prepared specimens, conventional low voltage ion polishing was used for the final polishing stage. In order to eliminate re-deposition of the grids (usually made of Cu or Mo), a circular Ti grid (with a much slower sputtering rate) was cut and used to support the TEM lamella (Figure 12). Conventional ion-milling was done using 0.3kV Xe^+ ions (Linda Ion Miller, Technoorg) at an incident angle of ±8°. The specimen was milled from the sapphire side, which has a much slower sputtering rate than that of Ni.

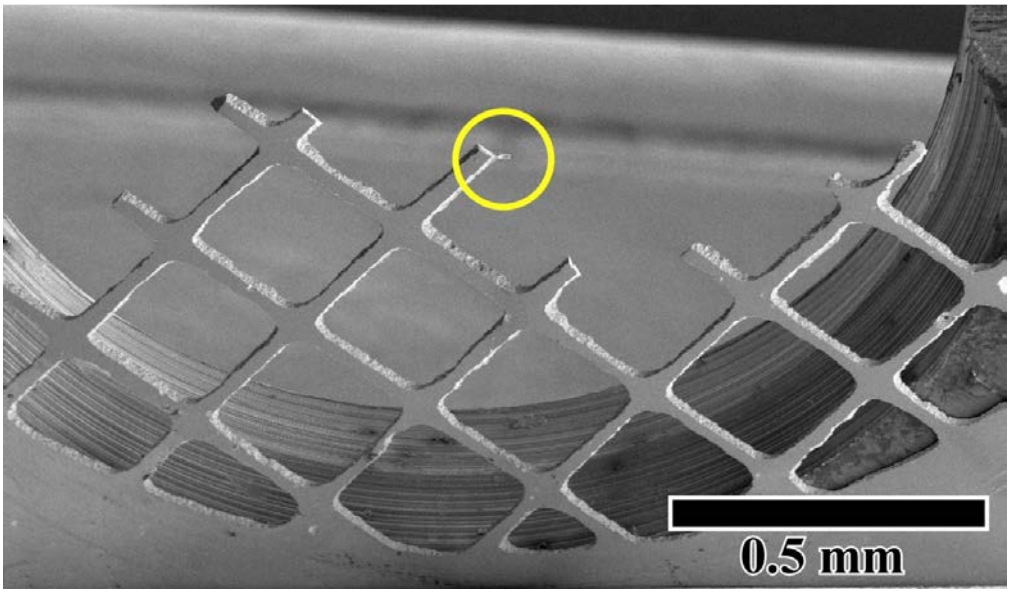

Figure 12: Conventional Ti grid for TEM. The grid was cut manually and a TEM lamella was attached using FIB (the lamella is seen in the yellow circle).

3.3 Characterization Methods

3.3.1 X-Ray Diffraction

The Ni particle texture was analyzed by X-ray diffraction (XRD), using Cu Kα radiation operated at 40 mA and 40 kV (Philips X'Pert goniometer). A θ-2θ coupled Bragg-Brentano geometry was used for analysis of integrated intensities and the preferred orientation of Ni reflections relative to the sapphire substrate.

3.3.2 TEM

The morphology of the particles was examined by TEM using a monochromated and aberration corrected FEG-TEM (FEI Titan 80-300 S/TEM) operated at 300 kV. Kikuchi electron diffraction was used to align the Ni particles in a low-index zone axis prior to acquiring selected area electron diffraction (SAD) patterns.

High-angle annular dark-field scanning transmission electron microscopy (HAADF-STEM) was also used. By using a STEM detector with a large inner radius, a HAADF

detector, electrons are collected which are not Bragg scattered. As such HAADF images show little or no diffraction effects, and their intensity is approximately proportional to Z^2.

At the beginning of each TEM experiment, in addition to standard alignments, correction of the spherical aberration was conducted on FIB deposited carbon using the CEOS software [110]. Using this software, optical adjustment of the electron microscope's hexapole corrector was performed, which provided the desired spherical aberration value (which was at times set to negative values [111]), and even other higher order aberrations (two-fold astigmatism, three-fold astigmatism, coma etc.).

3.3.2.1 Quantitative HRTEM: Exit Plane Wave Reconstruction

In addition to aberrations, image interpretation and quantification also suffers from the fact that it contains spatial frequencies above the point resolution, for which the CTF values change with defocus and Cs [112,113]. However, a series of images, taken at a wide enough defocus range will provide interpretable information up to the information limit. The reconstructed wave function has higher contrast at low frequencies (relative to any single image). The acquired defocus series can be used to reconstruct both the amplitude and phase components of the exit wave function that can provide chemical and structural information, respectively [113].

Exit-wave reconstruction was performed on a series of 11 experimental micrographs, acquired at different objective lens defocus values (using Cs=-0.008mm). The series was reconstructed using TrueImage software (FEI). A simulated series of the interface was generated from an atomistic model (developed from the exit wave data) using EMS software [114]. This procedure was done for different specimen thicknesses and the resulting simulated series was also reconstructed using TrueImage for comparison with the experimental results. The resulting simulated wave components (amplitude and phase) were compared with the experimental ones to determine the atomic column positions.

3.3.3 Atom Probe Tomography

Atom probe microscopy is based on field evaporation of individual atoms which can be augmented by pulsed laser irradiation for non-conducting materials, from a needle shaped specimen, 10-100nm in radius. The evaporated atoms are chemically analyzed and identified by a mass spectrometer. The result is an atom-by-atom, high spatial resolution, and three dimensional chemical analysis of the specimen. Atom probe is a very useful tool for studying solute segregation since the data can be quantified directly without the need of correlating with other techniques.

The composition of the Ni surface was measured using atom probe tomography (APT, Imago, LEAP). Samples for APT were prepared using the dual-beam FIB at the Technion following the procedure described in section 3.4. Atom probe analysis was done at Oxford University, UK. Experimentally determined APT bulk detection limits for S, Al, Ar, Fe, Mo, Ca, Si and W ranged from 25-35 ppm.

3.3.4 ECS simulations

"Wulffman" freeware [115] was used to identify all the facets present on the Wulff shape of the Ni particles, using the surface anisotropy observed by SEM (FIB). The crystal equilibrium shape is approximated by a sphere cut by facets of given energy relative to the isotropic surface energy of the sphere. With this software we have identified the surface facets that are not included in the projection used for the specific TEM specimens, but are visible by SEM.

3.4 Specimen Thickness Measurement

Accurate thickness measurement of thin foils is an issue of increasing importance, especially with recent developments in quantitative electron microscopy. The specimen thickness of TEM samples needs to be determined not only for analytical microscopy, but also for quantitative HRTEM, beam broadening and spatial resolution determination in scanning transmission electron microscopy (STEM), x-ray absorption corrections, and

defect density measurements. In addition, knowledge of thickness variations is extremely important for improving specimen preparation techniques.

Several approaches were used in the past for thickness measurements of thin foils, for example indirect knowledge of the specimens' geometry [116,117,118]. However, these techniques are either limited to a specific type of material (e.g. amorphous spheres) or they provide the thickness only at a specific location in the specimen.

The use of electron energy loss spectroscopy (EELS) to measure TEM specimen thickness can provide a thickness measurement for a relatively large area, regardless of the crystallinity of the specimen. The fraction of inelastic scattering occurring as an electron beam penetrates a thin specimen depends on the density and thickness of the specimen (or, more correctly, the total path of the electrons through the specimen). This effect is quantified by the log-ratio equation [119]:

$$\frac{t}{\lambda} = \ln\left(\frac{I_T}{I_{ZLP}}\right) \qquad (9)$$

where I_T is the total integrated area under the EELS spectrum, I_{ZLP} is the area under the zero-loss peak and λ is the electron mean free path for inelastic scattering.

In order to obtain the absolute specimen thickness, the value of λ needs to be known. Egerton ***et al.*** and Malis ***et al.*** have proposed a method to ***calculate*** λ for a specimen of known composition [120,121]. In their work, they proposed a parameterized equation and compared the calculated values to measurements taken at an accelerating voltage of 120kV, with relatively small objective apertures (i.e. small scattering angles). The validity of Egerton and Malis's equation for higher voltages was never proven although it has been used in a large number of studies.

Since accurate specimen thickness measurement is important for this research, a great deal of effort was invested in developing an experimental method for preparing specimens with a known geometry, and their subsequent use to calibrate λ.

3.4.1 Preparation of Specimens with a Known Thickness

Needle-shaped specimens were prepared using the FIB in a similar manner to that often used to prepare specimens for atom-probe tomography [122]. In the initial stages of needle preparation an annular pattern was used, with a 30kV 93pA Ga ion beam. The inner diameter of the annular pattern was gradually reduced to 200nm. The final stage of preparation was performed by low voltage FIB polishing (2kV, 10pA) in order to reduce surface amorphization and Ga implantation [123]. In this final stage, a circular pattern was used to sharpen the specimens' tip. All of the crystalline specimens were prepared from single crystals with the axis of the specimen needles parallel to a low-index crystallographic plane for ease of interpretation and alignment of the needles in the TEM. As an example, SEM and TEM micrographs of a Ni needle (supported by sapphire) are presented in Figure 13.

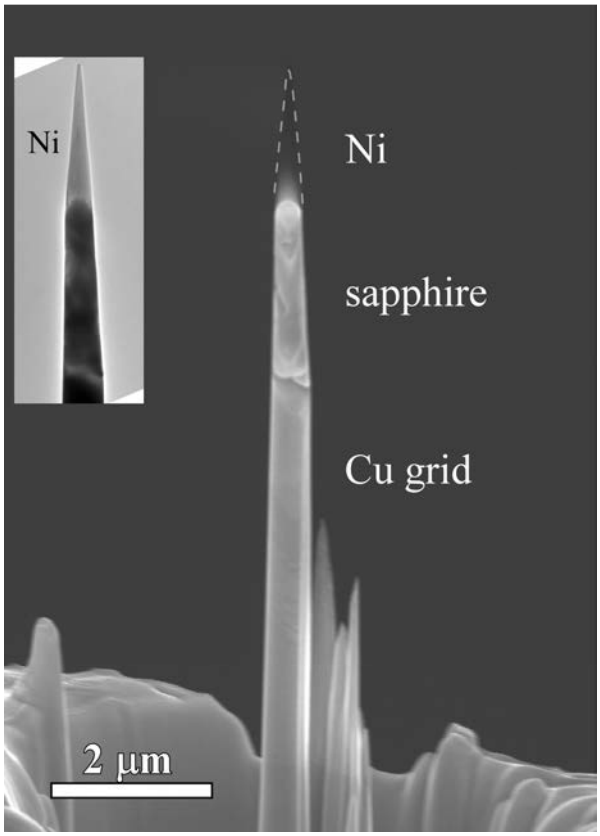

Figure 13: Secondary electron SEM micrograph of a Ni needle prepared by FIB. Due to the limited thickness of the needle tip, almost no secondary electron signal is detectable by SEM (image acquired at 10kV). The insert is a bright field TEM micrograph of the same needle, from which calibrated values of λ were obtained.

3.4.2 Thickness Measurement

EELS thickness maps were acquired in energy filtered TEM (EFTEM) mode by an automated procedure using Gatan's Digital Micrograph software. All thickness maps were acquired using a 6mm GIF entrance aperture, 0.7eV energy resolution, 10eV slit width and CCD binning of 4. Measurements were performed both in and out of low-index zone-axes. Relatively large objective apertures were used, resulting in a collection semi-angle β of 25.1mrad for Si, SiO_2 and Al_2O_3. For Ni a smaller aperture was selected to limit β to 17.7mrad. The collection angles were chosen to be relatively larger in order to keep the elastic-to inelastic scattering ratio independent of specimen orientation.

Since the specimen needles have a circular cross-section, by orienting the axis of the needle perpendicular to the incident electron beam, the width of the needle (w) at any point is equal to the maximum thickness (t) of the same cross section, as shown in the schematic drawing in Figure 14. In the coordinate system used here, the z-axis is that of the incident electron beam and the y-axis that of the specimen needle.

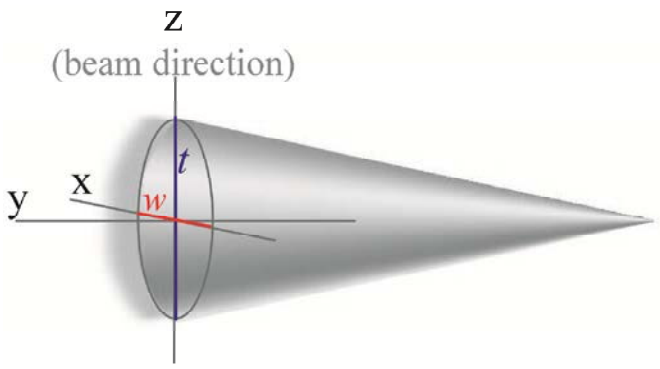

Figure 14: A schematic drawing of the specimen geometry used for calibration of the plasmon mean-free-path. For regions along the y-axis of the needle, values of t/λ were acquired using the EELS log-ratio method, and the value of λ was determined from the sample thickness (t) defined by the width (w) of the needle at that point on its axis.

Figure 15 is an example of thickness line-scans from a Si needle, acquired parallel to the x-axis of the sample. The thickness profiles were scaled to the radius of the needle, and then a mirror-image was created to confirm the circular cross-section. The line scans in this example were acquired parallel to the <110> zone axis (Figure 15, center) and from zone-axes at about ±25° tilt about the y-axis (Figure 15 left and right). All specimens were shown to have a circular cross section throughout the volume analyzed along the needle axis.

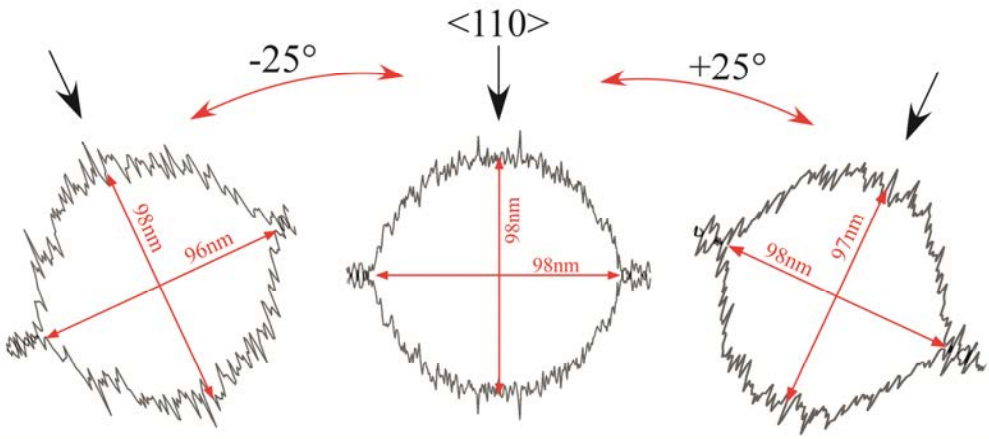

Figure 15 Thickness line-scans acquired along the x-axis of the Si sample. The profiles were scaled to the radius of the needle, and then a mirror-image was created to confirm the circular cross-section of the sample. The measurement was first performed on a [110] zone axis (center) and then at ±25° tilt about the y-axis (away from the low-index zone axis).

3.4.3 Ni Mean-Free-Path Calibration

The Ni needle was prepared from a dewetted Ni particle. Figure 16(a) is a bright-field TEM micrograph of the Ni needle. The width of the needle (and hence the maximum thickness of each cross-section) ranges from 40nm to 170nm along its length. The dashed line represents the location of the thickness line-scan that was used for the EELS analysis. The thickness map (shown in Figure 16 (b)) was acquired with a semi-collection angle of β=17.7mrad. The thickness gradient once more confirms that the needle has a circular cross-section throughout the analyzed region. This was further verified from thickness maps acquired after rotating the sample to large tilt angles about its y-axis.

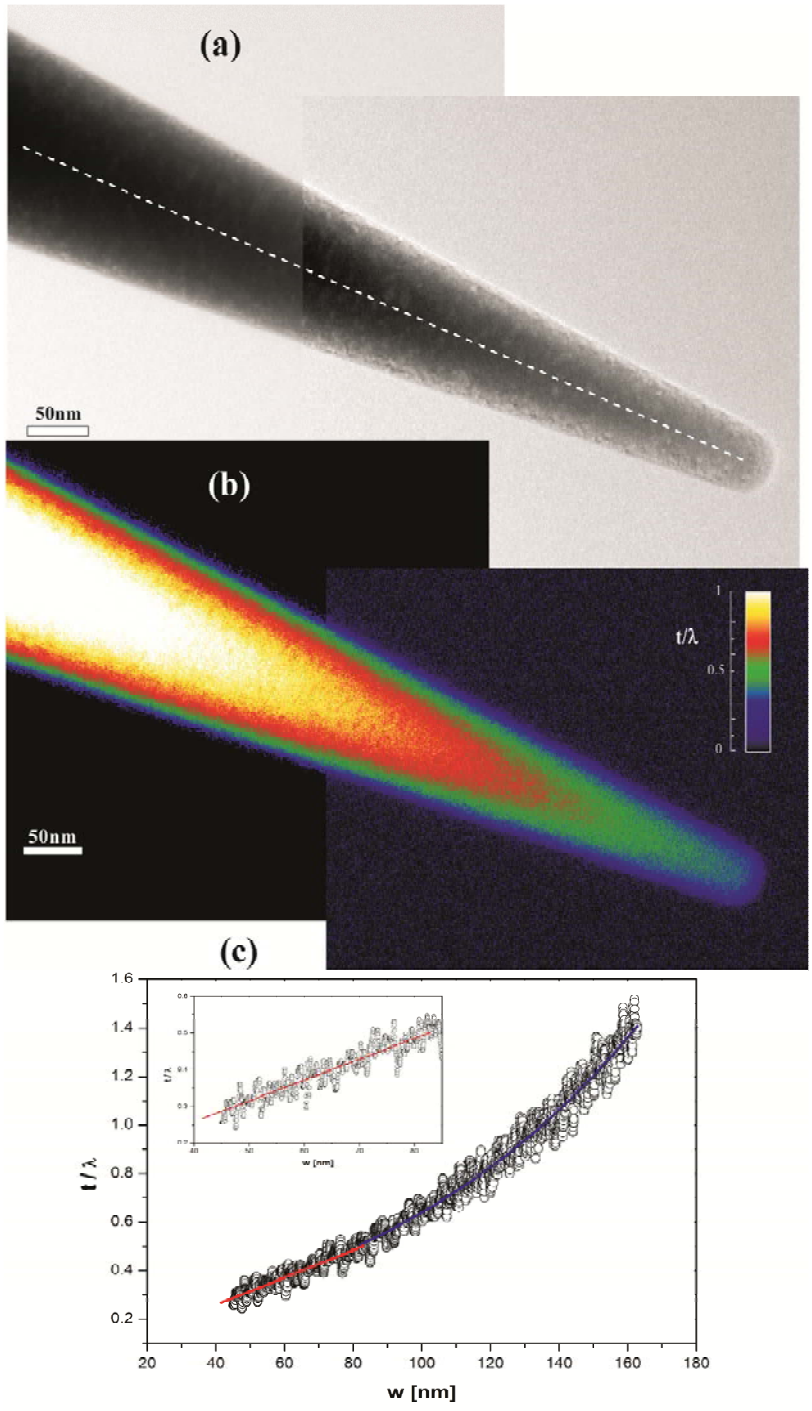

Figure 16: (a) Bright field TEM micrograph of the Ni specimen. (b) Thickness map acquired from the same region (β=17.7mrad, E0=300kV) using a false-color scale for the calibrated thickness. Each pixel on the map is correlated with a value of t/λ given by the legend. (c) Line-profile of t/λ as a function of specimen width w, acquired along the y-axis of the needle (indicated by a dashed line in

(a)). The data plotted in (c) show a linear change up to a value of t/λ=0.5 (plotted in red, and, at a higher magnification, in the inset). Above this value of t/λ an exponential behavior is observed (plotted in blue).

The thickness line-scan along the axis of the needle (the y-axis) was used to quantify λ from equation (9) (shown in Figure 16 (c)). The location of the line-scan is plotted as a dashed line in Figure 16 (a). A linear change in thickness along the axis is observed for $t/\lambda < 0.5$. This linear fit is marked with a red line (R=0.93). Since w=t, the slope of the line in the linear region is equal to 1/λ, and the ***measured*** value of the inelastic mean free path is: $\lambda_{Ni,\ 300kV,\ 17.7mrad} = 170nm$. For values of $t/\lambda > 0.5$, an exponential dependence was observed (plotted in blue, $R^2=0.97$). The accuracy of fit is limited to 0.1λ by the noise level of the thickness map and the surface roughness of the needle specimen. In the non-linear region, this error increases up to 0.2 λ, because a lower magnification was needed to image the larger needle cross-sections. The use of Egerton and Malis' equation for calculating λ for the same experimental conditions gives the value of $\lambda_{Ni,calculated}=96nm$. This major discrepancy of a deviation of 45% between the measured and calculated values is discussed in detail in the next section.

High resolution imaging of the Ni tip confirmed that no amorphous Ni remained on the specimen surface after low-voltage FIB polishing.

3.4.4 Calibrating Mean-Free-Path for Al_2O_3, Si and SiO_2

In a similar way to that described in the previous section, needle shaped specimens were prepared from Al_2O_3, Si and SiO_2. The results for the calculated are shown in Table 2. The calculated λ values are also presented for comparison.

Table 2: A comparison between the measured and calculated plasmon mean-free-paths.

	Measured λ [nm]	Calculated λ [nm]	Error
Ni	174	96	45%
Al_2O_3	143	126	12%
SiO_2	238	126	47%
Si	199	113	43%

The measured values of λ deviate significantly from the values calculated using Egertons' equation. Clearly, the influence of beam energy and collection angle is misrepresented in the equation, leading to a significant underestimation of the measured thickness.

The experimental method presented here can provide calibrated thickness changes over a large area of the specimen, and is not limited to a specific type of material or microstructure.

4. Results

4.1 Solid State Dewetting of Ni

The preferred orientation of the Ni particles on (0001) sapphire as determined from XRD was found to depend on the $P(O_2)$; a {100} preferred orientation was dominant in system A ($P(O_2)=10^{-9}$ atm) and a {111} orientation was dominant in systems B and C ($P(O_2)<10^{-20}$ atm). In both cases, the preferred orientation of the *as-deposited* film was {111}.

Previous knowledge regarding the substrate orientation combined with Ni surface facet identification allowed for the determination of the full orientation relationship of the particles from SEM micrographs. Among several hundred particles that were examined, only two orientation relationships (OR) were observed: 80% had the $\mathrm{Ni}(111)[1\bar{1}0] \| \mathrm{sapphire}(0001)[10\bar{1}0]$ OR (which is referred to as OR1), and the remaining 20% had the $\mathrm{Ni}(111)[1\bar{1}0] \| \mathrm{sapphire}(0001)[2\bar{1}\bar{1}0]$ OR (which is referred to as OR2). This was confirmed using electron diffraction in TEM. Note that the two ORs have the same interface plane but have a 30° relative rotation of the particle about the interface normal. In this study, only particles with OR1 were examined.

4.1.1 Solid-state dewetting kinetics

It is clear from Figure 9 that most of the particles have not equilibrated under the experimental conditions used in this study. At the final stage of the experiment, the particles are all single-crystals with a {111} plane parallel to the sapphire substrate. Although all of the facets that were identified in the ECS also appear in the large non-equilibrated particles, the particle aspect ratio is very large (they all have a height of 1-1.5 μm regardless of the lateral dimensions). The particles that are less than 2μm in diameter seem to have equilibrated completely in the directions parallel to the substrate, while the top facet is larger than the equilibrium size. In Figure 17, three equi-axed particles are visible, with different diameters ranging from 1.02 μm to 1.45 μm. The size of the side

{111} facets is marked by dashed lines to demonstrate that the top {111} facet is larger, and hence not equilibrated for the particles shown in the center and bottom of Figure 17. However, the ratio of sizes measured for the side {111} facets and the particle diameter is almost identical for all three particles, equal to 0.27, indicating that the side facets had indeed reached a steady state which may be equilibrium.

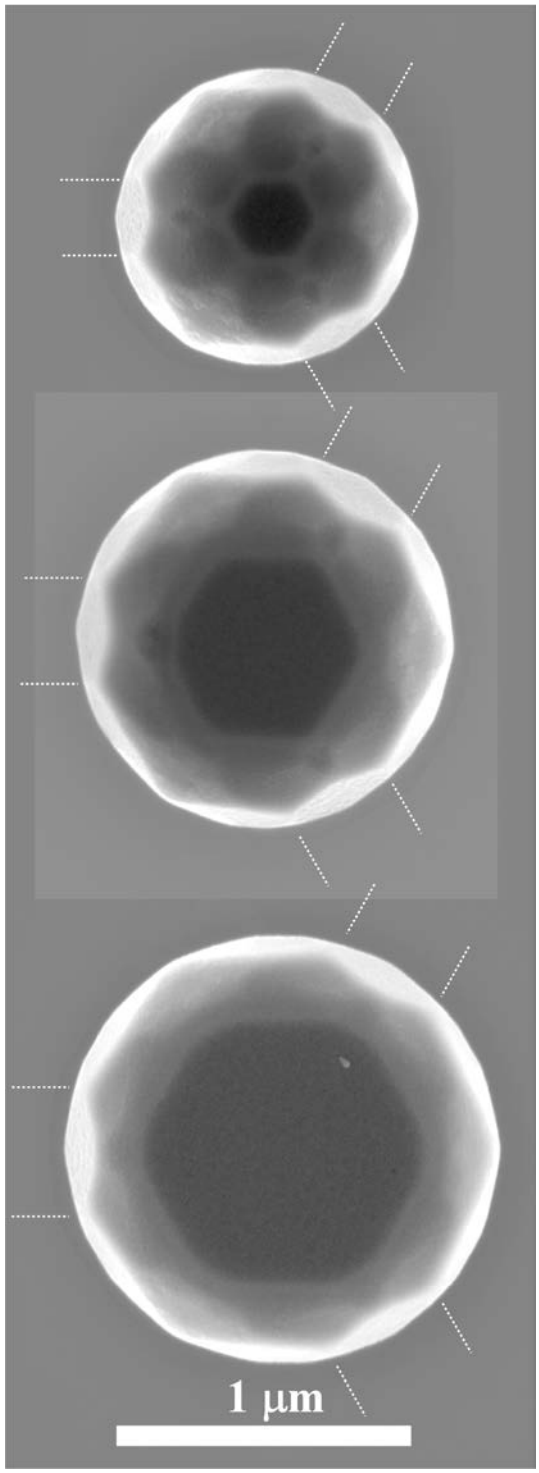

Figure 17: SEM micrographs of three particles of different diameters in system C showing different stages of equilibration. The dotted lines mark the size of the {111} facets on the sides, for comparison with the top {111} facet. Only the top particle reached equilibrium. All three particles exhibit the same facets but different relative size of the top {111} facet.

4.2 Equilibrium Crystal Shape of Nickel

4.2.1 Ni Crystal Shape

Figure 18 presents a HRSEM micrograph of one of the Ni particles equilibrated in Ar (system A, $P(O_2)=1*10^{-9}$ atm). This particle (with a (100) orientation parallel to the substrate surface) has a highly faceted shape. Four different families of facets are visible in the plan-view image, which have sharp connections to the rounded surfaces.

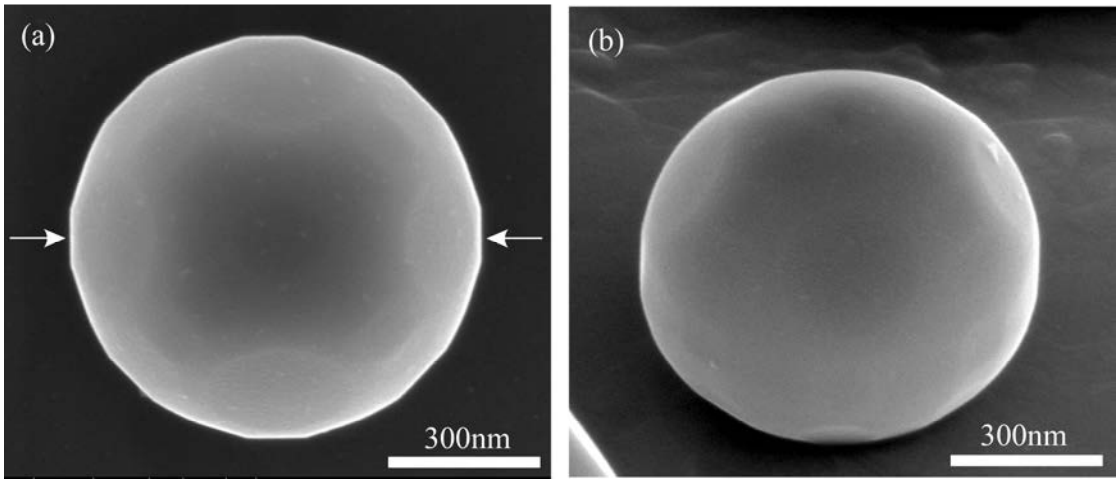

Figure 18: Secondary electron HRSEM micrographs of a Ni particle (system A, P(O2)=1*10-9 atm). The single crystal particle is oriented with the (100) plane parallel to the substrate. (a) plan-view. (b) side-view (52° tilt). The arrows indicate the location and direction of sectioning.

Figure 19 presents two HRSEM micrographs of a Ni particle equilibrated in $Ar+H_2$ (system B, $P(O_2)<10^{-20}$ atm). The particle is oriented with the (111) plane parallel to the substrate surface, and appears less faceted than the (100) oriented particle shown in Figure 18. However, this information cannot be used to draw any conclusions regarding the anisotropy of the surface energy for two reasons. First, the (111) oriented particle is coated with a thicker carbon layer that covers the morphological details on the surface, such as smaller facets. Second, the size of the (111) oriented particle is less than half that of the (100) oriented particle, so even if the facets were exposed, they might be too small to be detected (not resolved) by SEM. In addition, it is also possible that the connection of the facets to the rounded surface is smooth and not sharp as in system A. Such a

gradual change in surface orientation (and thus contrast) makes facets much more difficult to detect.

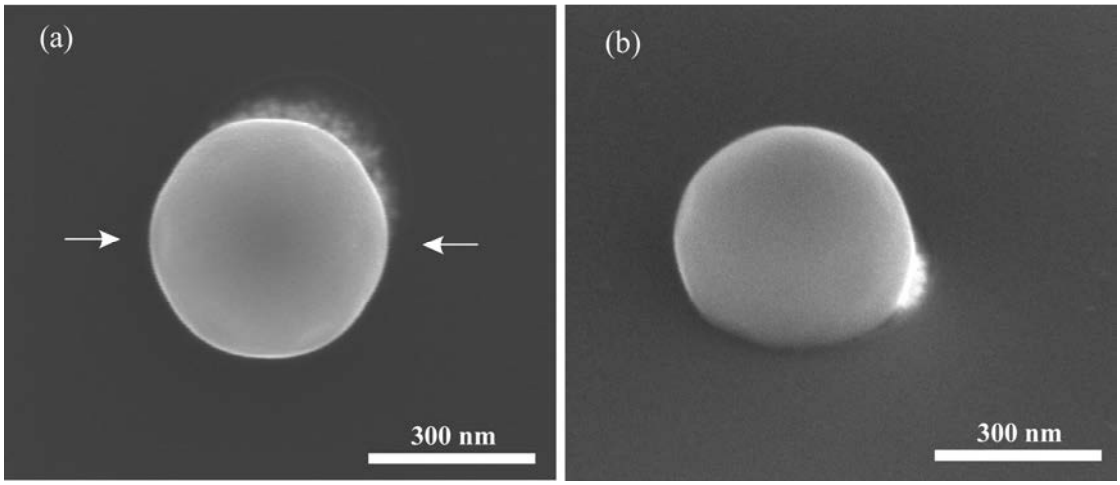

Figure 19: Secondary electron HRSEM micrographs of a Ni particle in system B ($P(O_2)=10^{-20}$ atm). The single crystal particle is oriented with the (111) plane parallel to the substrate surface. (a) plan-view (b) side-view (52° tilt). The arrows indicate the location and direction of sectioning. The bright contrast in (b) is due to electron charging of uncoated sapphire.

Due to the concern that the lack of facets in the particle seen in Figure 19 may be due to impurities in the starting materials or contamination in the furnace system, a dedicated dewetting furnace was constructed, in which the specimen is held in a sapphire tube (3.1.1.2). Figure 20 presents HRSEM micrographs of a Ni particle equilibrated in Ar+H_2 (system C, $P(O_2)<10^{-20}$ atm) in the sapphire tube furnace. In addition, the Ni target used for the deposition was 99.9995% pure (rather than 99.99% as in systems A and B). The particle is oriented with the (111) plane parallel to the substrate surface, and appears to be completely faceted.

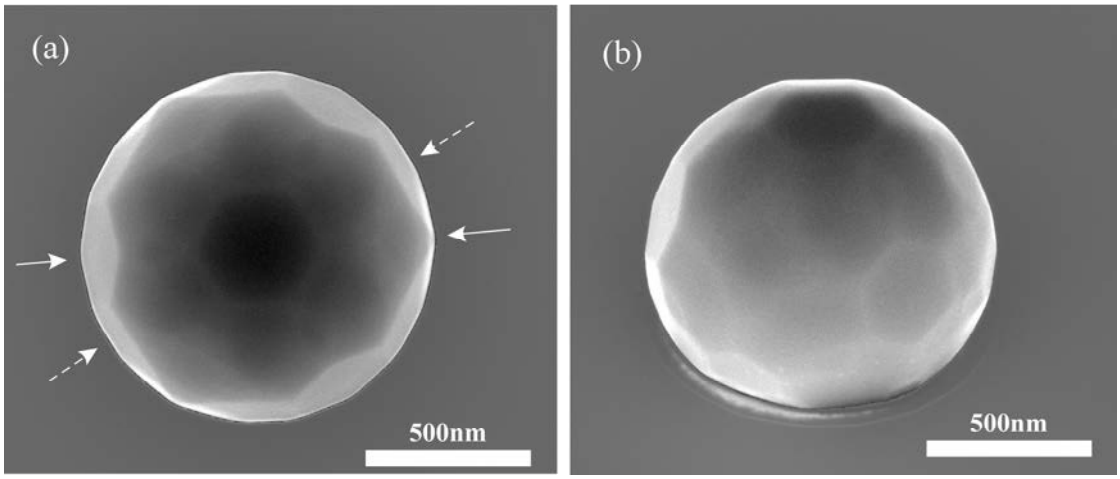

Figure 20: Secondary electron HRSEM micrographs of a Ni particle from system C ($P(O_2)=10^{-20}$ atm). The single-crystal particle is oriented with the (111) plane parallel to the substrate surface. (a) plan-view (b) side-view (52° tilt). The arrows indicate the locations and directions of sectioning.

Unlike SEM, by which over 50 particles were found to have identical crystal shapes for the three annealing processes, cross-section imaging of the particles in the TEM allows improved resolution and facet identification by electron diffraction. However, specimen preparation requires extreme precision (about 20 nm tolerance in the location of the thinnest area) and provides only limited sampling (due to the time required for specimen preparation) of a single projection of the shape to be analyzed. In this work, three TEM specimens were characterized for system A, two for system B and 5 for system C. Figure 21, Figure 22 and Figure 23 present bright field TEM micrographs of the equilibrated Ni particles. The specimens were prepared from the center of the same particles shown in Figure 18, Figure 19 and Figure 20 respectively, along the directions marked on the plan-view SEM micrographs.

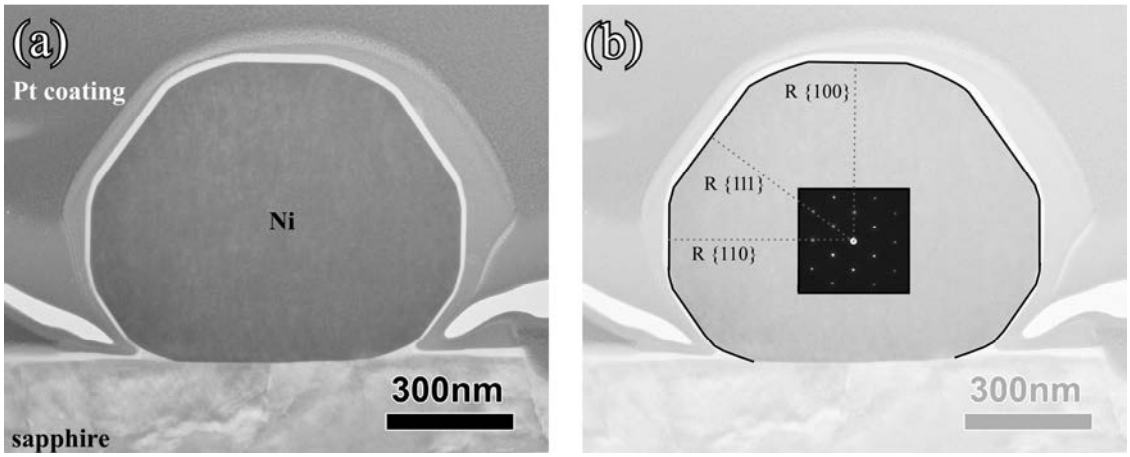

Figure 21: (a) bright field TEM micrograph of the (100) oriented Ni particle in system A along the [101] projection. (b) The Wulff shape contour (bold line), selected area electron diffraction pattern (inset in the center) and distances from the Wulff point to the {hkl} facets (dotted lines, marked as R{hkl}).

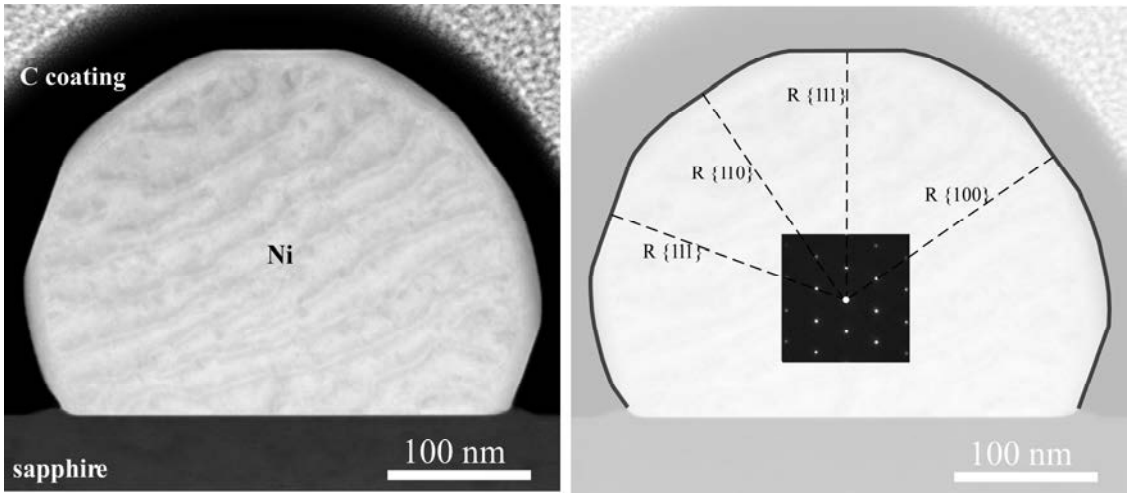

Figure 22: (a) High angle annular dark field STEM micrographs of the (111) oriented Ni particle equilibrated in system B, along the [101] projection. (b) The Wulff shape contour (bold line), selected area electron diffraction pattern (inset in the center) and distances from the Wulff point to the {hkl} facets (dotted lines, marked as R{hkl}).

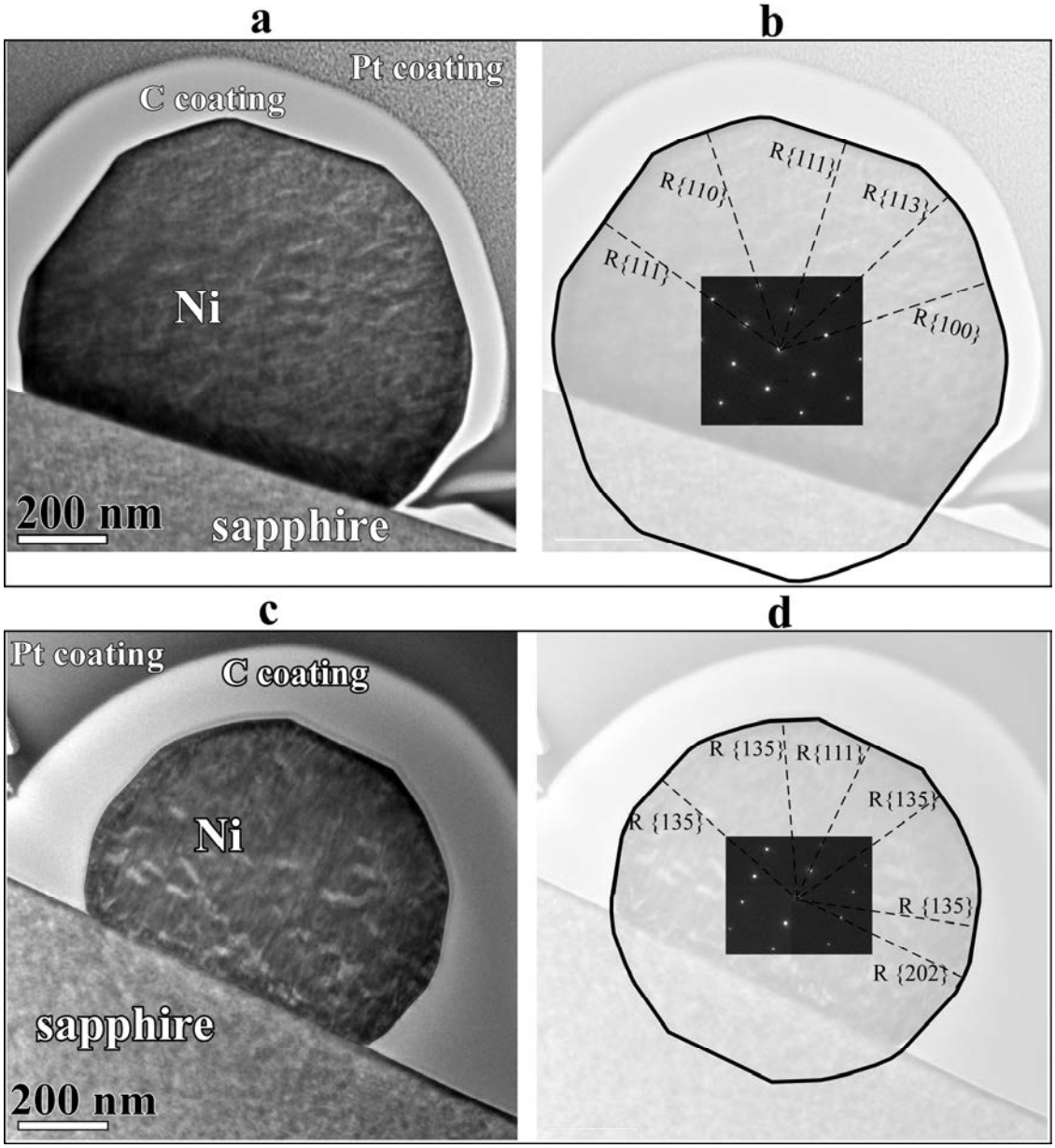

Figure 23: (a,c) bright field TEM micrographs of the (111) oriented Ni particle equilibrated in system C, along the [101] and [121] projections. (b,d) The Wulff shape contour (bold line), selected area electron diffraction patterns (inset in the center) and distances from the Wulff point to the {hkl} facets (dashed lines, marked as R{hkl}).

TEM analysis revealed that in the three systems, {111}, {110} and {100} surface facets were stable. It should be noted that the existence of other facets cannot be ruled out since

only one or two projections were examined for each system. In all cases, the lowest energy surface facets included *both* {111} and {100}. Most facets have sharp edges which mean that some orientations are missing on the ECS. An exception is the {110} facet on the particle equilibrated in system B (Figure 19). As observed from the SEM micrographs, this system also has the least anisotropic surface energy.

The use of a furnace with a sapphire tube and a purer Ni film (system C), stabilizes additional {113} and {135} surface facets that did not appear in the other two systems. The anisotropy for the examined particles as measured by TEM is given in Table 3.

4.2.1.1 ECS Simulations

"Wulffman" freeware was used to identify all the facets present on the Wulff shape of the Ni particles, using the surface anisotropy observed by SEM (Table 3). The crystal equilibrium shape is approximated by a sphere cut by facets of given energy relative to the isotropic surface energy of the sphere. With this software we have identified the surface facets that are not included in the projection used for the specific TEM specimens, but are visible by SEM (see Figure 24).

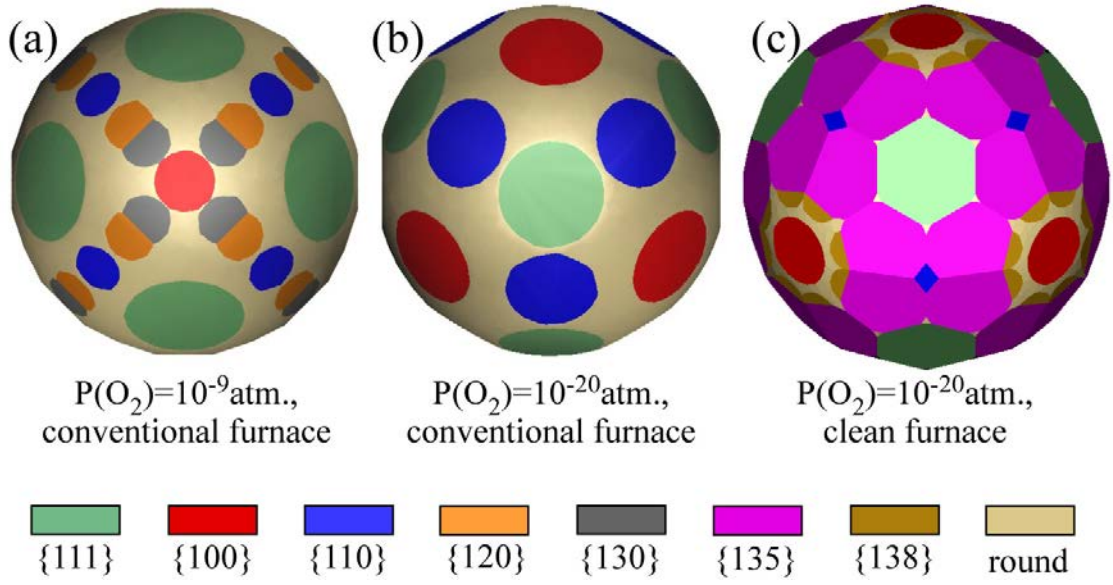

Figure 24: "Wulffman" simulations from SEM micrographs of the ECS of particles from systems A, B and C.

The Wulffman construction proved to be useful for system A, where two additional surface facets were identified: (012) and (013). Moreover, in system C the simulation proved that the {135} facets are in fact included in the Wulff shape, and determined the presence of yet another vicinal surface, {138}, in the ECS. The {113} facet that was identified by TEM is not present in the simulated ECS. This is because the surface plane that was thought to be (113) is not positioned edge-on in the TEM.

Table 3: Ni surface energy anisotropy as measured by TEM or from "Wulffman" simulations.

System	$P(O_2)$	Relative surface energies, $\gamma_{(hkl)}/\gamma_{(111)}$ as measured by TEM (**red**) or by Wulffman (**blue**)						
		$\gamma_{(001)}$	$\gamma_{(011)}$	$\gamma_{(012)}$	$\gamma_{(013)}$	$\gamma_{(135)}$	$\gamma_{(138)}$	$\gamma_{(max)}$
A	10^{-9} atm	**1**	**1.05**					**1.07**
		1.05	**1.05**	**1.05**	**1.05**			**1.06**
B	10^{-20} atm	**1**	**1.01**					**1.05**
		1	**1.01**					**1.05**
C	10^{-20} atm	**1**	**1.06**			**1.04**		**1.08**
		1.02	**1.03**			**1.01**	**1.03**	**1.04**

4.2.1.2 Surface Chemistry

APT was performed on the surface of particles with similar orientations to the ones analyzed by TEM. Line-scans are given for systems A, B (Figure 25 and Figure 26, respectively) and a 3D reconstructed tomogram is given for system C (Figure 27). Unlike in the case of liquid Ni equilibrated on sapphire [47], no Al was detected in the bulk Ni or at the surface (detection limit of 0.001 atoms/nm^2 which is roughly equivalent to 0.0001 monolayers).

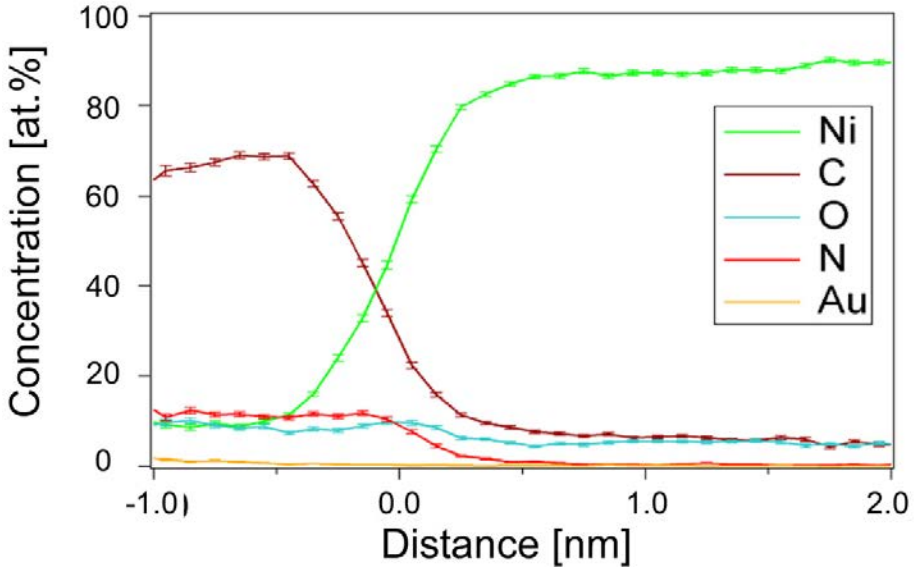

Figure 25: Line-scan from the APT data perpendicular to the Ni surface from system A.

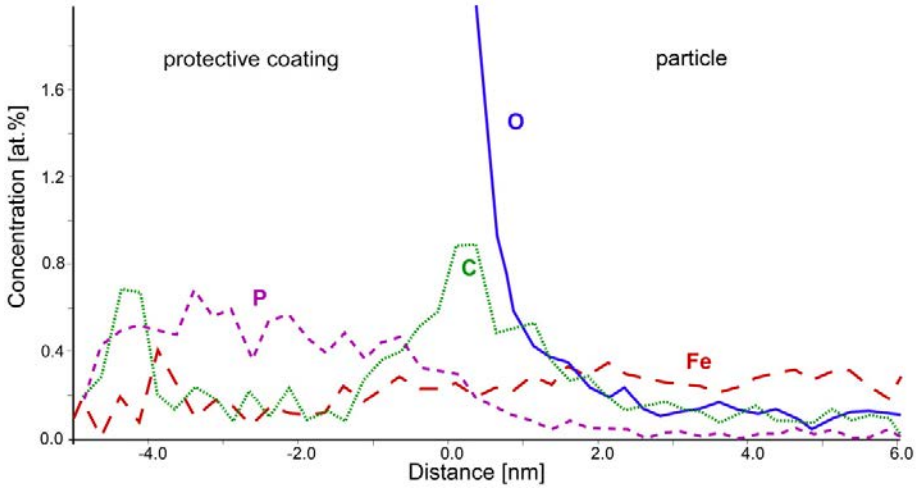

Figure 26: Line-scan from the APT data perpendicular to the Ni surface from system B.

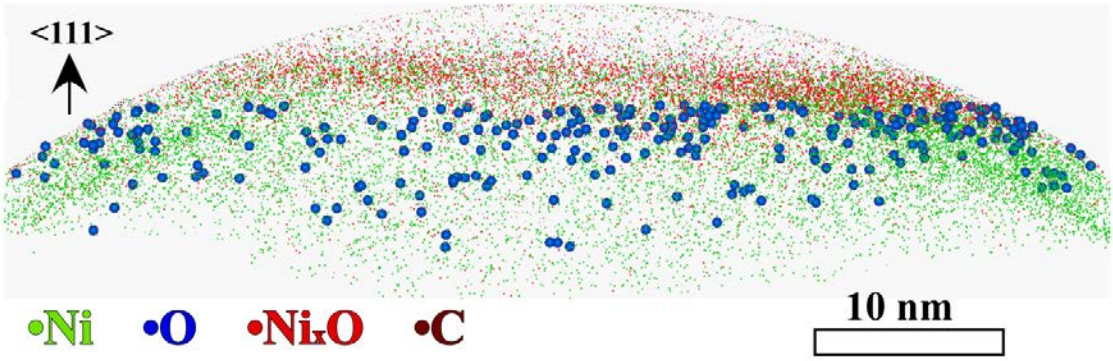

Figure 27: Reconstructed atom probe tomogram of the top of a (111) Ni particle from system C. Only three elements were detected: Ni, O and C. The large blue circles represent oxygen adsorbed from the ambient on the surface of the atom probe tip (after sample preparation).

For all three systems, a few nanometers (thickness) of oxidized Ni was found at the surface. This is expected since the measurements were conducted an extended period of time after the samples were prepared using the FIB, which included transfer from the dewetting furnaces to the FIB, and to the APT system, during which surface oxidation could not be prevented. This issue is somewhat problematic and means that the measurement of oxygen at the surface is not possible. However, a major difference was measured in the bulk oxygen content for all 3 systems: 0.2 at% in system B, and less than 0.02at% in system C. (The APT samples from system A were exposed to the ambient, as needles, for an extended duration and most of the metal was oxidized. Thus, the oxygen content in the Ni could not be determined for system A.) In system B, the surface Fe concentration was similar to that of the bulk (0.3-0.4at%). It can be seen from Figure 27 that in system C no element was detected other than Ni, O and C. Since the specimen was coated with a conductive carbon layer, no conclusions can be deduced regarding carbon surface adsorption.

4.3 Ni-Al_2O_3 Interfaces

4.3.1 Ni-Al_2O_3 Interface Energy

In order to quantify the thermodynamic stability of the interface, the interfacial energy was measured from cross-sections of the particles viewed in the TEM, using Winterbottom analysis (8). An example of one cross-section including the relevant parameters for Winterbottom analysis is presented in Figure 28. For the analysis, the surface energy of sapphire was taken from the literature $\gamma_{sapphire(0001)}$=1.07 J/m^2 [41] and the surface energy of Ni was calculated from the liquid Ni surface energy, taking into account the surface anisotropy of solid Ni and was determined to be $\gamma_{Ni(111)}$=2.05 J/m^2 (see Appendix III). It was found that the Ni(111)-Al_2O_3(0001) interface energy equilibrated at a P(O_2)=10^{-20}atm and 1623K is 2.16±0.2 J/m^2.

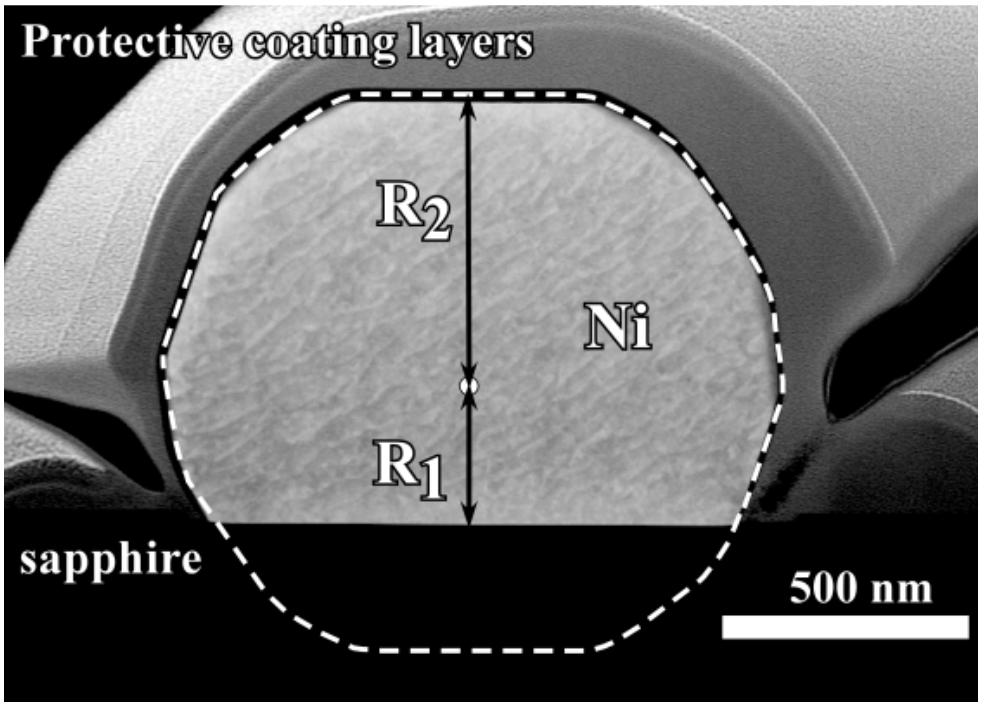

Figure 28: High angle annular dark field STEM micrograph of an equilibrated Ni particle, viewed along the [110] zone axis. The parameters R_1 and R_2 that are used for the energy measurement are indicated (see equation (8).

4.3.2 Ni–Al_2O_3 Interface Structure

In order to examine the interface structure, cross-section TEM samples were extracted from several particles, identical in shape and orientation relationship (all having OR1). For full analysis the interface was characterized in two different low index zone axes: projection A: $\mathrm{Ni}\left[1\bar{1}0\right]\|\,\mathrm{sapphire}\left[10\bar{1}0\right]$ and projection B: $\mathrm{Ni}\left[1\bar{2}1\right]\|\,\mathrm{sapphire}\left[11\bar{2}0\right]$. It should be noted that these are two complementary viewing directions for the same interface having OR1.

From each projection, a defocus series was acquired and the electron exit wave was reconstructed. The reconstructed wave amplitudes of both projections are presented in Figure 29. EMS software was used to simulate the exit wave of both the Ni and sapphire for different specimen thicknesses for both projections. The best fit was found for a thickness of 20-25nm for projection A and a thickness of 15nm for projection B. Note that the simulated amplitude does not contain all of the aberrations as the experimental micrograph, which results in a small discrepancy (visible mainly in the sapphire). EELS thickness maps were also used to experimentally determine the thickness of the examined areas of the specimens using a fully calibrated plasmon mean-free-path (see section 3.4) [124]. The thickness determined from EELS matched within 10% that found from exit wave simulations.

From this data, the atomic columns positions were determined, and the sapphire termination was identified to be the Al-1 termination (see Figure 33). In addition, interface relaxation was observed resulting in a 6.0-6.6% reduction in d-spacing of the Ni (111) terminating layer. In one of the specimens (viewed along projection A), a stacking fault was identified between the 2nd and 3rd Ni layers from the interface. However, this stacking fault is probably not an intrinsic part of the equilibrated interface since it was not observed in other TEM specimens prepared along projection A. (In projection B, i.e. Ni [121], such a fault cannot be detected.)

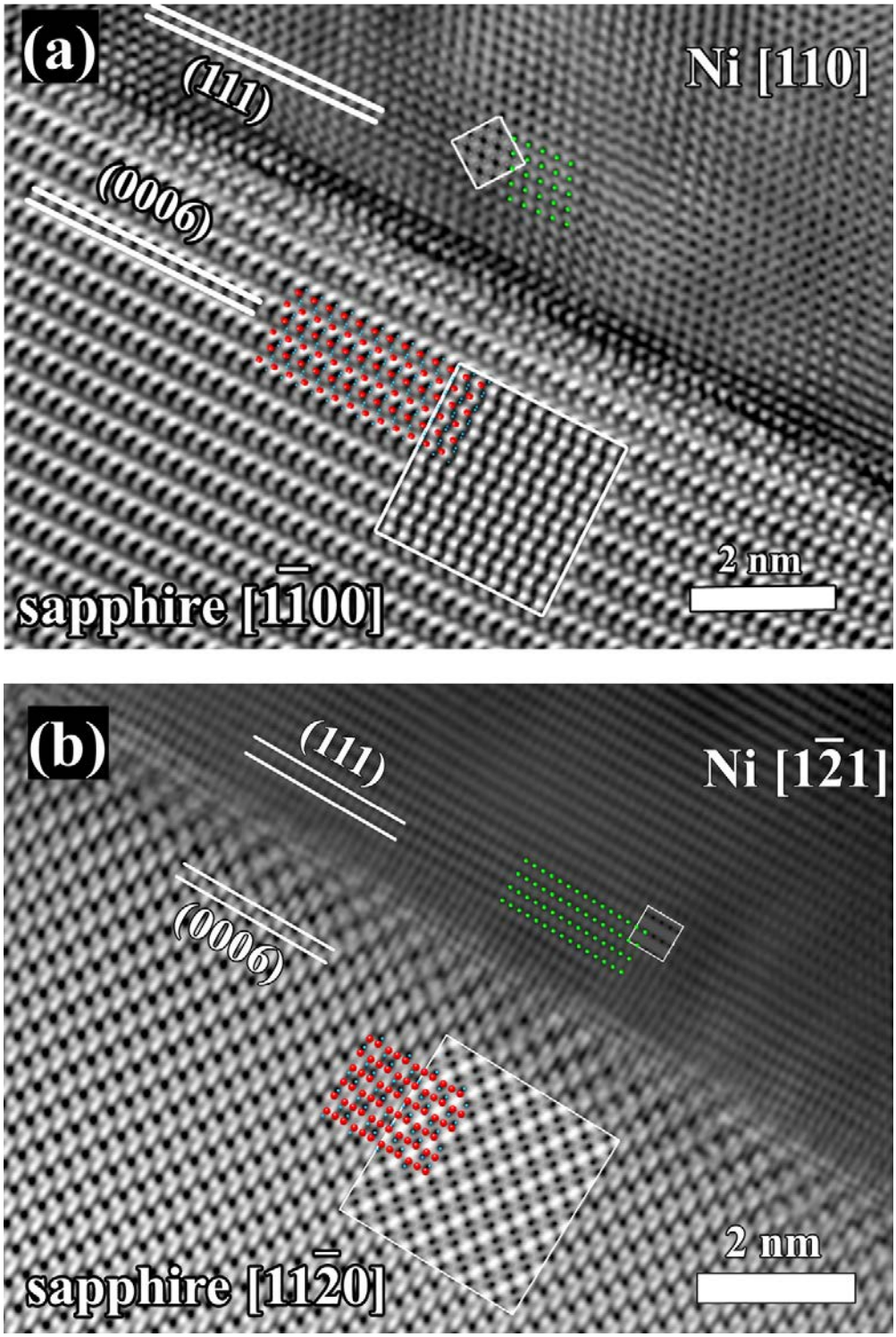

Figure 29: Reconstructed exit wave amplitudes of (a) projection A and (b) projection B. The simulated wave amplitude of both the Ni and sapphire is inset in both projections. The atomic column positions are overlaid in color: oxygen-red, aluminum-blue, nickel-green.

The examined specimens were also used for interface dislocations analysis using several TEM techniques. No dislocations were found at any of the examined interfaces and so it was concluded that the interface is incoherent at equilibrium. Although no reaction layer was found at the interface, a unique periodic contrast was observed in all of the specimens viewed along projection A (see Figure 29a and Figure 30). In order to enhance this periodicity, Figure 30 (a) was stretched normal to the interface. The measured wave length and amplitude of the periodic contrast running parallel to the interface are 23.6Å and 0.77Å, respectively. From image simulations it was concluded that this contrast originates from the terminating Ni layer that deforms periodically and undergoes reconstruction (i.e. a change in symmetry of the layer).

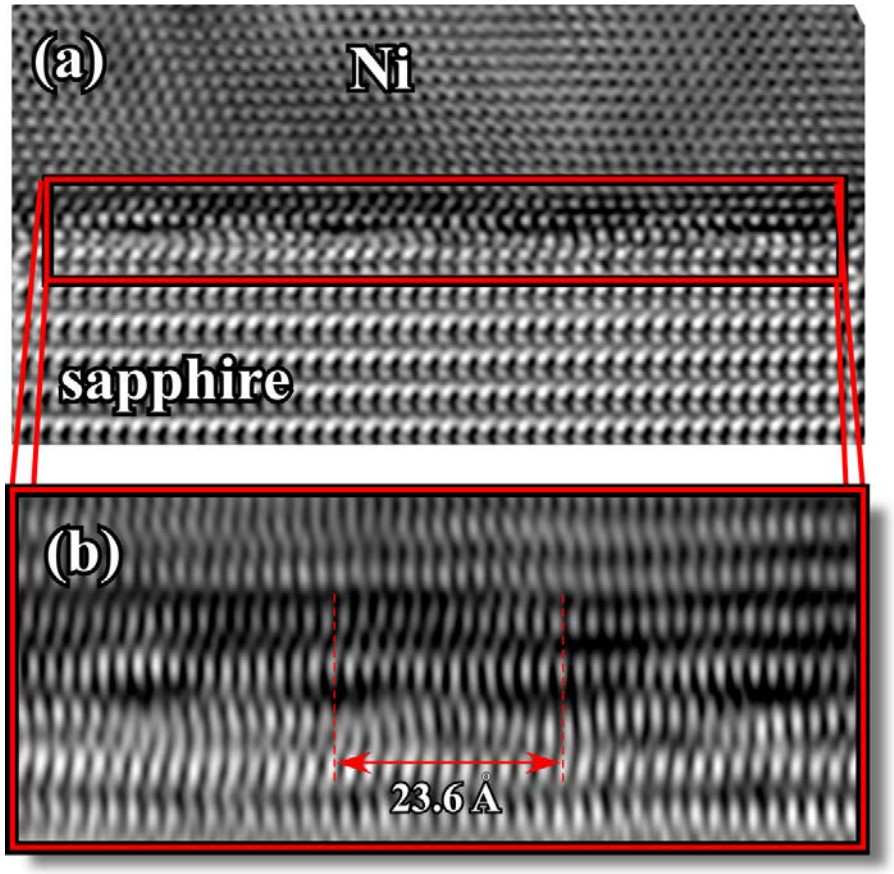

Figure 30: (a) The exit wave amplitude of the interface viewed along projection A. (b) a magnified image of the interface region showing the reconstructed Ni layer. In order to enhance the periodic contrast for viewing purposes, the image was stretched perpendicular to the interface.

To understand the structure of this reconstructed layer, atomistic models of the terminating layers were used, combined with the data obtained from HRTEM imaging. Figure 31(a) shows the atomistic model of only the terminating layers. The Ni atoms (shown in green) coincide with the oxygen atoms (marked in red) in a periodic manner across the interface region. The areas of largest coincidence are marked by hexagons. In these areas, the Ni shifts towards the oxygen atoms in order to form shortened Ni-O bonds. This shift is less pronounced farther away from the areas of coincidence. Between the areas of coincidence the Ni atoms shifts laterally (parallel to the interface) in order to shorten the Ni-O bonds, in addition to a vertical shift (which is smaller than that seen in the coincidence areas). This periodic reconstruction forms a two-dimensional interfacial unit cell, with a lattice parameter of 27.25Å (marked in black in Figure 31(b)).

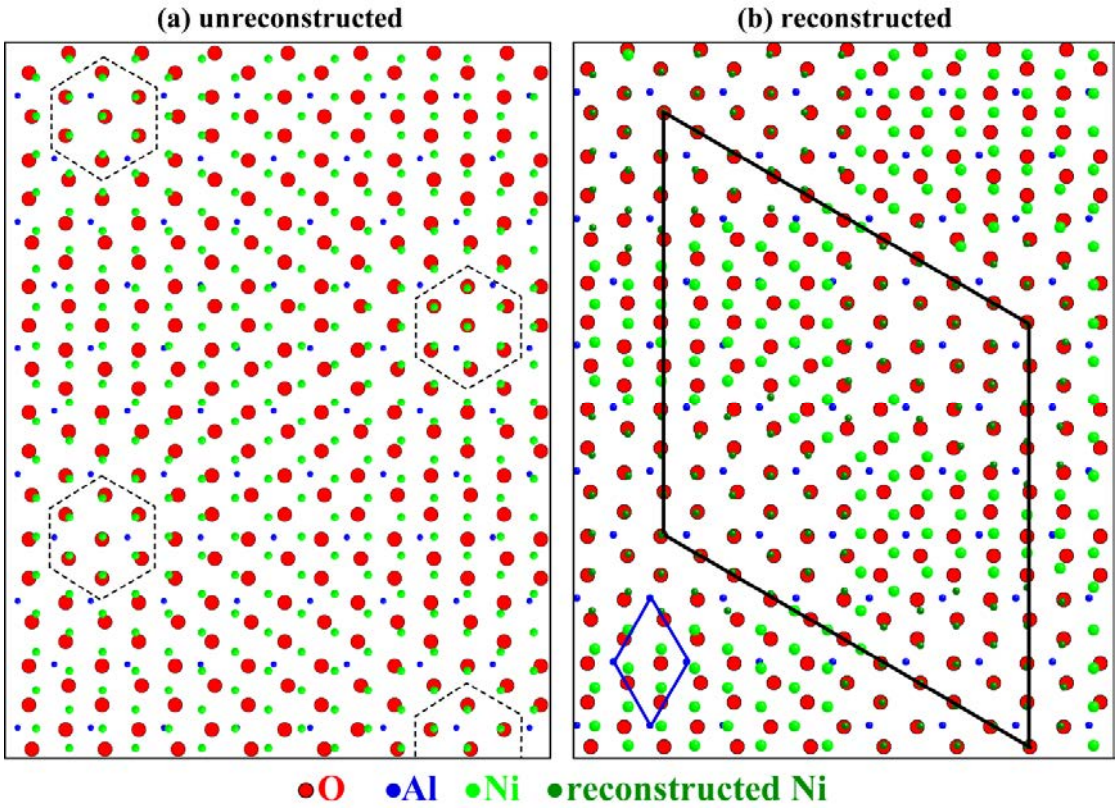

Figure 31: Schematic drawing of the terminating layers at the (a) unreconstructed and (b) reconstructed Ni-Al_2O_3 interface (determined from exit wave reconstruction). The areas of coincidence of the Ni atoms with the underlying oxygen are marked by hexagons in (a). These are the areas of the largest shift of the Ni atoms towards the sapphire. The reconstructed layer forms a

hexagonal 2-D unit cell, marked in black in (b). The Ni atoms that changed their positioned are marked in dark green.

This hexagonal 2-D unit cell is positioned parallel to the $<10\bar{1}0>$ directions of the sapphire. For this reason, the periodicity along these directions (i.e. projection A) is more pronounced and the projected wave-length is $27.25 \times \cos(30) = 23.6\text{Å}$ (see the dashed lines in Figure 32). This spacing fits perfectly to the periodic contrast that was measured experimentally (see Figure 30).

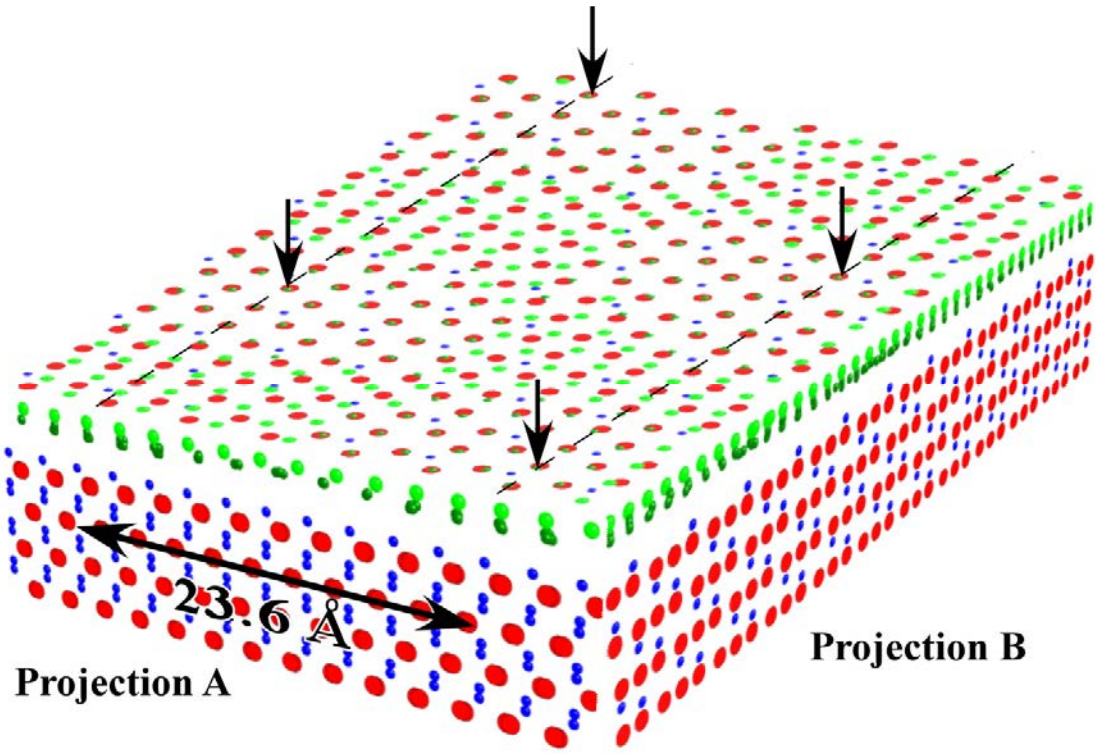

Figure 32: A projected schematic drawing of the reconstructed interface, showing both projections A and B. The positions of coincidence (marked by arrows) have a spacing of 23.6Å in the A ($\left[10\bar{1}0\right]$) direction.

Figure 33 presents the reconstructed electron wave amplitudes of the interface along projection A and B, with the atomistic model (shown in Figure 31(b)) superimposed.

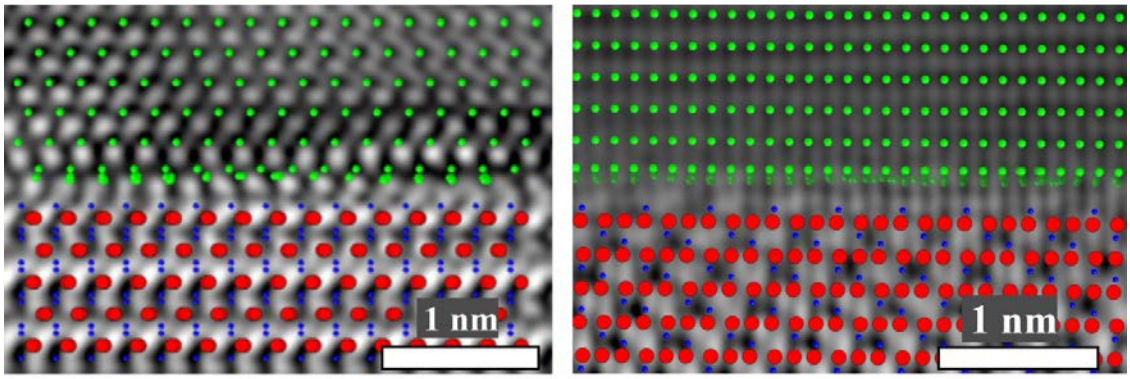

Figure 33: Reconstructed electron wave amplitudes of the interface along (a) projection A and (b) projection B (a magnification of Figure 29). The atomistic model is superimposed: Al in blue, O in red and Ni in green.

4.3.3 Ni(Hf)–sapphire interface

Following the characterization of the pure Ni-Al_2O_3 interface, the aim of this section is to study the influence of impurity segregation on the structural and thermodynamic properties and compare them to that of the undoped interface. Hf was chosen as dopant due to its technological importance in commercial Ni-Al_2O_3 interfaces.

In order to create a solid solution of Hf in Ni, it was necessary to keep the Hf content below the solubility limit (~0.5at.% at 1623K[125]). Approximately one monolayer of Hf was deposited between two ~125nm thick Ni layers (without breaking vacuum in the deposition system), to give ~0.5at.%Hf in the Ni films. Hf was found in the form of HfO_2 precipitates only on the free surface of the sapphire (marked by the arrows in Figure 34). In order to measure the Hf concentration at the interface or on the free surface of Ni, several analytical methods were used, including energy dispersive spectroscopy (EDS) in TEM, wavelength dispersive spectroscopy (WDS) from thin SEM specimens, EELS and high resolution Z-contrast STEM. It was concluded that no Hf was present at the interface or on the surface of the Ni (lowest detection limit=1monolayer, 7 particles examined). Surprisingly, Hf was also not detected in the bulk Ni (measured by WDS, detection limit=50ppm) although according to the phase diagram, the solubility limit of Hf in Ni at 1623K is 0.5at.% [125].

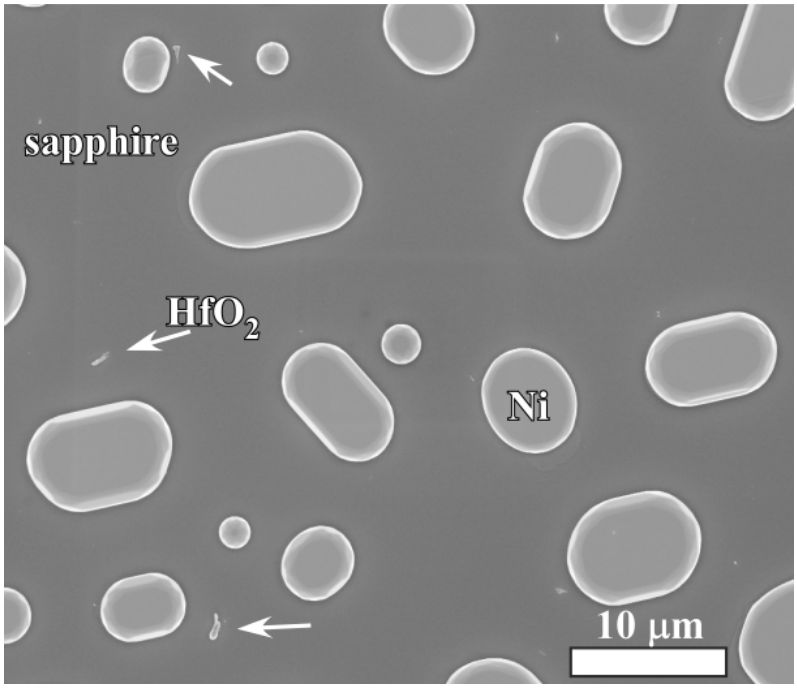

Figure 34: SEM micrograph of Ni+0.5at.%Hf dewetted on a sapphire substrate. Small HfO_2 precipitates were found on the sapphire surface (indicated by the white arrows). Hf was not detected at the Ni-Al_2O_3 interface, at the surface of the Ni or in the Ni bulk.

Two possible explanations were proposed for the absence of Hf from the interface. One is that the Hf does not decrease the interface energy, and segregation is promoted to the free surface of the sapphire, and the other explanation is that the amount of Hf was insufficient since the presence of HfO_2 particles depleted the Hf in the Ni (and thus at the interface). In order to eliminate the latter, another Ni-Hf multilayer specimen was prepared, containing 5at.%Hf. The total thickness of the layers was larger than that used in the previous samples (~350nm), resulting in a partially dewetted Ni film and areas of exposed sapphire (see Figure 35 (a-d)). Hf was found mostly on the free surface of the sapphire in the form of HfO_2 elongated precipitates stretching from the center of the exposed sapphire toward the Ni islands. The holes in the Ni film apparently nucleate on (more equiaxed) HfO_2 particles, which can be seen in the center of all of the areas of exposed sapphire.

HfO_2 was also found on the surface of the partially dewetted Ni (see Figure 35(b)).

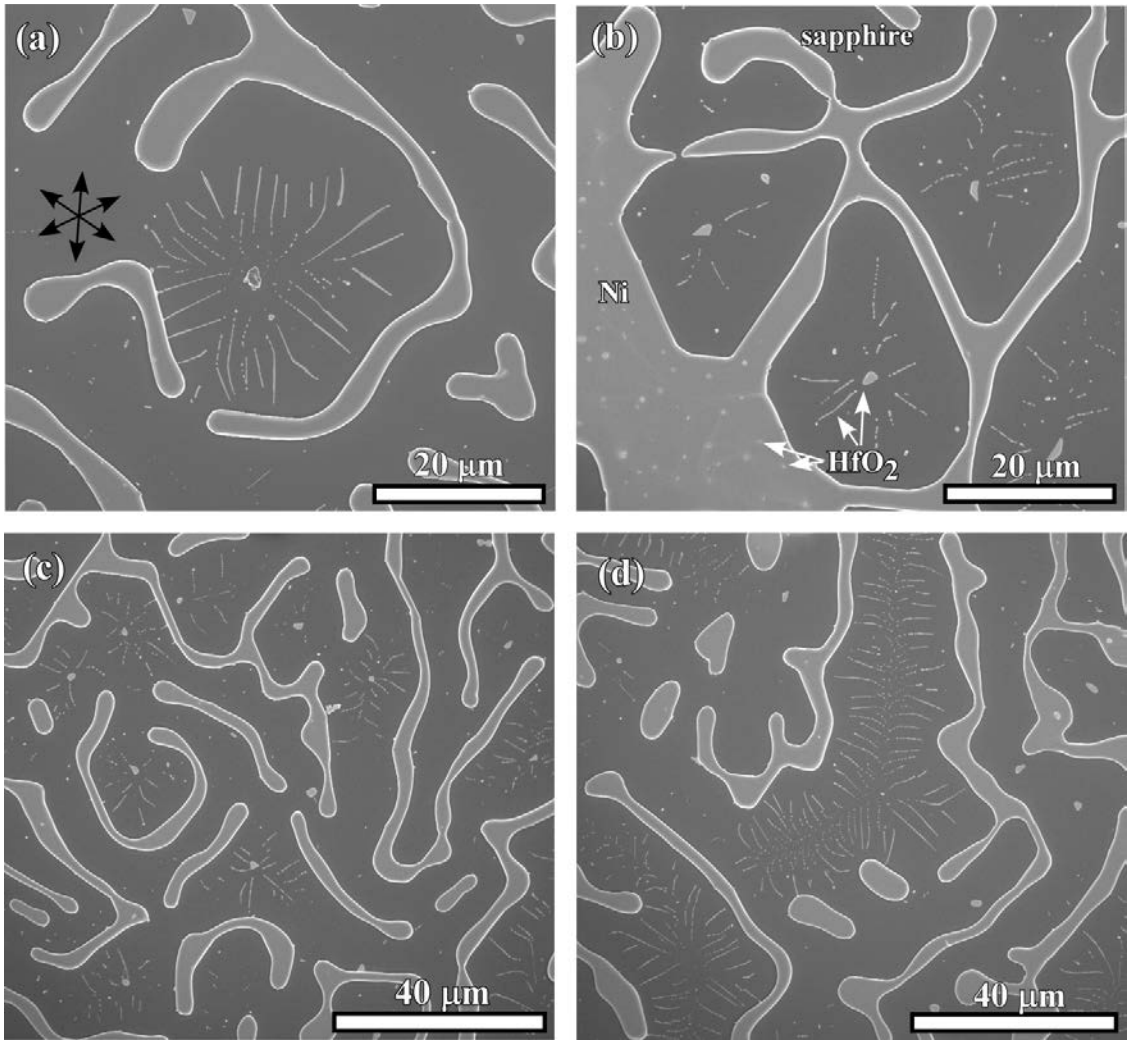

Figure 35: SEM micrographs of Ni+5at.%Hf partially dewetted on sapphire. Hf was found only in the form of (oxidized) stripes or particles. Hf segregates to the triple junction at a similar rate that the Ni dewets away from the Hf islands. As a result, Hf stripes depict the dewetting path. The arrows in (a) mark the $\langle 1\bar{1}00 \rangle$ directions of the sapphire substrate (and relate to all figures a-d)

The arrows in Figure 35(a) mark the $\langle 1\bar{1}00 \rangle$ directions of the sapphire substrate (and relate to figures a-d). The influence of the substrates' symmetry on the Ni dewetting path is clearly evident from the shape of the partially dewetted Ni and from the alignment of the HfO_2 particles. It is clear from these results that the elongated HfO_2 precipitates are aligned along the $\langle 1\bar{1}00 \rangle$ directions, normal to the receding Ni front, illustrating the dewetting path.

The Hf concentration in the Ni films was increased from 0.5at.% to 5at.% (above the solubility limit) in order to ensure sufficient Hf for equilibrium segregation to the interface with the sapphire (if the thermodynamic driving force for this is present). The results that are seen in Figure 35 show the opposite effect; Ni actually dewetts away from the HfO_2 in order to eliminate Ni-HfO_2 interfaces. To further confirm this, a TEM specimen was prepared from an elongated HfO_2 particle still in contact with a Ni island. The black arrow in Figure 36(a) shows the location from which the TEM specimen was extracted, and Figure 36(b) is a high-angle annular dark-field STEM micrograph of the interface area.

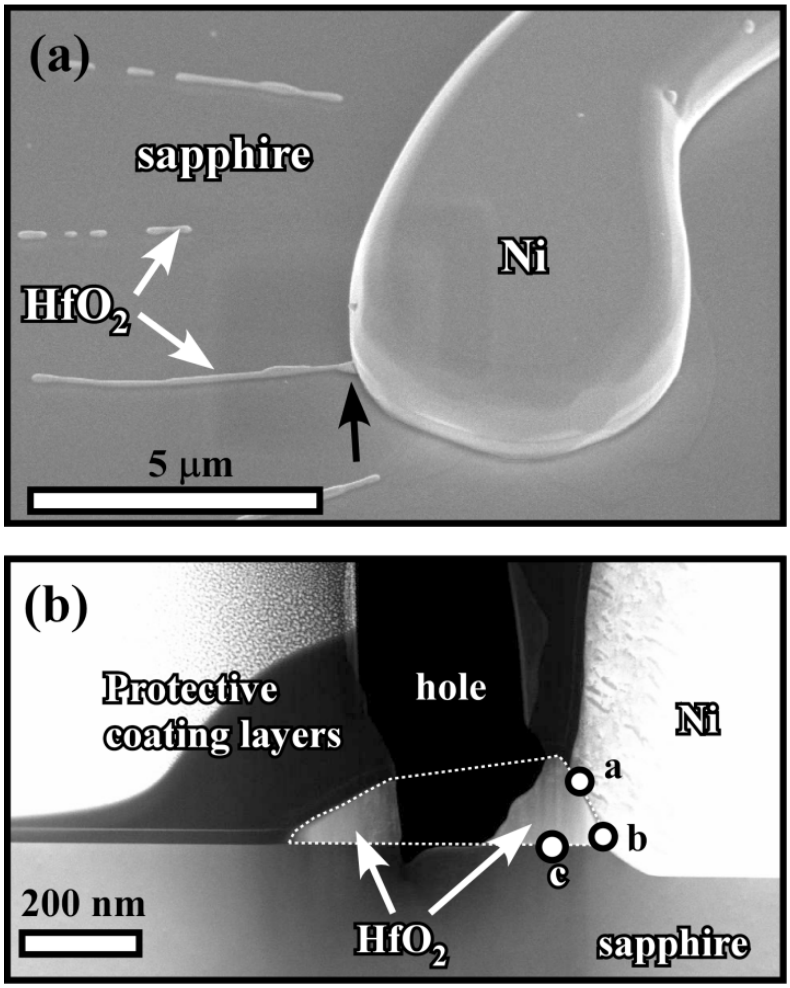

Figure 36: (a) SEM micrograph (inclined view) showing a HfO_2 stripe in contact with partially dewetted Ni. (b) Z-contrast STEM micrograph of the contact area between the HfO_2 and the Ni

(marked by the black arrow in (a)). Point a-c mark areas that were further analyzed by HRTEM, and are shown in Figure 37(a-c), respectively.

A more detailed examination of the Ni-HfO_2 interface was done using HRTEM. Figure 37 shows two areas of the same interface. Figure 37(a) presents the side closer to the ambient (marked by (a) in Figure 36(b)). From this micrograph it is evident that the Ni is not in contact with the HfO_2 and that they are actually a few nm's apart (this gap was filled with FIB-deposited carbon at the initial stage of TEM specimen preparation). Figure 37(b) shows another area of the Ni-HfO_2 interface, adjacent to the triple junction with Al_2O_3 (marked by (b) in Figure 36(b)). It is clear that the Ni is still connected to the HfO_2 at this part of the interface. From these findings we conclude that the examined Ni particle was in the course of separating from the elongated HfO_2 particle, and that the Ni indeed diffuses away from the HfO_2 and prefers to be in contact with the Al_2O_3 instead.

A HRTEM micrograph of the HfO_2-sapphire interface is shown in Figure 37(c) (area (c) from Figure 36(b)). The orientation relationship deviates from the $HfO_2(111)[110] \,||\, \text{sapphire}(0006)[11\bar{2}0]$ orientation relationship by 6.5° about the zone axis.

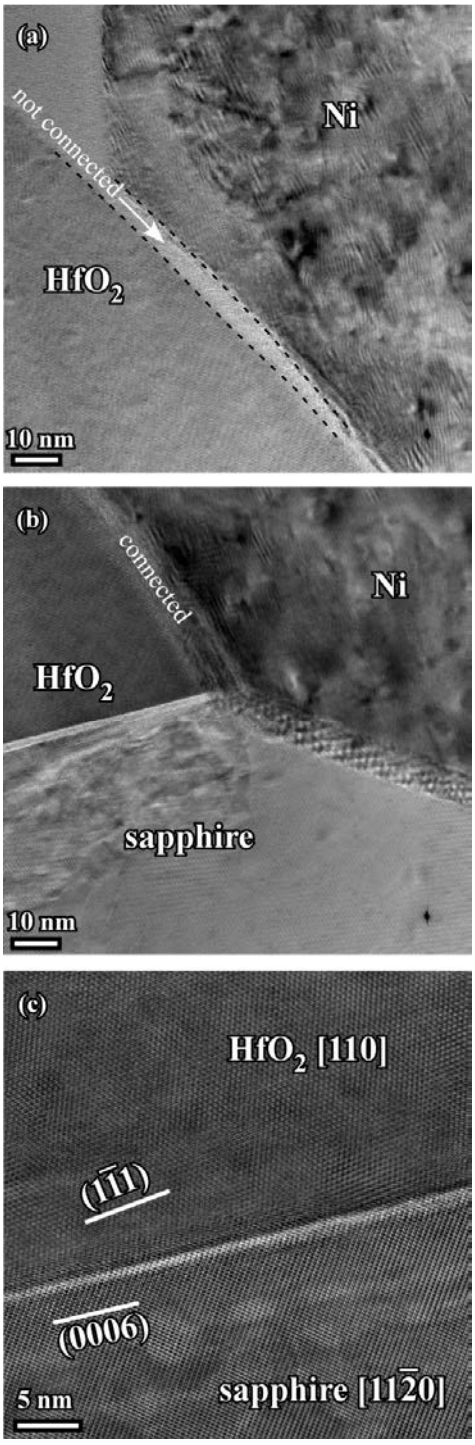

Figure 37: TEM micrographs of (a) the interface between Ni and HfO_2, close to the free surface of the HfO_2 stripe (marked as point (a) in Figure 36(b)). (b) The same interface, closer to the triple junction with sapphire (marked as point (b) in Figure 36(b)), and (c) HfO_2-sapphire interface (marked as point (c) in Figure 36(b)).

Figure 38 is a schematic drawing which summarizes the experimental results and the dewetting sequence of Ni(Hf) on sapphire. At the initial stage of dewetting, Hf diffuses to and precipitates (probably as HfO_2) at the Ni-Al_2O_3 interface. This is a preferred site for heterogeneous nucleation of holes in the Ni film. The dewetting kinetics are affected by the crystallography of the substrate (and perhaps also by that of the Ni film), and the fastest rate of dewetting is along the sapphire $\langle 1\bar{1}00\rangle$ directions (Figure 38 (b). Subsequently, Hf diffuses to the triple-lines (Ni-sapphire-ambient) and more precipitates are formed. Additional diffusion of Hf coarsens the existing precipitates. This happens at a similar rate to that of Ni diffusion, so that the Hf follows the receding triple line and forms elongated precipitates that are aligned along the sapphire $\langle 1\bar{1}00\rangle$ directions (Figure 38(c)). At the final stage of dewetting, interface and surface energy minimization is achieved and the specimen consists of separated Ni and HfO_2 particles (Figure 38(d)).

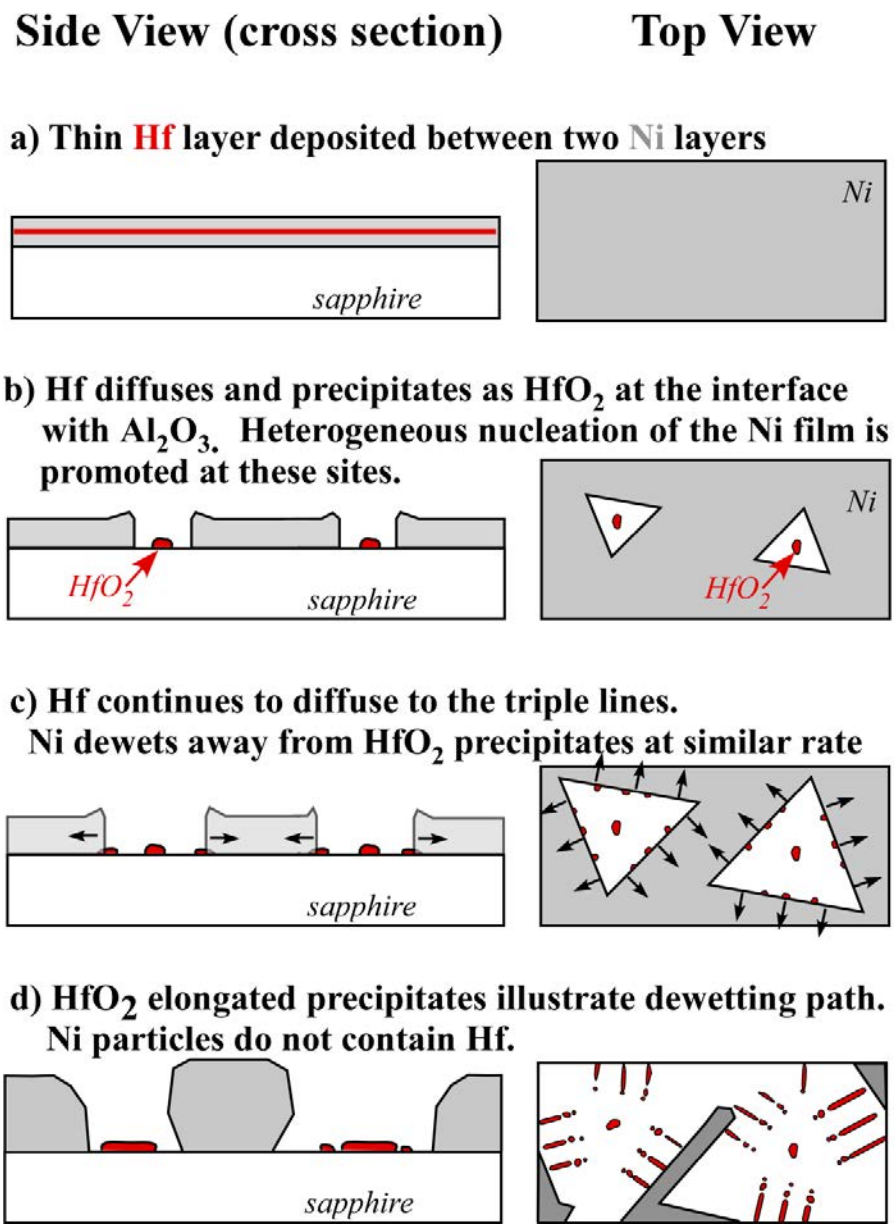

Figure 38: Schematic drawing of the proposed model of Ni(Hf) dewetting on sapphire.

It is not clear whether Hf oxidation occurred at the interface (by reduction of the Al_2O_3) or at the triple line (when exposed to the ambient). Moreover, the driving force for Hf segregation to the triple line is not clear. One option is that the Ni-HfO_2 interface energy is larger than that of Ni-Al_2O_3 and separation of the HfO_2 and Ni is required in order to reduce the surface energies of the system. Another option is that the Hf anisotropically

segregates to the free surface of sapphire, where it oxidizes. The following section describes two experiments that were designed to clarify this issue.

4.3.4 3.2 Ni–HfO_2 interface

In order to determine whether the driving force for Hf segregation is the formation of HfO_2, a thin non-continuous layer of Hf was deposited on the sapphire substrate and was heat treated under the same conditions used for dewetting the Ni (1623K, 5 hours, $P(O_2)=10^{-20}$[atm]). The result was a uniform coverage of HfO_2 nano-particles. On top of this substrate (and HfO_2 particles) a continuous 250nm thick layer of Ni was deposited, and again dewetted. At the end of this process, the small HfO_2 islands that were formed in the first stage remained distributed on the free surface of the sapphire, and larger HfO_2 particles were found at the Ni-sapphire triple lines (see Figure 39). The Ni-sapphire interface was free from HfO_2 particles. The arrow in Figure 39 indicates the original position of a Ni-sapphire triple line, which is marked by larger HfO_2 particles. This result shows that Hf oxidation is not the driving force for the microstructure reached during dewetting, and indicates that two-phase dewetting to minimize the total surface and interface energies of the system is responsible for the morphological changes.

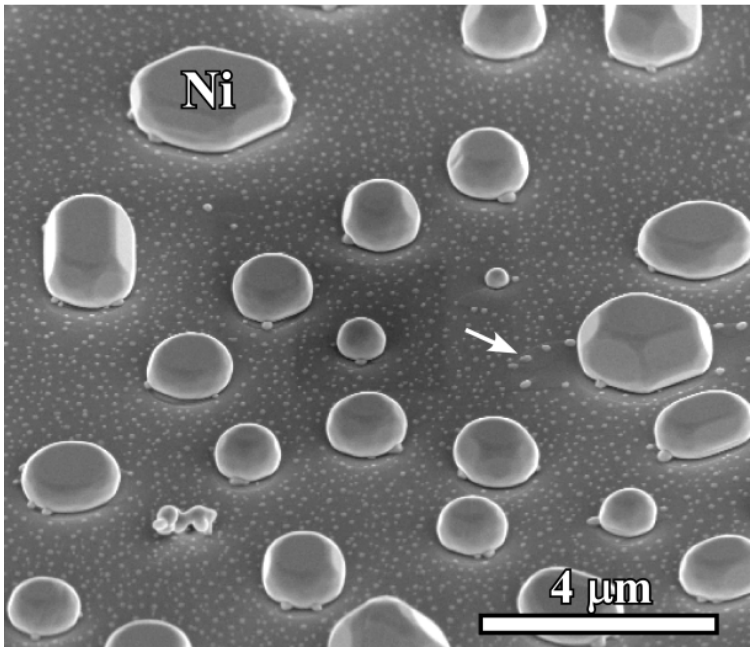

Figure 39: Ni particles dewetted on a sapphire substrate uniformly covered with HfO_2 nano-particles. The nano-particles segregated to the Ni-sapphire triple junction during the Ni dewetting.

In order to determine the difference between Ni-Al_2O_3 and Ni-HfO_2 interface energies, and to corroborate the findings shown above, Ni was dewetted on a (polycrystalline) HfO_2 substrate (see Figure 40). FIB was used to extract a cross section TEM specimen from the center of a relatively small equiaxed particle (shown in Figure 41).

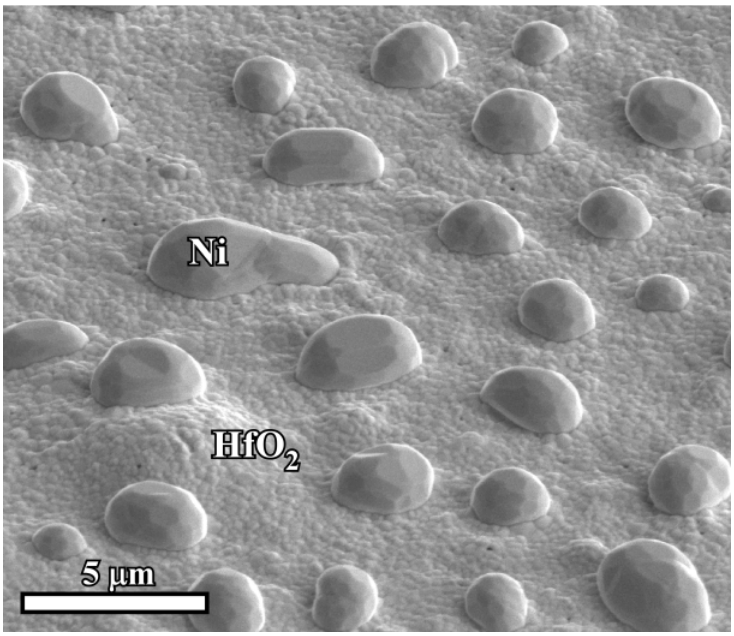

Figure 40: Ni dewetted on polycrystalline HfO_2.

The cross section micrograph of the Ni particle was used to measure the Ni-HfO_2 interface energy and the surface energy of HfO_2, according to the dihedral angle analysis at the triple line (equation 7) (neglecting contributions from torque).

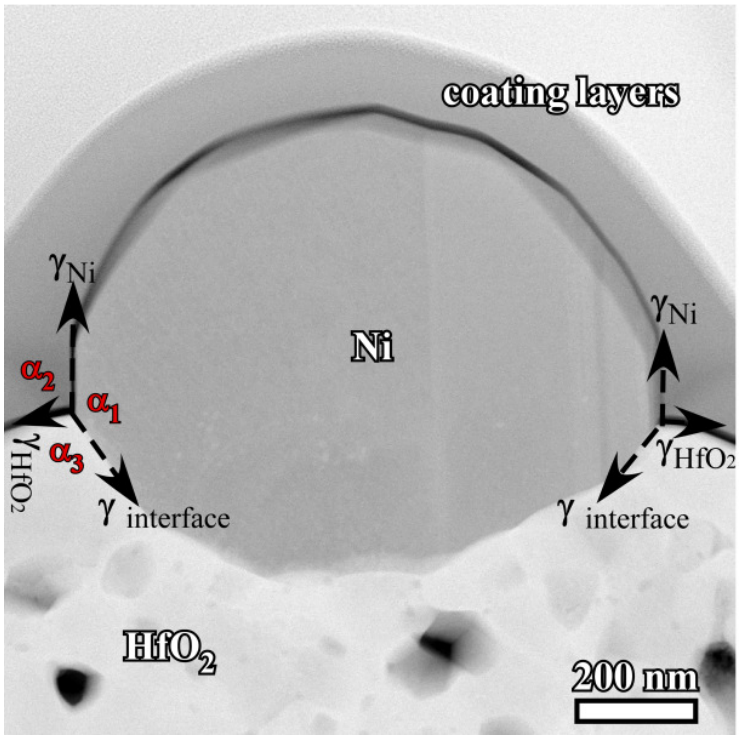

Figure 41: Z-contrast STEM micrograph of a Ni particle dewetted on polycrystalline HfO_2. An energy balance at both triple junctions was used to measure Ni-HfO_2 interface energy. Holes in the HfO_2 are also evident in the form of dark contrast.

For the calculation, the absolute value of the pure Ni(111) surface energy (2.05J/m^2) was taken from the present study (see Appendix 9). Using the surface energy of pure Ni is valid in the presence of Hf, since Hf has a higher surface energy than Ni, and is not expected to segregate to the Ni free surface and reduce the surface energy [126]. The measured Ni-HfO_2 interface energy for one triple junction was 2.87 J/m^2 and for the other 2.53 J/m^2, giving an average value of 2.7±0.4 J/m^2. This value is significantly higher than the Ni-Al_2O_3 interface energy (2.16±0.2 J/m^2) that was measured using the same experimental conditions [127], proving that the driving force for the separation of HfO_2 and Ni at equilibrium is driven by the reduction of interface/surface energies. From the energy balance in Figure 41, the surface energy of HfO_2 was also calculated. The value measured from one triple junction is 1.8 J/m^2 and from the other 1.4 J/m^2.

5. Discussion

5.1 Solid State dewetting

Shape evolution towards equilibrium depends upon the initial state of the system. In this work, the initial state is a thin film that develops side facets according to the ECS during solid state dewetting. The top (111) facet is the last one to reach equilibrium and is usually larger than the side (111) facets, except for particles smaller than ~800nm as can be seen in Figure 9 and Figure 17. This behavior suggests that a nucleation barrier prevents only the top facet from reaching the equilibrium size. This limitation is more significant for larger facets (and particles). Mullins and Rohrer [20,21] also predicted the existence of such a nucleation barrier for a facet to reach an equilibrium size, which is more significant for larger facets. If the initial shape was a sphere (as in the case of solidifying drop), it is expected to develop facets that will increase in size at the expense of the rounded surfaces, as described in equation (2). However, this equation considers only surface diffusion and not other processes such as evaporation-condensation that may also take part in equilibration, especially at such high homologous temperatures. In the case of growth shapes (as in solid state dewetting), a polyhedral crystal will form during the initial stages of dewetting and the rounded surfaces will only develop at the final stages of equilibration.

5.2 Equilibrium Crystal Shape of Ni

In the present work we have shown that the ECS of Ni equilibrated in system C (clean furnace, $P(O_2)<10^{-20}$atm, see Figure 20Figure 1), is completely faceted with no round surfaces and contains high index facets. This is very unusual for FCC metals which have partially rounded equilibrium shapes truncated by low index facets, as seen for Au and Cu in Figure 42.

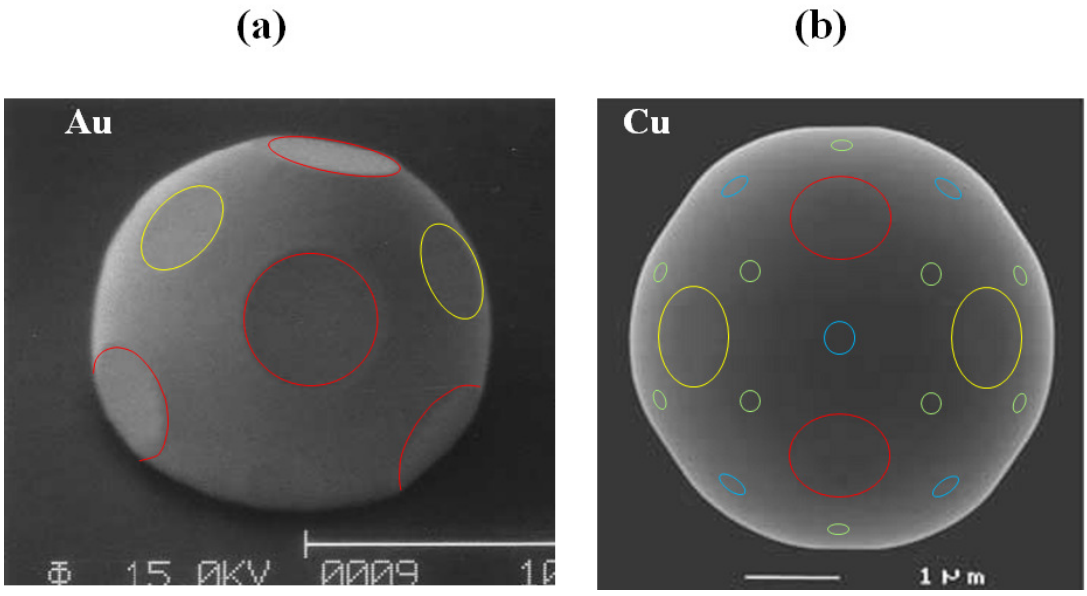

Figure 42: ECS of: (a) Au equilibrated on SiC [128] (b) Cu on sapphire [129]. (111) facets are marked in red, (100) facets in yellow, (110) in blue and (311) in green.

It is possible that the fully faceted Ni crystals represent growth shapes rather than an equilibrium shape. However, while impurities and kinetic effects may have prevented full equilibration in these experiments, we think that system C is the closest to equilibrium for the following reasons:

a) In contrast to previous equilibration experiments of Cu [24], it is less likely that impurities originated from the Ni target (which was 99.9995% pure for systems B and C). Impurities may have come from the sapphire substrate (99.99%, probably containing several ppm of Na, Ca, Si), but these were not detected by APT.

b) The very long equilibration times required for Cu was for particles that were about 5µm in diameter. According to equation (2), the time for shape equilibration depends very strongly on the particle size, and the sub-micron Ni particles are expected to have reached equilibration.

c) Since the present experiment was done in the solid state, equilibration kinetics and their mechanisms are quite different than the ones proposed by Nichols and Mullins and Mullins and Rohrer [19,20]. In their models, shape changes are calculated for surface-diffusion processes on particles that are initially spherical (as discussed above), and develop facets that are tangentially connected to the neighboring vicinal

orientations. In this work, where the initial geometry is a flat continuous film, the facets have mostly sharp edges, and evaporation-condensation is also expected to take part in mass transport. To the best of our knowledge, no model has been formulated to describe the time required to equilibrate solid particles similar to the ones seen in this work.

5.2.1 Surface energy anisotropy

The results presented here show that the crystal shape of pure Ni is completely faceted with a maximum anisotropy of 8%, and does not include all orientations. Usually, an increase in surface anisotropy and the appearance of high index orientations are attributed to lower temperature, surface segregation, or surface structure (microscopic) reconstruction [18,30]:

5.2.1.1 Surface Reconstruction

Since Ni has an absolute surface energy which is larger than most FCC metals, it is expected that the existence of a round surface that has a high number of unsaturated bonds (or a small number of nearest neighbors) will not be energetically favorable. This can result in a driving force for surface reconstruction that is larger than for other metals. Although it is known that Ni surface reconstruction occurs at room temperature, no reports were found in the literature about reconstruction above room temperature [130,131].

5.2.1.2 Effect of Temperature

In order to observe the Wulff shape of particles equilibrated at 0.97Tm, the specimen must be cooled down very rapidly to prevent surface diffusion from changing the shape according to the temperature change. Unfortunately, in the present experimental apparatus rapid cooling cannot be done, and the specimens were cooled at a rate of 15 K/min. At this rate it took 36-40 minutes to decrease the temperature to 0.6Tm, where no significant diffusion is expected to occur. Such a cooling duration could have some

influence on the final examined shape. However, since the cooling rate was the same for all three systems, the results can be a basis for comparison.

5.2.1.3 Surface Composition

The fact that no impurities were detected on the surface of system C does not necessarily mean that this system represents the Wulff shape of clean Ni. First, atom probe analysis could not be used to quantify carbon or oxygen adsorption, due to specimen transfer/storage and the carbon coating used to prevent charging. Both carbon and oxygen are expected to influence surface anisotropy if they are present at the surface. Even if other impurities (like S which is a common impurity in Ni) were present at the initial stage of dewetting, and have evaporated, the surface still needs sufficient time to allow the crystal to re-equilibrate according to the new anisotropy (that of pure Ni). In the work by Chatain *et al.* [24], Cu films were dewetted in the liquid state and were equilibrated in the solid state under a reducing atmosphere. Impurities (such as sulfur) that were present in the initial film significantly increased the anisotropy and formed faceted steps around the larger facets. By equilibrating the particles under flowing $He+H_2$, the surface was cleaned of all impurities. However, it still took the crystals 78 hours to equilibrate into the new ECS (although the initial shape was very close to the final ECS of pure Cu).

5.2.2 Simulations of the equilibrium shape

Although the facets and their relative stability identified by TEM agree very well with those calculated using Wulffman, several discrepancies were found in the relative surface energies of the stable facets. In system A, the relative energy of the {100} facet is lower than the measured value (see Table 2). The reason for this is that the top (100) facet that was used to determine the relative energy is slightly larger than the side {100} facets. In other words, the top facet hadn't fully reached its equilibrium size. The projection chosen for TEM analysis does not include the side {100} facets, and thus this error in measurement could not be considered. However, the shape simulation did include the projected size of the side facets (seen from the top view in Figure 18 and Figure 24a). Hence, for system A, the calculated anisotropy is more correct than the measured one.

The calculated anisotropy for system C is lower for almost all facets. The reason for this is that the size of the {111} facets in the simulation is smaller than the real size of these facets (i.e., it is thought to have a larger relative energy). Since all energies in Table 2 were taken relative to that of {111}, the resulting values reflect a lower anisotropy. Thus, for system C, the experimental measurement (as conducted using TEM) is more accurate than the simulation.

5.2.3 Effect of $P(O_2)$ and Fe Contamination

It is clear that the dominant factor that determines the anisotropy is different in all three systems. In system A, it is believed that the main factor is the presence of a larger amount of oxygen in the gas phase. In system B, Fe is the dominant factor, although it may be a combined effect with oxygen. According to the APT profile, the Fe concentration at the surface is similar to that of the bulk, i.e., there is no Fe surface segregation. This is explained by the similar surface energies of Fe and Ni (γ_{Fe} is slightly higher) and the relatively large enthalpy of mixing [102]. Although the influence of Fe on the surface anisotropy is dramatic, it is not clear what lowers the surface energy of rough surfaces and de-stabilizes higher index planes. One possible explanation is the formation of Fe-O bonds at the surface. In System C, the main reason for the high anisotropy and the stability of high index planes was discussed above.

5.3 Ni–Al_2O_3 Interface Structure and Energy

5.3.1 Interface Energy

Using Winterbottom's equation the interface energy of equilibrated pure Ni-Al_2O_3 interfaces was determined to be 2.16 J/m^2. Taking into account the surface energies of the interface plans the thermodynamic work of adhesion can be calculated according to

$$W_{ad} = \gamma_{Ni} + \gamma_{sapphire} - \gamma_{interface} \quad \textbf{(10)}$$

giving W_{ad}=0.96 J/m^2. This value is low compared to the W_{ad} calculated by Zhang ***et.al*** [77]. However, this comparison is problematic since in their DFT calculation the structure of the interface is different than the equilibrium structure and the surface energies are not those of the relaxed free surfaces. In addition, this calculation relates to the Al_2 interface termination.

To the best of our knowledge, only a single attempt was made in the past to experimentally measure the Ni-Al_2O_3 interface energy. Pilliar and Nutting [60] also used the Winterbottom relation for the same interface at a temperature of 1273K. However, instead of TEM they used tilted projections in the SEM to determine the particle's shape. In their work, they used lower surface energies values compares to the ones used in this work, although at a lower temperature the surface energies are known to increase. In addition, the ratio R_1/R_2 that was measured by Pilliar and Nutting is higher than the one measured in this work, which is a good indication of a reduction in surface energy of the Ni due to the presence of impurities (Ni purity was not reported). The contribution of low surface energies and high particle aspect ratio are opposite in equation (8). As a result, the interface energy measured by Pilliar and Nutting (2.14 J/m^2) is, by chance, very similar to the one measured in this work.

5.3.2 Interface Structure

After determining the $P(O_2)$ threshold for Ni-spinel formation as a bulk layer at Ni-Al_2O_3 interfaces, Brydson ***et al.*** raised the issue of whether a spinel phase at the nanometric length scale exists at the interface even below that threshold value. This question is important since the presence of such a phase would be expected to affect the interfacial properties. The result presented here clearly show that such a layer does not exist at $P(O_2)=10^{-20}$[atm].

The interface termination was calculated by Zhang ***et al.*** for a wide range of $P(O_2)$ at T=1300K and T=1750K [72]. According to the calculation, at both temperatures the most stable interface at low $P(O_2)$ is Al_2 terminated. However, only the O-terminated interfaces had a change in symmetry of the terminating Ni layer (described as 'buckling' of the Ni layer by 0.55Å normal to the interface). The fact that the structure of the Al_1-terminated

interface is different than the one determined in this work, suggests that the DFT calculation may not reflect the equilibrated structure of the interface, but rather represents a metastable interface state. A similar trend was reported by Wang *et al.* [70] who found from DFT simulations (of a Ni-Al_2O_3 interface that was also stretched to coherency) that the Ni terminating layer differs in structure from that of bulk Ni layers and contains vacancies and corrugations. Shi *et al.* [71] performed first principles calculations to demonstrate the effect of the different translations of the Ni with respect to the sapphire, for the Al_1 termination. Although their work was limited in size, they showed that the spacing of the layers parallel to the interface is the smallest when the Ni is positioned on top of an oxygen atom. This change in interlayer spacing is reflected in the present study by the distortion of the Ni layer at the area where the Ni is positioned on top of the oxygen in order to decrease the Ni-O bond length. Still, the complete picture of the reconstructed interface cannot be completely understood from DFT because of size limitations, and in all calculations the structure of the interface is assumed to be only the coherent part of what has been shown here to be a semi-coherent interface. Obviously, this is not the case for equilibrated Ni-Al_2O_3 interfaces.

Long *et al.* [73] examined the structure of *incoherent* Ni-Al_2O_3 interfaces using an energy minimization technique that, unlike DFT, is not limited by size. They were able to predict the existence of a reconstructed Ni layer at the interface that absorbs the misfit strain energy. This alternative mechanism for strain energy reduction also allows forming shorter Ni-O bonds. Unfortunately, the simulation was limited only to interface regions where the Ni was positioned adjacent to oxygen sites, and does not describe the entire interface structure (although this calculation method allows simulating larger systems). Nevertheless, their conclusion that interfacial reconstruction occurred is unusual, since to the best of our knowledge, there is no experimental proof of interface reconstruction at metal-ceramic interfaces.

To the best of our knowledge, the atomistic structure of Ni-Al_2O_3 interfaces was not examined *experimentally* before. However, the structure of 0.18ML of Ni layer deposited on a sapphire substrate was investigated very recently by Venkataramani *et al.* using atomic force microscopy operated in the non-contact mode [132]. In their work they very nicely show that the reconstructed sapphire surface can influence the distribution of

agglomerated (particles dewetted), providing a "bottom-up" approach for patterning of metal (Ni) clusters on the surface of sapphire. There is no doubt that the reconstruction affects the distribution of the particles, although a fully periodic distribution is not obtained. Exactly how the reconstructed surface interacts with the Ni particles was not shown, but rather estimated based on DFT of Ni interacting with the ideal (1x1) sapphire (0001) surfaces.

The presence of a reconstructed layer was also reported for several monolayers of MgO deposited on Pt, Pd, Ag, or Mo [133,134,135]. The reconstruction symmetry also reflects the coincidence between the two lattices. However, this structure was only stable for a film thickness of 5ML, after which lattice dislocations were formed.

The reconstruction found in the present study is described as: $(2.5\sqrt{3} \times 2.5\sqrt{3}\ R30)$. This notation reflects the symmetry of coincidence between the (111) Ni layer (the reconstructed layer) and the sapphire basal surface. The basal surface plane on Al_2O_3 is known to undergo reconstruction at elevated temperatures (above ~900°C) at low $P(O_2)$ as a result of oxygen evaporation. Several surface symmetries were identified according to the following sequence [9,136]:

Table 4: surface reconstruction of sapphire (0001)

Temperature Range	Reconstruction Symmetry
1050°C-1150°C	$\sqrt{3} \times \sqrt{3}\ R30$
1150°C-1350°C	$3\sqrt{3} \times 3\sqrt{3}\ R30$
1350°C < T	$\sqrt{31} \times \sqrt{31}\ R9$

While the $\sqrt{31} \times \sqrt{31}\ R9$ is the most studied surface structure [137,138,139,140,141], little is known about the two other structures. Vilfan ***et al.*** [9] studied the $3\sqrt{3} \times 3\sqrt{3}\ R30$ surface structure and determined that the top Ni layer is arranged as a (111) layer of bulk Al (with a ~2% strain). This layer is located above two or three additional Al layers that are arranged according to the sapphire symmetry. No vertical displacement of the atoms was reported.

In this study, the sapphire substrates were not annealed prior to the film deposition. Since the depositions were performed ex-situ, at room temperature and on the O-terminated surface, it is not possible that the surface of sapphire was reconstructed during deposition. This means that the reconstructed interface structure develops at high temperature and not as a result of substrate patterning during deposition. In addition, the stability of the reconstructed interface is larger than the reconstructed sapphire surface since, unlike the free surface, the interface structure did not change upon cooling or exposure to higher $P(O_2)$. This can be attributed to slower oxygen diffusion or to the more rigid nature of the Ni terminating layer, being constrained by crystals on both sides.

The presence of a reconstructed layer at the interface serves to reduce misfit strain, as an alternative mechanism to introducing misfit dislocations. It is not clear why the former mechanism is preferred over the latter in this case. One suggestion is that the driving force for reconstruction is the strong affinity of Ni to O (in the sapphire) that causes a distortion in the Ni sites located on top of the oxygen.

Another suggestion is that a large density of dislocations is required to compensate for the relatively large misfit at Ni-Al_2O_3 interface (9.3%), making this mechanism ineffective. This is similar to low-angle grain boundaries that have increasing dislocation density with an increasing misfit angle, up to a certain value in which the boundary will not contain periodic lattice dislocations. If this assumption is correct, similar structures are expected to be present at other metal-ceramic interfaces with large misfit. In an experimental study of the Cu-Al_2O_3 interface Dehm ***et al.*** were able to show that the interface is incoherent since no misfit dislocations were identified along the interface [142]. Since the Cu-Al_2O_3 interface also has relatively large misfit (~7.4%) it is possible that a reconstructed layer also develops. However, due to microscopy limitations at the time of Dehm's study, the atomistic arrangement at the interface was not resolved and so the mechanism of strain accommodation remained unclear.

5.4 Hf-doped Ni-Al_2O_3 Interface

5.4.1 Hf solubility in Ni

The results shown here indicate that Hf is in fact insoluble in Ni at 1623K, contradicting the 0.5at.% solubility determined from the equilibrium phase diagram [125]. The most commonly used Ni-Hf phase diagram (and, to the best of our knowledge, the only one in the literature) is based on alloys that contain up to 3at.%Zr. We believe that the presence of Zr increased the solubility limit of Hf (according to that in the ternary Ni-Zr-Hf system) and cannot be used to draw conclusions on Hf solubility in pure Ni, especially at such low concentrations. In this study, we used 99.99% pure Hf that does not contain Zr (detection limit < 100 ppm) and according to our calibrated WDS measurements, the Ni bulk does not contain dissolved Hf at 1623K (detection limit = 50 ppm).

5.4.2 Anisotropy of Dewetting

The anisotropic dewetting of the Ni is obviously affected by the sapphire (0001) surface. The orientation of the Ni with respect to the sapphire was investigated in a previous study only at the initial and final stages of dewetting. It is known from x-ray diffraction that the as-deposited Ni layer has a (111) preferred orientation parallel to the (0001) sapphire substrate (both interface plans have a 3-fold symmetry), while a $Ni(111)\langle 110\rangle||sapphire(0001)\langle 1\bar{1}00\rangle$ low-index orientation relationship is preferred at equilibrium. However, it is not clear at which point of the dewetting process the Ni develops this orientation relationship. For this reason, knowledge of the final Ni orientation cannot be used to draw conclusions regarding the contribution of the Ni symmetry to the dewetting kinetics and anisotropy.

5.4.3 Hf Oxidation

It is not clear from the results at which stage the Hf oxidizes. The $P(O_2)$ of these experiment is not low enough to prevent Hf oxidation. According to the Ellingham diagram the $P(O_2)$ required for Hf oxidation at 1623K (10^{-29} [atm]) is lower than that of

Al (10^{-28} [atm]), so it is not thermodynamically possible to have Al_2O_3 and metallic Hf under the same equilibration conditions . During the deposition process of the Hf by e-beam evaporation, the substrates were initially covered. This allowed the evaporated Hf to reduce the oxygen partial pressure in the evaporation chamber, so that oxidation of the Hf during deposition on the substrates is not likely. One possibility is that the Hf reduced the Al_2O_3 at the interface and oxidized there. This is supported by the Ellingham diagrams that state that the energy of formation of HfO_2 is slightly lower than that of Al_2O_3. In addition, it can be seen from Figure 37(b) that the sapphire substrate adjacent to the interface with HfO_2 shows a contrast different from the areas under the Ni (also seen in Figure 37(b)). This contrast might suggest that partial reduction of the Al_2O_3 took place leaving a large concentration of oxygen vacancies. EELS was used to see if varying oxygen concentration could be detected in the sapphire, but no change was detected between the different areas of the substrate. It is possible that sapphire re-oxidation occurred during TEM specimen preparation, specimen transport, and/or storage, making the measurement of oxygen vacancies in a thin specimen much more complicated. Another possibility is that the Hf segregated from the bulk directly to the triple-line and was oxidized by the ambient. In this case, the damaged sapphire area adjacent to the HfO_2 islands remains unexplained.

5.4.4 Ni–HfO_2 Energy Measurement

The use of equation (**6**) for the measurement of solid-solid interface energy neglects the contribution of torque forces. These forces act perpendicular to any singular surface orientation (e.g. facet) and prevent a change in orientation to the neighboring orientations (with higher energies). This means that the triple junction between 3 facets is not completely free to adopt all geometries and does not always directly reflect the energy balance. This inaccuracy is greater for larger energy anisotropies. However, in the case of the HfO_2-Al_2O_3 interface, this anisotropy is moderate, since from Figure 41 the shape of the interface is relatively curved and is almost unaffected by the different orientations of the HfO_2 grains. It is estimated that the neglected torque results in an error of 15% to the measured interface energy.

It is clear from this study that Hf does not stabilize Ni-Al_2O_3 interfaces thermodynamically, and if possible it will prefer to precipitate on the sapphire substrate and not to be in contact with Ni. The role of Hf in commercial bond-coats is not necessarily the same, since other impurities are also present in the alloy that can completely change the characteristics of the system. On the other hand, Hf has been reported to segregate from the bond coat, across the interface and precipitate as HfO_2 inside the oxide [143,144,145]. This may indicate that while the compositions of our experimental system are different from commercial systems, from the point of interfacial energy the presence of HfO_2 at the interface is undesirable.

6. Summary and Conclusions

The goals of this research were to quantitatively determine the interface energy for an *equilibrated* system, and to correlate the results with the atomistic structure of the *same* interface. In order to achieve this goal, a comprehensive study of the surface energy of Ni and its anisotropy was also conducted. In addition, the effect of Hf segregation in the structure and energy was investigated.

Solid-state dewetting experiments of pure Ni films were performed under controlled working conditions. The crystal shape was analyzed by three complementary characterization methods (SEM, TEM and Wulffman simulations), and for the first time the nickel crystal shape was related to the chemical composition of the surface. The crystal shape was found to be almost completely facetted with both dense and high index planes, in contrast to that expected for an FCC metal. At $P(O_2)=1*10^{-9}$ atm, {012} and {013} facets were stabilized, and at $P(O_2)<1*10^{-20}$ atm, {135} and {138} facets were stabilized. The addition of Fe decreased the anisotropy dramatically, de-stabilizing high-index planes. The kinetics of particle shape equilibration from the geometry of a thin film was studied. A major difference was found between shape evolution in the directions parallel and normal to the substrate. This resulted in particles that had side facets with similar proportions (i.e., the same facet diameter to particle diameter ratio) but a top facet that is significantly larger, indicating a nucleation barrier preventing the top facet from reaching equilibrium.

The solid-solid interface energy was measured and aberration corrected HRTEM was used to identify the atomistic structure of the same interfaces. It was found that the interface between Ni and (0001) sapphire undergoes reconstruction, resulting in a $2.5\sqrt{3} \times 2.5\sqrt{3}\,R30$ interfacial unit cell. This is a specific interfacial state with an energy of 2.16 J/m^2, which in the past has been defined as an incoherent interface. It is believed that the reconstructed interface accommodates the very different structures of the two bulk phases at the interface, and this is predicted to be a viable mechanism to reach a low energy interface between very dissimilar materials.

In addition to undoped interfaces, this model study was designed to provide specimens from which the interface energy could be measured as a result of Hf segregation to the interface. In contrast to the existing literature, Hf was not found to segregate to Ni-alumina interfaces. Furthermore, due to the limited solubility limit and oxygen partial pressure, the Hf oxidized and formed small HfO_2 particles from which the Ni films dewetted. This is explained by the measured difference in interface energy between Ni-alumina (2.16±0.2 J/m^2) versus Ni-HfO_2 (2.7±0.4 J/m^2). As a result, in the experimental configuration used here, the Hf will prefer to form as HfO_2 particles on the free surface of the Al_2O_3. This Ni-Hf separation process occurs via anisotropic dewetting of the Ni film (fastest along the sapphire $\langle 1\bar{1}00 \rangle$ directions) simultaneously with HfO_2 precipitation at the Ni-Al_2O_3-ambient triple line. The Hf probably oxidizes by reducing Al_2O_3 at the interface.

There have been many excellent studies of the structure and chemistry of metal-ceramic interfaces. Most of the detailed studies were conducted on bi-crystals of interfaces formed by deposition methods such as molecular beam epitaxy. These interfaces do not necessarily present low energy configurations. The present experimental approach, based on solid-state dewetting, generates low energy equilibrated interfaces, which provide for both thermodynamic and crystallographic analyses.

7. Open Questions & Future Work

Further analysis of the Ni surface structure may provide insight as to the existence of surface reconstruction and can help to understand the large surface anisotropy.

The effect of the starting conditions on the interface structure is very significant in DFT calculations. It would be interesting to see if this can predict the interface reconstruction observed in this work, given the correct starting conditions, in spite of the size limitation.

One of the most interesting questions that emerged from this study is why some interfaces develop misfit dislocations in order to reduce strain, while others (such as in this case) develop a reconstructed layer and an incoherent interface. This question can be addressed by calculations of the affect of misfit strain of different magnitude on the strain accommodation mechanism.

The current experimental setup did not allow for a gradual increase of the $P(O_2)$. It would be interesting to see how the $P(O_2)$ level affects the interface structure.

The experimental setup used in this study allows for the introduction of many dopants to the Ni layer. It would be very interesting to see the effect of other dopants on the Ni-Al_2O_3 interface structure and energy.

8. Appendix I

Winterbottom Analysis

The analysis is based on surface and interfacial energy considerations of an equilibrated particle on a foreign substrate, under conditions of constant temperature, volume and chemical potential. The variation in the free energy of the system, $\delta\Psi$, caused by any shape change equals zero at equilibrium, and is expressed by:

$$\delta\Psi = \delta\int_{SV}\gamma_{SV}dA + \delta\int_{SP}\gamma_{SP}dA + \delta\int_{PV}\gamma_{PV}dA = 0 \qquad (11)$$

Where SV is the substrate-vapor surface, SP is the substrate-particle interface, and PV is the free surface of the particle. While equation (11) describes the general solution for any particle-substrate configuration, there is no general solution of this problem other than knowing all of the surface energies and their anisotropies. However, a simplification can be made in the case of an interface which is flat and coplanar with the substrate. In this case, the sum of the interface area A_{SP} and the free surface of the substrate A_{SV} equals the original surface of the substrate without a particle present (S). Thus, the first term in equation (11), which expresses the change in the substrate-vapor surface area, can be written as:

$$\delta\int_{SV}\gamma_{SV}dA = \delta\int_{S}\gamma_{SV}dA - \gamma_{SV}\delta A_{SP} \qquad (12)$$

Since the value of S is not influenced by any shape changes of the system, the first term on the right side of equation (12) will be zero. Substituting equation (12) in equation (11) yields:

$$\delta\int_{SP}\gamma_{SP}dA + \delta\int_{PV}\gamma_{PV}dA - \gamma_{SV}\delta A_{SP} = 0 \qquad (13)$$

The last term in equation (13) can be replaced with the following integral:

$$\gamma_{SV}\delta A_{SP} = \delta \int_{SP} \gamma_{SV} dA \tag{14}$$

And equation (13) can be written as:

$$\delta \int_{SP} (\gamma_{SP} - \gamma_{SV}) dA + \delta \int_{PV} \gamma_{PV} dA = 0 \tag{15}$$

Winterbottom defined a general surface energy γ* for the particle, which is equal to the particle vapor surface energy for all orientations corresponding to the free surface of the particle, and is defined as γ_{SP}-γ_{SV} at the interface:

$$\text{Particle – Vapor Surface:} \quad \gamma^* = \gamma_{PV} \tag{16}$$

$$\text{Particle – Substrate Interface:} \quad \gamma^* = (\gamma_{SP} - \gamma_{SV})$$

Using this definition, equation (15) can be written as:

$$\delta \int_{P} \gamma^* dA = 0 \tag{17}$$

Thus, the problem of determining the equilibrium shape of a particle equilibrated on a substrate is reduced to a much simpler problem of determining the equilibrium shape of an *equivalent* particle with a surface energy γ*. The solution to this problem is given by equation (18), and is equivalent to the solution developed by Wulff for determining relative surface energies by equilibrium shape analysis.

$$\int_{P} \gamma^* dA \rightarrow \min \tag{18}$$

Thus, the interfacial energy can be determined by measuring two characteristic lengths in the Wulff shape: the distance from the center of the Wulff plot (i.e. the Wulff point) to the interface with the substrate (R_1), and the distance from the Wulff point to the uppermost facet of the particle (R_2), as shown schematically in Figure 4.

9. Appendix II

$P(O_2)$ Measurement

In the experimental apparatus used for systems B and C, the partial pressure of oxygen was controlled by the reaction: $O_2 + 2H_2 \rightarrow 2H_2O$. The specimen was placed in a sapphire tube furnace under flowing Ar + 7%vol.H_2. Since the total pressure was 1 atm, the $P(H_2)$=0.07 atm.

The moisture content in the gas tank (as measured by the manufacturer) is 0.1 ppm. Assuming the moisture level in the chamber is 1 ppm gives a $P(H_2O)$ of $1*10^{-6}$ atm.

The $P(O_2)$ can then be calculated using:

$$\Delta G = -RT \ln\left[\frac{P(H_2O)^2}{P(H_2)^2 P(O_2)}\right]$$

At T=1623 K, ΔG=-313500 J/mol, giving a $P(O_2)$ =$1.6*10^{-20}$ atm.

10. Appendix III

Estimation of the Absolute Solid Surface Energy of Ni

In addition to relative surface energy and thus anisotropy, the data given in the present study was used to estimate the absolute surface free energy of solid Ni. This is an extremely important and fundamental parameter that is rarely measured due to the lack of a rigorous experimental method. In this work, we estimated the solid surface energy using several assumptions and data from the literature:

a) Levitated drop experiments by Brillo et al. [102] were used to obtain the surface energy of *undercooled liquid* Ni at 1625 K. They used the same Ni as used for the dewetting experiments. From the measurements we obtained $\gamma_{(liquid,1625K)}$=1.8 J/m^2.

b) Considering a 20% increase in surface energy at solidification [54] (due to the solid-liquid interface that is formed) gives $\gamma_{(solid,1625K)}$ = 2.16 J/m^2. This value represents the surface free energy of the rounded solid surface.

c) Taking into account the measured surface anisotropy $\gamma_{(\{111\},1625K)}$= 2.05±0.05 J/m^2.

The major assumption in this approach is the 20% increase in surface energy upon solidification, while the advantage is that absolute values of surface energy can be determined for each individual facet. Zero creep experiments can provide a direct measurement of the *average* solid surface energy, and Kumikov and Khokonov suggest that the most reliable published value for the average surface energy of Ni is 1.94 J/m^2 [146], which is close to the value measured here.

11. References

1. Ernst F.. Materials Science and Engineering: R: Reports 1995;14:97.

2. A. Zangwill, Cambridge University Press, (1988), p.15-17.

3. D.M. Lipkin, D.R. Clarke and A.G. Evans, Acta Materialia, **46**[13]: 4835-4850, (1998).

4. J.H. Choi, D.Y. Kim, B.J. Hockey, S.M. Wiederhorn, J.E. Blendell and C.A. Handwerker, Journal of the American Ceramic Society, **85**[7]: 1841-1844, (2002).

5. W.C. Cheng and P. Wynblatt, Journal of Crystal Growth, **173**[3-4]: 513-527, (1997).

6. D. Chatain, P. Wynblatt and G.S. Rohrer, Acta Materialia, **53**[15]: 4057-4064, (2005).

7. I. Manassidis and M.J. Gillan, Journal of the American Ceramic Society, **77**[2]: 335-338, (1994).

8. Z.M. Wang and P. Wynblatt, Surface Science, **398**[1-2]: 259-266, (1998).

9. I. Vilfan, T. Deutsch, F. Lancon and G. Renaud, Surface Science, **505**: L215-L221, (2002).

10. J.J. Métois and P. Müller, Surface Science, **548**[1-3]: 13-21, (2004).

11. K. Arenhold, S. Surnev, H.P. Bonzel and P. Wynblatt, Surface Science, **424**[2-3]: 271-277, (1999).

12. H.P. Bonzel and M. Nowicki, Physical Review B, **70**: 245430-1-9, (2004).

13. G. Wulff, Z. Krystallogr. Mineral., **34**: 449-530, (1901).

14. J.J. Métois and P. Müller, Surface Science, **548**[1-3]: 13-21, (2004).

15. K. Arenhold, S. Surnev, H.P. Bonzel and P. Wynblatt, Surface Science, **424**[2-3]: 271-277, (1999).

16. H.P. Bonzel and M. Nowicki, Physical Review B, **70**: 245430-1-9, (2004).

17. H.P. Bonzel, Progress in Surface Science, **67**[1-8]: 45-58, (2001).

18. J.C. Heyraud, J.J. Metois and J.M. Bermond, Journal of Crystal Growth, **98**[3]: 355-362, (1989).

19. F.A. Nichols and W.W. Mullins, Transactions of the American Institute of Mining, Metallurgical and Petroleum Engineers, **233**[10]: 1840-8, (1965).

20. W.W. Mullins and G.S. Rohrer, Journal of the American Ceramic Society, **83**[1]: 214-16, (2000).

21. G.S. Rohrer, C.L. Rohrer and W.W. Mullins, Journal of the American Ceramic Society, **84**[9]: 2099-2104, (2001).

22. I. Goldfarb, S. Grossman, G. Cohen-Taguri and M. Levinshtein, Applied Surface Science, **238**[1-4]: 29-35, (2004).

23. I. Goldfarb, G. Cohen-Taguri, S. Grossman and M. Levinshtein, Physical Review B, **72**[7], (2005).

24. Chatain D, Ghetta V, Wynblatt P. Interface Science 2004;12:7.

25. Sundquist BE. Acta Metallurgica 1964;12:67.

26. Emundts A, Bonzel HP, Wynblatt P, Thurmer K, Reutt-Robey J, Williams ED. Surface Science 2001;481:13.

27. Heyraud JC, Metois JJ. Surface Science 1983;128:334.

28. Wang ZM, Wynblatt P. Surface Science 1998;398:259.

29. Heyraud JC, Metois JJ. Acta Metallurgica 1980;28:1789.

30. Chatain D, Wynblatt P, Rohrer GS. Acta Materialia 2005;53:4057.

31. Wynblatt P, Chatain D. Reviews on Advanced Materials Science 2009;21:44.

32. Hondros ED, McLean M. In: Structures et Propriétés des Surfaces, (Editions du CNRS: Paris, 1970), p. 219.

33. Cheng W-C, Wynblatt P. Journal of Crystal Growth 1997;173:513.

34. Ghetta V, Fouletier J, Chatain D. Acta Materialia 1996;44:1927.

35. Serre C, Wynblatt P, Chatain D. Surface Science 1998;415:336.

36. Shim H, Chatain D, Wynblatt P. Surface Science 1998;415:346.

37. T. Young, Philosophical Transactions of the Royal Society, **65**: 95, (1805).

38. L.E. Murr, Materials Science and Engineering, **12**[5-6]: 277-83, (1973).

39. T. Young, Philosophical Transactions of the Royal Society, **65**: 95, (1805).

40. E. Saiz, A.P. Tomsia and R.M. Cannon, Acta Materialia, **46**[7]: 2349-2361, (1998).

41. G. Levi and W.D. Kaplan, Acta Materialia, **51**[10]: 2793-2802, 2003.

42. J. Gaydos, A. W. Neumann, in Applied Surface Thermodynamics, Surfactant Science Series V.63, ed. by A. W. Neumann and J. K. Spelt, New York : Marcel Dekker (1996) p.169

43. D. Chatain and W.C. Carter, Nature Materials, **3**[12]: 843-845, (2004).

44. G. Levi, C. Scheu and W.D. Kaplan, Interface Science, **9**[3-4]: 213-220, (2001).

45. Y.X. Liu and R.M. German, Acta Materialia, **44**[4]: 1657-1663, (1996).

46. N. Eustathopoulos, M. G. Nicholas and B. Drevet, in, Pergamon Materials Series V.3, Oxford, UK, (1999) p.106-144.

47. G. Levi, D.R. Clarke and W.D. Kaplan, Interface Science, **12**[1]: 73-83, (2004).

48. D.J. Srolovitz, Goldinger, JOM, (1995).

49. Oh SH, Scheu C, Wagner T, Tchernychova E, Rühle M. Acta Materialia 2006;54:2685.

50. Scheu C, Klein S, Tomsia AP, Rühle M. Journal of Microscopy-Oxford 2002;208:11.

51. Scheu C. Interface Science 2004;12:127.

52. W. Mader and M. Rühle, Acta Metallurgica, 37[3]: 853-66, (1989).

53. J. Mayer, C.P. Flynn and M. Rühle, Ultramicroscopy, 33[1]: 51-61, (1990).

54. J.M. Howe, International Materials Reviews, **38**[5]: 233-256, (1993).

55. C. Herring, ed. By W.E. Kingston, McGraw-Hill, New York, (1951) p.143-179.

56. D.M. Saylor and G.S. Rohrer, Interface Science, **9**[1-2]: 35-42, (2001).

57. B.L. Adams, S. Ta'Asan, D. Kinderlehrer, I. Livshits, D.E. Mason, C.T. Wu, W.W. Mullins, G.S. Rohrer, A.D. Rollett and D.M. Saylor, Interface Science, **7**[3/4]: 321-338, (1999).

58. L.E. Murr, R.J. Horylev and W.N. Lin, Philosophical Magazine, **20**[168]: 1245-64, (1969).

59 W.L. Winterbottom, Acta Metallurgica, **15**: 303-310, 1967.

60. R.M. Pilliar and J. Nutting, Philosophical Magazine, **16**[139]: 181-8, (1967).

61. J.W. Cahn and D.W. Hoffman, Acta Metallurgica, **22**[10]: 1205-14, (1974).

62. Sadan H, Kaplan WD. Journal of Materials Science 2006;41:5099.

63. Ernst F. Metal-oxide interfaces. Materials Science and Engineering: R: Reports 1995;14:97.

64. Dehm G, Scheu C, Rühle M, Raj R. Acta Materialia 1998;46:759.

65. Mercer C, Faulhaber S, Yao N, McIlwrath K, Fabrichnaya O. Surface and Coatings Technology 2006;201:1495.

66. A.E. Murut and C.L. White, Acta Materialia, 45[6]: 2547-2563, (1997).

67. Zhang W, Smith JR, Evans AG. Acta Materialia 2002;50:3803.

68. Brillo J, Egry I. Journal of Materials Science 2005;40:2213

69. Hila Meltzman, Dominique Chatain, Dan Avizemer, Theodore M. Besmann, and Wayne D. Kaplan; accepted to Acta Materialia (February 2011).

70. Wang X-G, Smith JR, Evans AG. Physical Review B 2006;74:081403.

71. Shi S, Tanaka S, Kohyama M. Journal of the American Ceramic Society 2007;90:2429.

72. Zhang W, Smith JR, Wang X-G, Evans AG. Physical Review B 2003;67:245414.

73. Long Y, Chen NX. Journal of Physics Condensed Matter 2008;20.

74. Feng JW, Zhang WQ, Jiang W, Gu H. Physical Review Letters 2006;97.

75. Jiang Y, Smith JR, Evans AG. Applied Physics Letters 2008;92.

76. Gaudette F, Suresh S, Evans AG, Dehm G, Rühle M. Acta Materialia 1997;45:3503.

77. W. Zhang, J.R. Smith and A.G. Evans, Acta Materialia, **50**[15]: 3803-3816, (2002).

78. X.-G. Wang, J.R. Smith and A.G. Evans, Physical Review B (Condensed Matter and Materials Physics), **74**[8]: 081403-4, (2006).

79. K.P. Trumble and M. Rühle, Acta Metallurgica et Materialia, **39**[8]: 1915-1924, 1991.

80. R. Brydson, H. Mullejans, J. Bruley, P.A. Trusty, X. Sun, J.A. Yeomans and M. Ruhle, Journal of Microscopy, **177**[3]: 369-86, (1995).

81. V. Merlin and N. Eustathopoulos, Journal of Materials Science, **30**[14]: 3619-3624, (1995).

82. E. Saiz, A.P. Tomsia and K. Suganuma, Journal of the European Ceramic Society, **23**[15]: 2787-2796, 2003.

83. G. Levi, D.R. Clarke and W.D. Kaplan, **12**[1]: 73-83, 2004.

84. J.M. Howe, International Materials Reviews, **38**[5]: 233-256, 1993.

85. C. Wan, P. Kritsalis, B. Drevet and N. Eustathopoulos, Materials Science and Engineering a, **207**[2]: 181-187, 1996.

86. V. Merlin and N. Eustathopoulos, Journal of Materials Science, **30**[14]: 3619-3624, 1995.

87. P. Kritsalis, V. Merlin, L. Coudurier and N. Eustathopoulos, Acta Metallurgica Et Materialia, **40**[6]: 1167-1175, 1992.

88 G. Levi, C. Scheu and W.D. Kaplan, Interface Science, **9**[3-4]: 213-220, 2001.

89. P. Nikolopoulos, S. Agathopoulos, Journal of European Ceramic Society, **10**:415, (1992).

90. G. Levi, C. Scheu and W.D. Kaplan, Interface Science, **9**[3-4]: 213-220, (2001).

91. Gleeson B. Journal of Propulsion and Power 2006;22:375.

92. Meier GH, Pettit FS, Smialek JL. Materials and Corrosion 1995;46:232.

93. Hou PY, Izumi T, Gleeson B. Oxidation of Metals 2009;72:109.

94. Hou PY. Oxidation of Metals 1999;52:337.

95. E A. Golightly, E H. Stott, G. C. Wood: Oxid Met. 10 (1976), 163

96. Pint BA, More KL, Wright IG. Oxidation of Metals 2003;59:257.

97. B. A. Pint, Oxid. Met. 49, 531 (1998).

98. Guo H, Sun L, Li H, Gong S. Thin Solid Films 2008;516:5732.

99. J. E. McDonald, J.G. Eberhardt: Trans. TMS-AIME 233 (1965) 512.

100. Jiang Y, Smith JR.. Journal of Materials Science 2009;44:1734.

101. Bennett IJ, Kranenburg JM, Sloof WG. Journal of the American Ceramic Society 2005; 88:2209.

102. Brillo J, Egry I. Journal of Materials Science 2005;40:2213

103. Hong JS, Jo W, Ko KJ, Hwang NM, Kim DY. Philosophical Magazine: 2009;89:2989.

104. Mykura H. Acta Metallurgica; 1961;9:570

105. Hanbicki AT, Darling SB, Gaspar DJ, Sibener SJ. The Journal of Chemical Physics 1999;111:9053.

106. Barsotti T. Bermond JM. Drechsler M. Journal de Physique, Colloque 1984;C9:43.

107. Trumble KP, Ruhle M. Acta Metallurgica Et Materialia 1991;39:1915.

108. Reyntjens S. and Puers R., Journal of Micromechanics and Microengineering 2001;11:287.

109. Sadan H, Kaplan WD, Journal of Materials Science 2006;41:5099.

110. M. Haider, H. Rose, S. Uhlemann, E. Schwan, B. Kabius and K. Urban Ultramicroscopy, 75[1]: 53-60, 1998

111 K. Tillmann, L. Houben, A. Thust and K. Urban, Journal of Materials Science, V41[14]: 4420-4433, 2006.

112. L. Houben, A. Thust and K. Urban, Ultramicroscopy, **106**[3]: 200-214, (2006).

113. K. Tillmann, A. Thust and K. Urban, Microscopy and Microanalysis, **10**[2]: 185-198, (2004).

114. Stadelmann PA. Ultramicroscopy 1987;21:131.

115. Roosen AR, McCormack RP, Carter WC. Computational Materials Science 1998;11:16.

116. Lee, C.-W., Ikematsu, Y. & Shindo, D. (2002). Journal of Electron Microscopy 51(3),143.

117. Jin, Q., & Wang, S. (2006) Microscopy and Microanalysis, 12, 1184-1185.

118. Plitzko, J. M., & Mayer, J. (1999). Ultramicroscopy, 78, 207-219.

119. Joy, D.C., Egerton, R.F., Maher, D.M (1979). PP 817-826. SEM Inc. AMF O'Hare, IL

120. Egerton, R. F. & Cheng, S. C. (1987). Ultramicroscopy, 21, 231-244.

121. Malis, T., Cheng, S. C. & Egerton, R. F. Journal of electron microscopy technique (1988), 8, 193-200.

122. Thompson, K., Lawrence, D., Larson, D. J., Olson, J. D., Kelly, T. F. & Gorman, B. (2007).

123 M. Baram and W.D. Kaplan, Journal of Microscopy, 232[3]:395-405, 2008

124. Meltzman H, Kauffmann Y, Thangadurai P, Drozdov M, Baram M, Brandon D, Kaplan WD. Journal of Microscopy 2009;236:165.

125. Nash P, Nash A. Bulletin of Alloy Phase diagrams 1983;4:250.

126. Keene BJ. International Materials Reviews 1993;38:157.

127. Meltzman H. and Wayne D. Kaplan, to be published (2011)

128. Wang ZM, Wynblatt P. Surface Science 1998;398:259.

129. Chatain D, Ghetta V, Wynblatt P. Interface Science 2004;12:7.

130. Kaukasoina P, Lindroos M, Diehl RD, Fisher D, Chandavarkar S, Collins IR. Journal of Physics: Condensed Matter 1993;5:2875.

131. Thurgate SM, Jennings PJ. Applications of Surface Science 1985;22-23:478.

132. Venkataramani K, et al. Nanotechnology 2010;21:265602.

133. Renaud G, Barbier A, Robach O. Physical Review B 1999;60:5872.

134. Noguera C, Godet J, Goniakowski J. Physical Review B 2010;81:155409.

135. Olander J, Lazzari R, Jupille J, Mangili B, Goniakowski J, Renaud G. Physical Review B 2007;76:075409.

136. M Gautier, G Fenaud, L Pham Van, B Villette, M Pollak, N Thromat, F Jollet, J-P Duraud (1994) Journal of the American Ceramic Society 77, 323.

137. J Wang, A Howard, RG Egdell, JB Pethica, JS Foord. (2002) Surface Science 515, 337.

138. G Renaud, B Villette, I Vilfan, A Bourret. (1994). Phys. Rev. Lett. 73.

139. JV Lauritsen, MCR Jensen, K Venkataramani, B Hinnemann, S Helveg, BS Clausen, F Besenbacher. (2009) Physical Review Letters 103,076103.

140. EAA Jarvis, EA Carter. (2001) Journal of Physical Chemistry B 105, 4045.

141. S Gota, M Gautier-Soyer, L Douillard, JP Duraud, P Le Fevre (1996) Surface Science 352-354,1016.

142. G Dehm, C Scheu, G Möbus, R Brydson, M Rühle. (1997) Ultramicroscopy 67,207.

143. C Mercer, S Faulhaber, N Yao, K McIlwrath, O Fabrichnaya (2006) Surface and Coatings Technology 201,1495.

144. JA Haynes, BA Pint, KL More, Y Zhang, IG Wright. (2002) Oxidation of Metals, 58,513.

145. J. A. Haynes, K. L. More, B. A. Pint, I. G. Wright, K. Cooley, and Y. Zhang, (2001) Mater. Sci.Forum 369–372, 679.

146. VK Kumikov, KB Khokonov. (1983) Journal of Applied Physics 54,1346.